# Subcritical Turbulence in the Mega Ampere Spherical Tokamak




Ferdinand van Wyk

Mansfield College

University of Oxford

A thesis submitted for the degree of

*Doctor of Philosophy*

Michaelmas 2016

# Abstract

The transport of heat out of tokamak plasmas by turbulence is the dominant mechanism limiting the performance of fusion reactors. Turbulence can be driven by the ion temperature gradient (ITG) and suppressed by toroidal equilibrium scale sheared flows. Numerical simulations attempting to understand, and ultimately reduce, turbulence are crucial for guiding the design and optimisation of future reactors.

In this thesis, we investigate ion-scale turbulence by means of local gyrokinetic simulations in the outer core of the Mega Ampere Spherical Tokamak (MAST). We perform a parameter scan in the values of the ITG and the flow shear. We show that nonlinear simulations reproduce the experimental ion heat flux and that the experimentally measured values of the ITG and the flow shear lie close to the turbulence threshold. We demonstrate that the system is subcritical in the presence of flow shear, i.e., the system is formally stable to small perturbations, but transitions to a turbulent state given a large enough initial perturbation. We propose a scenario for the transition to subcritical turbulence previously unreported in tokamak plasmas: close to the threshold, the plasma is dominated by a low number of coherent long-lived structures; as the system is taken away from the threshold into the more unstable regime, the number of these structures increases until they fill the domain and a more conventional turbulence emerges.

We make quantitative comparisons of correlation properties between our simulations and experimental measurements of ion-scale density fluctuations from the MAST BES diagnostic. We apply a synthetic diagnostic to our simulation data and find reasonable agreement of the correlation properties of the simulated and experimental turbulence, most notably of the correlation time, for which significant discrepancies were found in previous numerical studies of MAST turbulence. We show that the properties of turbulence are essentially functions of the distance to threshold, as quantified by the ion heat flux. We find that turbulence close to the threshold is strongly affected by flow shear, whereas far from threshold, the turbulence resembles a conventional ITG-driven, zonal-flow damped regime.

# Acknowledgements

I would like to thank my supervisors Prof. Alex Schekochihin, Dr. Edmund Highcock, and Dr. Colin Roach for their support and guidance throughout my DPhil, and for instilling in me the importance of taking care of the details. As result of their guidance, I have become better scientist, writer, and programmer.

I benefitted over the years from the advice and expertise of senior members of the extended Oxford and Culham plasma physics groups: Ian Abel, Anthony Field, Felix Parra, Bill Dorland, Paul Dellar, Michael Barnes, and Nuno Loureiro who were always willing to help. I also greatly appreciated the company of my fellow plasma physics graduate students who made it a much easier journey: Michael Fox, Justin Ball, Greg Colyer, Alessandro Geraldini, Joseph Parker, and last but not least, George Wilkie, whose humour made every conference a more enjoyable experience.

There are many other fellow graduate students from Mansfield College and elsewhere, who made the DPhil journey with me either in person, or in spirit, and whose support was greatly appreciated: Alex Rowell, Nicole Miranda, Chris Birkl, James Fagan, Katia Damer, and Kevin O'Keeffe. Particular thanks goes to Cherese Thakur, Daniel Lordan, and Phelim Bradley who went through all the ups and downs of graduate life with me.

From my time at University College Cork, I would like to thank Dr. Paddy McCarthy for helping me reach my goal of researching fusion energy and Prof. Frank Peters for his engaging lectures and encouragement.

Finally, this DPhil would not have been possible without the support of my family. My mom and her partner who have allowed me to follow my interests and to reach my potential, but above all my brother Adriaan whose limitless good humour and high spirits have always been a source of optimism.

# *Contents*


**1 Introduction** **1**
- 1.1 Nuclear fusion . . . 1
- 1.2 Turbulence . . . 2
- 1.3 Sheared flows and subcritical turbulence . . . 3
- 1.4 Comparisons between simulations and experimental measurements . . . 4
- 1.5 Thesis outline . . . 7

**2 MAST experimental configuration** **9**
- 2.1 The Mega Ampere Spherical Tokamak . . . 9
- 2.2 Equilibrium profiles . . . 10
  - 2.2.1 MAST discharge #27274 . . . 10
  - 2.2.2 A note on radial grids . . . 11
  - 2.2.3 MAST profile diagnostics . . . 12
  - 2.2.4 Equilibrium profiles . . . 13
  - 2.2.5 Sign of $\omega$ and $\gamma_E$ . . . 16
- 2.3 Beam emission spectroscopy . . . 17

**3 Modelling plasma turbulence** **19**
- 3.1 Introduction . . . 19
- 3.2 Toroidal geometry . . . 20
- 3.3 Local gyrokinetic description . . . 22
  - 3.3.1 The Fokker-Planck equation . . . 22
  - 3.3.2 The gyrokinetic orderings and assumptions . . . 22
  - 3.3.3 The gyrokinetic equation . . . 24
  - 3.3.4 Flow shear stabilisation . . . 26
- 3.4 Overview of GS2 . . . 27
  - 3.4.1 Geometry . . . 28
  - 3.4.2 Collisions . . . 34

3.4.3 Real-space effect of flow shear . . . 36
3.4.4 Implementation of hyperviscosity . . . 38
3.5 Numerical set-up . . . 40

**4 Nonlinear simulations 45**
4.1 Introduction . . . 45
4.2 Heat flux . . . 47
4.3 Subcritical turbulence . . . 50
4.3.1 Minimum initial perturbation amplitude . . . 51
4.3.2 Finite lifetime of turbulence . . . 52
4.3.3 Transient growth of perturbations . . . 54
4.3.4 Characterising transient growth . . . 54
4.3.5 Conditions for the onset of subcritical turbulence . . . 57
4.4 Structure of turbulence close to and far from the threshold . . . 59
4.4.1 Coherent structures in the near-marginal state . . . 60
4.4.2 $Q_i/Q_{\mathrm{gB}}$ as an order parameter . . . 64
4.4.3 Maximum amplitude . . . 65
4.4.4 Structure counting . . . 67
4.4.5 Shear due to zonal flows . . . 71
4.5 Summary . . . 73

**5 Correlation analysis and comparison with experimental results 75**
5.1 Introduction . . . 75
5.2 Correlation analysis . . . 77
5.2.1 Radial correlation length . . . 78
5.2.2 Poloidal correlation length . . . 79
5.2.3 Correlation time . . . 81
5.2.4 Parallel correlation length . . . 82
5.2.5 Density-fluctuation amplitude . . . 83
5.3 Experimental BES results . . . 83
5.4 Correlation analysis with synthetic diagnostic . . . 85
5.5 Correlation analysis of raw GS2 data . . . 88
5.5.1 Correlation parameters within experimental uncertainty . . . 89
5.5.2 Correlation parameters versus $Q_i/Q_{\mathrm{gB}}$ . . . 96
5.6 Summary . . . 100

**6 Conclusions 102**
6.1 Future directions . . . 105

**A Linear and nonlinear effect of hyperviscosity** **107**

**B Resolving the effect of flow shear** **111**

**C Linear simulations with $\gamma_E = 0$** **113**

**D Transforming to real space and laboratory frame** **116**
D.1 Laboratory frame . . . . . 116
D.2 Radial domain size . . . . . 117
D.3 Poloidal domain size . . . . . 118
D.4 Parallel coordinate and domain size . . . . . 119

**E Synthetic correlation properties without the "spike filter"** **121**

**F Example GS2 input file** **123**

**Bibliography** **127**

# *List of Figures*


1.1 Toroidal configuration of magnetic field lines . . . . . 2

2.1 Image of MAST plasma . . . . . 10
2.2 MAST flux surfaces . . . . . 12
2.3 Experimental profiles . . . . . 15
2.4 Experimental heat flux profile . . . . . 16
2.5 MAST point-spread functions . . . . . 18

3.1 Toroidal geometry . . . . . 21
3.2 MAST magnetic field lines . . . . . 31
3.3 Physical effect of $\gamma_E$ . . . . . 37
3.4 $(\kappa_T, \gamma_E)$ values in parameter scan . . . . . 41

4.1 Contour plot of $Q_i/Q_{\mathrm{gB}}$ versus $\kappa_T$ and $\gamma_E$ . . . . . 48
4.2 Values of $Q_i/Q_{\mathrm{gB}}$ versus $\kappa_T$ and $\gamma_E$ . . . . . 49
4.3 $Q_i/Q_{\mathrm{gB}}$ line plots versus $\kappa_T$ and $\gamma_E$ . . . . . 49
4.4 $Q_i/Q_{\mathrm{gB}}$ line plots within experimental uncertainty . . . . . 50
4.5 Demonstration of subcritical turbulence . . . . . 52
4.6 Transient growth of electrostatic potential . . . . . 55
4.7 $N_\gamma$ and $t_0$ versus $k_y\rho_i$ . . . . . 57
4.8 $N_\gamma$ and $t_0$ versus $k_y\rho_i$ for marginally unstable simulations . . . . . 58
4.9 Maximum transient-amplification factor . . . . . 59

4.10 Real-space density-fluctuation fields on $(x, y)$ plane . . . . . 60
4.11 Real-space radial $\boldsymbol{E} \times \boldsymbol{B}$ velocity on $(x, y)$ plane . . . . . 62
4.12 Real-space perpendicular temperature-fluctuation fields $T_{\perp i}$ on $(x, y)$ plane . 63
4.13 Real-space density-fluctuation fields in parallel direction . . . . . 64
4.14 Radial and poloidal advection of coherent structure . . . . . 65
4.15 Scaling of maximum fluctuation amplitude with $Q_i/Q_{\mathrm{gB}}$ . . . . . 66
4.16 Structure counting procedure . . . . . 68
4.17 Scaling of number of structures with $Q_i/Q_{\mathrm{gB}}$ . . . . . 69
4.18 $N(\delta n_i/n_i)^2_{\mathrm{max}}$ scaling with $Q_i/Q_{\mathrm{gB}}$ . . . . . 70
4.19 Ratio of zonal shear to background flow shear . . . . . 72
4.20 Zonal shear versus background flow shear . . . . . 73

5.1 Radial correlation function . . . . . 79
5.2 Poloidal correlation function . . . . . 80
5.3 Time correlation function . . . . . 82
5.4 Parallel correlation function . . . . . 83
5.5 Experimental correlation results . . . . . 84
5.6 Correlation parameters of synthetic GS2 data . . . . . 86
5.7 Correlation parameters for raw GS2 density fluctuations . . . . . 90
5.8 Correlation parameters for raw GS2 density fluctuations (cont'd) . . . . . 93
5.9 Comparison of linear and nonlinear time scales . . . . . 95
5.10 Correlation parameters for GS2 density fluctuations versus $Q_i/Q_{\mathrm{gB}}$ . . . . . 97
5.11 Correlation parameters for GS2 density fluctuations versus $Q_i/Q_{\mathrm{gB}}$ (cont'd) . 98

A.1 Linear effect of hyperviscosity . . . . . 108
A.2 Effect of hyperviscosity on $N_\gamma$ and $Q_i/Q_{\mathrm{gB}}$ . . . . . 109

B.1 Nonlinear decorrelation time versus ITG . . . . . 112

C.1 Linear growth rates and frequencies for one species, adiabatic electron simulations . . . . . 114

C.2 Linear growth rates and frequencies for two-species simulations . . . . . 114
C.3 Maximum growth rate . . . . . 115

D.1 MAST magnetic-field pitch-angle . . . . . 118
D.2 GS2 density fluctuations for a near-marginal case on an $(R, Z)$-plane . . . . 119

E.1 GS2 correlation parameters with a synthetic diagnostic applied without a numerical "spike filter" . . . . . 122

# Chapter 1

# *Introduction*

## 1.1 Nuclear fusion

Nuclear fusion is the process that powers the stars. Confined by the gravitational force and heated to very high temperatures, hydrogen isotopes can collide and fuse to form helium and release large amounts of energy. When it comes to harnessing this power for use on Earth, the most promising fusion reaction is between deuterium and tritium isotopes of hydrogen, which produces a 3.5 MeV helium nucleus and a 14.6 MeV neutron. Utilising this reaction for the purposes of electricity generation has been the goal of fusion scientists since the idea was first proposed in the 1950s.

The tokamak has emerged as the most promising concept for confining this reaction by using a toroidal configuration of magnetic field lines (see Figure 1.1). At the temperatures required for fusion to occur, deuterium and tritium become fully ionised and the gas becomes a plasma. In the presence of a magnetic field, these charged particles are forced to gyrate about the magnetic field lines in a plane perpendicular to the field lines and although they can freely stream along them, they remain confined. This is because in the toroidal configuration, magnetic field lines lie on a single surface and so provide no direct route out of the plasma. This is crucial given that no material one could feasibly build a fusion reactor out of, can withstand direct contact with the extremely high temperature fusion plasma. This also necessarily means that large pressure gradients are set up between the hot core, where fusion reactions take place, and the relatively cool

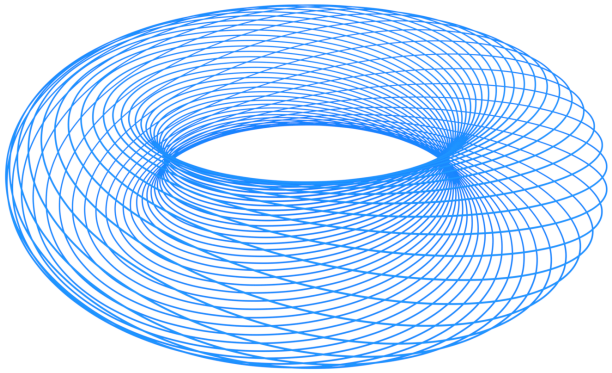


Figure 1.1: Toroidal configuration of magnetic field lines used to confine fusion plasmas.

edge near the reactor walls. It is these gradients that give rise to a physical process that has hindered the realisation of fusion energy since the first attempts to build reactors large enough to produce electricity: turbulence.

## 1.2 Turbulence

Even in the ideal confinement scenario described above, there are still processes by which plasma particles can escape. These processes include collisions with other particles in addition to particle drifts due the presence of an electric field, magnetic field line curvature, and magnetic field gradients. The transport of particles, momentum, and heat out of the plasma due to these processes is known as neoclassical transport [1–5]. While important, neoclassical transport alone would not significantly hinder the viability of a well-designed fusion reactor. Instead, it is turbulence that presents a much greater challenge to fusion power as an energy source [6–13]. In the presence of gradients of density, flow, or temperature, small perturbations to the plasma state can grow exponentially, and eventually interact with each other, leading to a turbulent state. This turbulent state gives rise to enhanced radial transport of particles, momentum, and heat, which can significantly exceed neoclassical estimates [14–17]. This presents a challenge for sustaining the temperatures and densities necessary in the core for fusion. Thus, reducing or eliminating turbulence completely would be the most effective means of achieving improved fusion power.

Experimental, numerical, and theoretical studies have shown that turbulent transport is strongly dependent on the ion temperature gradient (ITG) [17–27]. Additionally, the electron temperature and density gradients, which give rise to the electron temperature gradient (ETG) mode [10, 11] and the trapped electron mode (TEM) [12], can also drive turbulence. In this work, we will focus on turbulence driven by the ITG, which is a source of free energy and drives the well-known ITG instability [6, 8], in combination with turbulence driven by the TEM, which also drives turbulence at ion scales. It is well-established that modest increases in the ITG lead to large increases in ion heat flux, so-called "stiff transport" (see [17] for a recent experimental study). The phenomenon of stiff transport is an important consideration in the design of fusion reactors. In order to maximise the temperature in the core (to increase fusion power) we want to maximise the temperature gradient between the core and the relatively cool edge, where technological constraints (e.g. material strain due to heat deposition, melting due to high temperatures, etc.) must be taken into account. However, enhanced ITG-driven transport (which reduces the ITG) would set an upper bound on the ITG and, hence, on the core temperature that we can achieve. That is, unless some process exists that can reduce or eliminate turbulence, driven by the ITG instability, without reducing the ITG itself. Fortunately, it has been shown that such a process exists in the form of sheared flows perpendicular to the magnetic field lines.

## 1.3 Sheared flows and subcritical turbulence

It has been shown experimentally that toroidal rotation, or more specifically the differential rotation between surfaces of constant magnetic field, can lead to a reduction or even complete suppression of turbulence [17, 20, 28–30]. Toroidal differential rotation can be driven by the neutral beam injection (NBI) system present in most fusion experiments [30]. The NBI system injects deuterium atoms at high energy to heat the plasma and simultaneously generates a toroidal flow in the plasma. This gives rise to a sheared flow (since the NBI system deposits most of its momentum and heat at the core of the plasma) with components both parallel and perpendicular to the direction of the magnetic field. Perpendicular flow shear has been shown to reduce, or even eliminate,

turbulence, while parallel flow shear has been shown to drive a linear instability [7] (the parallel-velocity gradient (PVG) instability), which can increase the level of turbulence. This effect has been confirmed in many numerical studies [26, 27, 31–35]. However, it was shown that large flow shears and temperature gradients are required before the destabilising effect of the parallel flow shear is strong enough to overcome the stabilising effect of the perpendicular flow shear [26, 27]. For this reason, PVG-driven turbulence is not expected to play a large role in the experimentally relevant plasmas we will consider in this work, given the modest levels of the ITG and flow shear. To summarise, we see that there is a competition in fusion plasmas between the destabilising effects of the ITG and PVG instabilities, and the stabilising effect of the perpendicular flow shear.

Perpendicular flow shear can reduce turbulence levels in two ways: by stabilising the linear instabilities that amplify small perturbations, and by shearing apart eddies that characterise the turbulent state. It has been shown that perpendicular flow shear can, in fact, render the plasma completely linearly stable. However, there may still be substantial transient growth of perturbations and, given large enough initial perturbations, this transient growth can still lead to a saturated nonlinear state – a phenomenon known as "subcritical" turbulence [26, 27, 36–39]. This is a well-known phenomenon in neutral fluid systems, such as Couette and Poiseuille flows, where, though they are linearly stable, finite perturbations can nonetheless lead to a turbulent state [40–45]. Understanding the transition to a turbulent state in subcritical systems is a long-standing challenge in neutral fluids and, more recently, in fusion plasmas, where dramatically improved confinement is possible in the absence of turbulence. However, there is currently very little known about the transition to subcritical turbulence in fusion-relevant plasmas – an issue we address in this thesis.

## 1.4 Comparisons between simulations and experimental measurements

At the temperatures and densities found in fusion experiments, such as MAST, it can be shown that the conditions for a fluid description are rarely satisfied and that a kinetic

description must be used (see [46] for a recent discussion). Gyrokinetics [47–49] has emerged as the most appropriate first-principles description in the context of plasma turbulence in the core of tokamaks – the focus of this thesis. The nonlinear gyrokinetic equation is derived via an asymptotic expansion of the Fokker-Planck equation. In general, it can only be solved numerically, and a number of codes have been developed for this purpose, for example, GS2 [11, 50] (the code used in this work), GENE [10, 51], and GYRO [52]. There has been a concerted effort to include in these codes a large number of physical effects relevant to experimental plasmas, such as realistic magnetic-surface geometries, arbitrary numbers of kinetic species, realistic Fokker-Planck collision operators, and so on. This has allowed the simulation of turbulence in fusion plasmas with sufficient realism to be compared quantitatively to experimental measurements. These "local" codes, such as GS2, take as input the values and first derivatives of equilibrium quantities at a particular radial location, and predict a host of quantities that could theoretically be measured by an experimental diagnostic, for example, the flux of particles, momentum, and heat, or density, flow, and temperature fluctuations.

In conjunction with increasingly realistic modelling, more sophisticated diagnostic techniques have been designed, which aid in our understanding of the conditions inside the reactor and allow us to make comparisons with modelling results. Initial comparisons between simulations and experiments were limited to averaged quantities such as the transport of particles, momentum, and heat. More recently, diagnostics that measure fluctuating quantities have been developed: beam emission spectroscopy (BES) that measures ion-scale density fluctuations [53–56]; Doppler reflectometry that measures density fluctuation at scales intermediate to ion and electron scales, rotation velocity of turbulent structures, and the radial electron field [57–59]; scattering diagnostics that measure electron scale density fluctuations [60]; and correlation electron cyclotron emission (CECE) diagnostics [61] that measure electron temperature fluctuations. Measurements of fluctuating quantities allow more extensive quantitative comparisons between experiment and simulations. However, meaningful comparisons are only possible via the use of "synthetic diagnostics" that take account of the measurement characteristics of the particular diagnostic and modify the simulation output accordingly [61–66].

In this work, we will focus on measurements from the BES system on MAST [54,

55]. The BES diagnostic infers ion-scale turbulent density fluctuations from $D_\alpha$ emission (the emission of light resulting from the dominant transition of ionised deuterium), which is generated as a result of the injection of neutral particles by the NBI system. The BES diagnostic takes measurements in a two-dimensional radial-poloidal plane. In the case of an ITG- or TEM-unstable plasma, the characteristic turbulence length scale in the direction perpendicular to the magnetic field is of the order of the ion gyroradius [67]: $l_\perp \sim \rho_i$, and it is these turbulent structures that BES is designed to measure. Such two-dimensional measurements provide insight into the structure of turbulence, and they have allowed turbulence to be visualised for the first time. From the BES measurements, it is possible to estimate the turbulence correlation time $\tau_c$ via the cross-correlation time delay (CCTD) method [64, 66, 68], the radial and poloidal correlation lengths $l_R$ and $l_Z$, and the relative density-fluctuation field $\delta n_i/n_i$ [66, 69]. A recent experimental study [65] used the BES diagnostic to measure turbulent density fluctuations in the outer core of a MAST L-mode plasma and compared with global gyrokinetic simulations. While there was some agreement at mid-radius, serious discrepancies remained at outer radii, where ITG turbulence may not be fully suppressed by flow shear, in predictions of turbulence characteristics, such as the ion heat flux and turbulence correlation time. In this work, we will study turbulence in the outer-core region of the MAST discharge in Ref. [65] using high-resolution local gyrokinetic simulations.

In simulating experimentally-relevant plasmas using gyrokinetic codes, we aim to achieve the following. First, we want to better understand the physical mechanisms that most affect influence turbulence and its associated enhanced transport. Specifically, how do turbulence characteristics (such as transport, spatial scales, time scales, etc.) change in the outer core of MAST with the ITG and the flow shear? Secondly, in light of newly available experimental data from the MAST BES diagnostic [65], do the turbulence characteristics found in local gyrokinetic GS2 simulations agree with experimental BES measurements within the experimental uncertainties of the ITG and flow shear? Such quantitative comparisons with experimental results are essential in developing confidence in our theoretical models and numerical implementations. In understanding the properties of turbulence, we ultimately aim to guide the optimisation and design of future experiments and fusion reactors to mitigate or eliminate the causes

of turbulence.

## 1.5 Thesis outline

The rest of this thesis is organised as follows. In Chapter 2, we give an overview of MAST, the MAST BES diagnostic, and discuss the discharge we will be considering in this work. In Chapter 3, we give an overview of gyrokinetics and the GS2 code that we use to solve the system of gyrokinetic equations in an axisymmetric torus. We discuss the toroidal geometry that is appropriate to tokamaks and the relevant approximations in this setting that are used to derive the gyrokinetic equation. We discuss details of the numerical implementation of GS2 pertinent to our study, such as the extraction of geometric information from experimental output, the calculation of collision frequencies, and the implementation of flow shear and hyperviscosity. Finally, we detail the numerical setup for our study, including the extent of our parameter scan, the physics we have included, the approximations we have made, the numerical resolutions we have used (along with a justification for choosing them), and lastly a comprehensive table of parameters extracted from the experiment required to run a numerical study.

The main results of this work are split into two parts. In Chapter 4, we will study, numerically, the effect on turbulence in the outer core of MAST, when the ITG and perpendicular flow shear are changed. We will show that turbulent transport is stiff with respect to changes in the ITG, but also that the perpendicular flow shear is effective at suppressing turbulence. Performing an extensive parameter scan in these two equilibrium parameters, we map out the turbulence threshold (the line separating regions of enhanced turbulent transport and neoclassical transport) and show that the experimental level of ion heat flux corresponds to values of the ITG and flow shear close to the turbulence threshold. We discover that the system is subcritical and that large initial perturbations are required to ignite turbulence, a phenomenon not previously observed for experimentally-relevant plasmas. Furthermore, we discover that the near-threshold state is one dominated by long-lived, coherent structures, which exist against a background of much smaller fluctuations. We argue that these structures are a direct consequence of the subcritical nature of the system, which concentrates plasma into these

structures as a means of maintaining the minimum amplitude below which fluctuations would be quenched. Sufficiently far from the turbulence threshold in parameter space, we recover a more conventional turbulent state consisting of many strongly interacting eddies simultaneously being sheared apart by the perpendicular flow shear. The number and amplitude of the above structures are shown to be functions of the distance from the turbulence threshold in the parameter space of ITG and flow shear – both increasing as the ITG is increased or as the flow shear is decreased. In this way, we identify three distinct regions of parameter space: the region of no turbulence (where transport would be neoclassical); a marginally unstable, intermediate state between the non-turbulent and fully turbulent states, characterised by long-lived, coherent structures; and a conventional chaotic, turbulent state far from the turbulence threshold.

In Chapter 5, we make direct comparisons with experimental measurements from the BES. We review the existing methods for performing a correlation analysis of BES measurements and discuss the differences in applying such an analysis to our simulations. Additional analyses are performed, such as calculating the parallel correlation length – something not currently experimentally measured. We then proceed to present two types of correlation analysis of our simulations: with and without a synthetic diagnostic. We show that there is reasonable agreement with experimental measurements in the case of analysis with the synthetic diagnostic. However, radial correlation lengths predicted by GS2 are shown to be below the resolution threshold of the BES diagnostic (an issue discussed in detail in Ref. [66]). Our analysis without the synthetic diagnostic shows that the synthetic diagnostic has a measurable effect on several turbulence characteristics, including the poloidal correlation length and the fluctuation amplitude, consistent with work in Ref. [66]. Finally, we present the correlation properties as functions of the ion heat flux and show that the structure of the turbulence in our simulations is effectively only a function of this parameter, which measures the distance to the turbulence threshold.

Our discussion and conclusions are presented in Chapter 6, along with suggestions for future work.

# Chapter 2

# *MAST experimental configuration*

## 2.1 The Mega Ampere Spherical Tokamak

MAST [70, 71] is a medium-sized, low-aspect ratio spherical tokamak. Along with the National Spherical Torus Experiment Upgrade (NSTX-U)[72, 73] in Princeton, USA, it is one of the leading spherical tokamaks: a novel reactor design that is under active research as an alternative to conventional high-aspect ratio reactors [74], such as the Joint European Torus (JET). Spherical tokamaks offer a number of potential advantages over conventional tokamaks that could make them suitable as fusion reactors [74, 75]: (i) lower cost due to compact design; (ii) higher plasma $\beta$ (ratio of plasma pressure to magnetic pressure), as a result of more efficient confinement; (iii) superconducting magnets are not strictly needed due to already high plasma $\beta$; (iv) in the case of MAST, high rotation and resulting sheared flows can suppress turbulence. The energy confinement of spherical tokamaks has been shown to be comparable to conventional tokamaks [76] and promisingly, spherical tokamaks show more favourable energy confinement scalings with experimental parameters [77, 78].

Figure 2.1 shows an image of a typical MAST plasma[1] and Table 2.1 gives some important parameters of the MAST device[71]. MAST is equipped with two NBI systems directed tangential to the flux surfaces that heat the plasma, with injected power up to $3.8$ MW. The NBI system also gives rise to toroidal rotation and differential toroidal

[1] `http://www.opendata.ccfe.ac.uk/mast/`

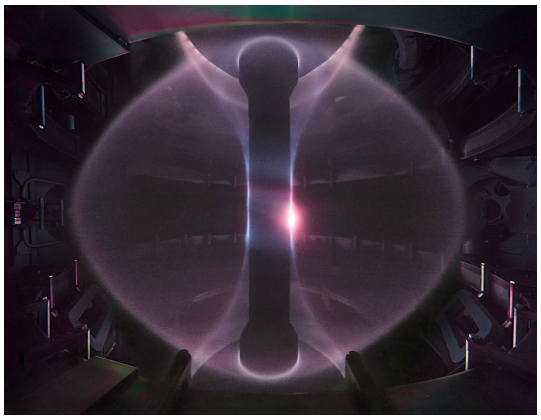


Figure 2.1: Image of the MAST tokamak in operation highlighting the compact D-shaped geometry aided by a narrow central magnet column. The bright spot is the location at which deuterium fuel is pumped into the plasma and is ionised.

| | |
|---|---|
| Major radius $R$ | $\approx 0.9$ m |
| Minor radius $a$ | $\approx 0.6$ m |
| Aspect ratio $A = R/a$ | $\approx 1.5$ |
| Plasma current $I_p$ | 1.3 MA |
| Magnetic field $B$ | 0.5 T |
| Pulse duration | 0.5 s |
| Power injected | 3.8 MW |

Table 2.1: Experimental parameters for the MAST experiment.

rotation, which will be the subject of our investigation. MAST is one of the more well-diagnosed tokamaks in operation, making it an ideal experiment to test theoretical predictions against. We detail the range of diagnostics that have allowed us to perform our numerical transport study in Section 2.2 and the review the BES system in Section 2.3 with which we compared our simulation results.

## 2.2 Equilibrium profiles

### 2.2.1 MAST discharge #27274

In this work, we will focus on the MAST discharge #27274, which forms part of a set of three nominally identical experiments (i.e., identical profiles and equilibria) previously reported in Ref. [65], differing only in the radial viewing location of the BES system. The three discharges are #27272, #27268, and #27274, wherein the centre of the BES was located at 1.05 m, 1.2 m, and 1.35 m, respectively. Each discharge produced an L-mode plasma with strong toroidal rotation and, hence, flow shear perpendicular and

parallel to the magnetic field [65]. The MAST BES diagnostic [54, 55] observes an area of approximately $16 \times 8$ cm$^2$ in the radial and poloidal directions, respectively, corresponding to approximately one third of the minor radius of the plasma. Therefore, the combination of the above discharges provided a complete radial profile of BES measurements on the outboard side of the plasma.

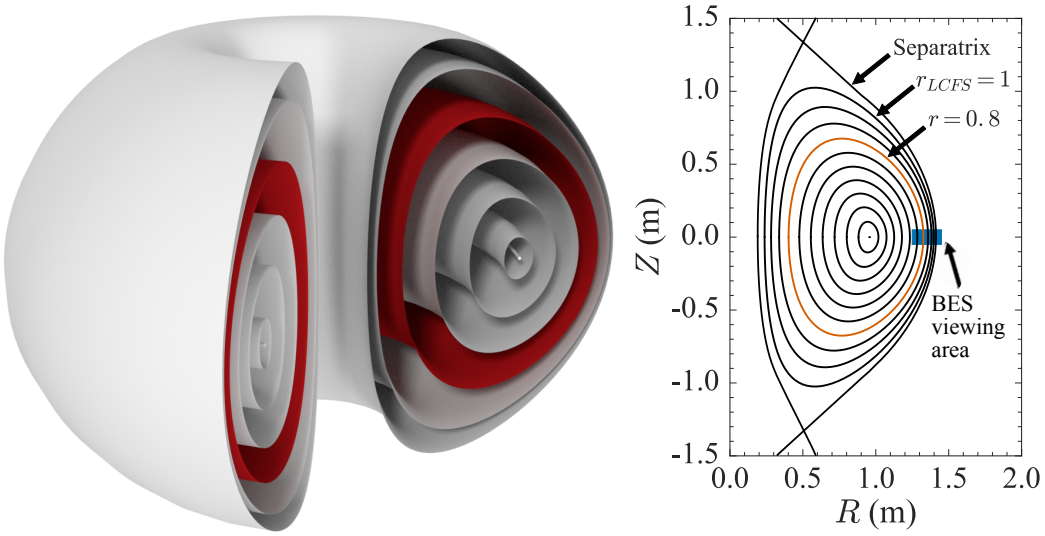
Previous investigations of MAST turbulence for similar configurations [30, 35], found that ion-scale turbulence is suppressed in the core region by flow shear. However, flow shear is weaker in the outer-core region, which may still be unstable to ITG modes, making it possibly to study ion-scale turbulence. Turbulence is also driven partly by trapped electron modes (TEMs) and the electron temperature gradient (ETG). In this work, we will restrict our attention to the time window $t = 0.250 \pm 0.002$ s and the radial location $r = D/2a = 0.8$ ($\equiv r_0$) of #27274, where $D$ is the diameter of the flux surface and $a$ is the half diameter of the last closed flux surface (LCFS), both measured at the height of the magnetic axis. Importantly, there is no large-scale and disruptive magnetohydrodynamic (MHD) activity at this time and radial location [65]; as such activity would interfere with the quality of BES measurements. The normalized radial location $r = 0.8$ corresponds to a major radius of approximately $1.32$ m and, therefore, falls within the viewing area covered by discharge #27274 [see Figure 2.2(b)].

### 2.2.2 A note on radial grids

We use $r = D/2a$ as the definition of the radial location because it corresponds to the radial coordinate used by the Miller specification of flux-surface geometry [79] (see Section 3.4.1). In terms of other commonly used radial coordinates, $r = 0.8$ corresponds to $\rho_{\rm tor} = \sqrt{\psi_{\rm tor}/\psi_{\rm tor,LCFS}} = 0.7$ where

$$\psi_{\rm tor} = \left(\frac{1}{2\pi}\right)^2 \int_0^V dV \boldsymbol{B} \cdot \nabla\phi \tag{2.1}$$

is the toroidal magnetic flux, $V$ is the volume enclosed by the flux surface, $\boldsymbol{B}$ is the magnetic field, $\phi$ is the toroidal angle, and $\psi_{\rm tor,LCFS}$ is the toroidal flux enclosed by the last closed flux surface [see Figure 2.2(b)]. In terms of the poloidal magnetic flux,




(a) (b)

Figure 2.2: (a) A three-dimensional view of the nested flux surfaces. (b) The poloidal cross-section of the magnetic geometry along with the LCFS and the separatrix, which separates closed field lines from open ones. The flux surface of interest is at $r = 0.8$, shown in red. It was chosen so that this surface intersects the BES measurement plane for discharge #27274. The blue shaded region indicates the location of the BES diagnostic.

$\rho_{\rm pol} = \sqrt{\psi_{\rm pol}/\psi_{\rm pol,LCFS}} = 0.87$, where

$$\psi \equiv \psi_{\rm pol} = \left(\frac{1}{2\pi}\right)^2 \int_0^V dV \boldsymbol{B} \cdot \nabla\theta \tag{2.2}$$

is the poloidal magnetic flux, $\theta$ is the poloidal angle, and $\psi_{\rm pol,LCFS}$ is the poloidal flux enclosed by the LCFS.

### 2.2.3 MAST profile diagnostics

MAST has a range of high-quality diagnostics, which allow us to extract the equilibrium parameters required to conduct a numerical transport study. The ion temperature, $T_i$, and toroidal flow velocity, $u_\phi = R\omega$, where $\omega$ is the toroidal angular rotation frequency, were obtained from charge-exchange-recombination spectroscopy (CXRS) measurements of $C^{+6}$ impurity ions with a spatial resolution of $\sim$ 1 cm [80]. The

electron density, $n_e$, and temperature, $T_e$, were obtained from a Thomson-scattering (TS) diagnostic [81] with resolution comparable to the CXRS system. These measured profiles were mapped onto flux-surface coordinates by the pre-processing code $MC^3$ using a motional-Stark-effect-(MSE)-constrained EFIT equilibrium [82]. These equilibrium profiles served as input to the transport analysis code TRANSP[2] [83], which calculates the transport coefficients of particles, momentum, and heat. Figure 2.2(a) shows a three-dimensional view of the axisymmetric nested flux surfaces and Figure 2.2(b) shows the poloidal cross-section of the flux surfaces extracted from an EFIT equilibrium. The $r = 0.8$ surface is highlighted in both plots. The measurement window of the BES diagnostic for discharge #27274 is also shown in Figure 2.2(b). The chosen flux surface at $r = 0.8$ intersects the measurement window at the outboard midplane, allowing direct comparisons between our numerical predictions of turbulence and experimental measurements.

### 2.2.4 Equilibrium profiles

The important experimental quantities needed to conduct a numerical study are the radial profiles of $T_i$, $T_e$, $n_i$ (the ion density), $n_e$, and $\omega$. MAST does not take direct measurements of $n_i$, but we assume that it is equal to $n_e$, as measured by the TS diagnostic, due to quasineutrality. As explained in Section 3.3, it is assumed in the local formulation of gyrokinetics that only the physical quantities (and their first derivatives) at the location of the flux tube determine the characteristics of the turbulence. Therefore, to conduct a numerical study of turbulence we need only the equilibrium values and their first derivatives (or for some quantities their gradient length scales) at $r = 0.8$ to simulate turbulence at that radius. The appropriate (normalised) gradient length scales of $T_i$,

[2] `http://w3.pppl.gov/transp/`

$T_e$, and $n_e$, and flow shear (gradient of $\omega$) are

$$\frac{1}{L_{Ti}} = -\frac{\mathrm{d}\ln T_i}{\mathrm{d}r} \equiv \kappa_T, \tag{2.3}$$

$$\frac{1}{L_{Te}} = -\frac{\mathrm{d}\ln T_e}{\mathrm{d}r}, \tag{2.4}$$

$$\frac{1}{L_{ne}} = -\frac{\mathrm{d}\ln n_e}{\mathrm{d}r}, \tag{2.5}$$

$$\gamma_E = \frac{r_0}{q_0}\frac{\mathrm{d}\omega}{\mathrm{d}r}\frac{a}{v_{\mathrm{th}i}}, \tag{2.6}$$

where $q(\psi) = \partial\psi_{\mathrm{tor}}/\partial\psi_{\mathrm{pol}}$ is the safety factor and $q_0$ is the value at $r_0$, $v_{\mathrm{th}i} = \sqrt{2T_i/m_i}$ is the ion thermal velocity, and $m_i$ is the mass of the ion species (deuterium). In a tokamak, the safety factor is approximately $q(\psi) \sim (r/R)(B_\phi/B_\theta)$, where $B$ is the magnetic field, $B_\theta = |\nabla\psi|/R$ is the poloidal component of $B$, and $R$ is the major radius at the location of the flux surface at the outboard midplane. The flow shear parameter $\gamma_E$ can be interpreted as the (non-dimensionalised) shear of the component of the toroidal shear perpendicular to the local magnetic field. The sign of $\gamma_E$ is determined in Section 2.2.5, given that $\omega$ can be positive or negative depending on the sign convention used.

The left-hand column of Figure 2.3 shows the radial profiles of $T_i$, $T_e$, $n_e$, and $\omega$ (with the sign determined as in Section 2.2.5), as functions of $r$. The gradient scale lengths (2.3)–(2.5) and flow shear (2.6) are plotted as functions of $r$ in the right-hand column in Figure 2.3. The dashed lines indicate $r = 0.8$ and the equilibrium values at this radial location are given in Table 2.2. The profiles in Figure 2.3 represent a 20-ms time average around $t = 0.25$ s and the shaded areas indicate the standard deviations.

The profile of the ion heat flux $Q_i^{\mathrm{exp}}$ was calculated by using the equilibrium profiles and magnetic geometry as input to a TRANSP analysis, which calculated $Q_i^{\mathrm{exp}}$ as a function of $r$ by equating it to the net deposited power within the flux surface labelled by $r$. The profile of $Q_i^{\mathrm{exp}}$ as a function of $r$ is shown in Figure 2.4. In this work, we normalise the heat flux to the gyro-Bohm value defined by

$$Q_{\mathrm{gB}} = n_i T_i v_{\mathrm{th}i}\frac{\rho_i^2}{a^2}. \tag{2.7}$$

From Figure 2.4, we find that the experimental level of heat flux at $r = 0.8$ is $Q_i^{\mathrm{exp}}/Q_{\mathrm{gB}} = 2 \pm 1$.

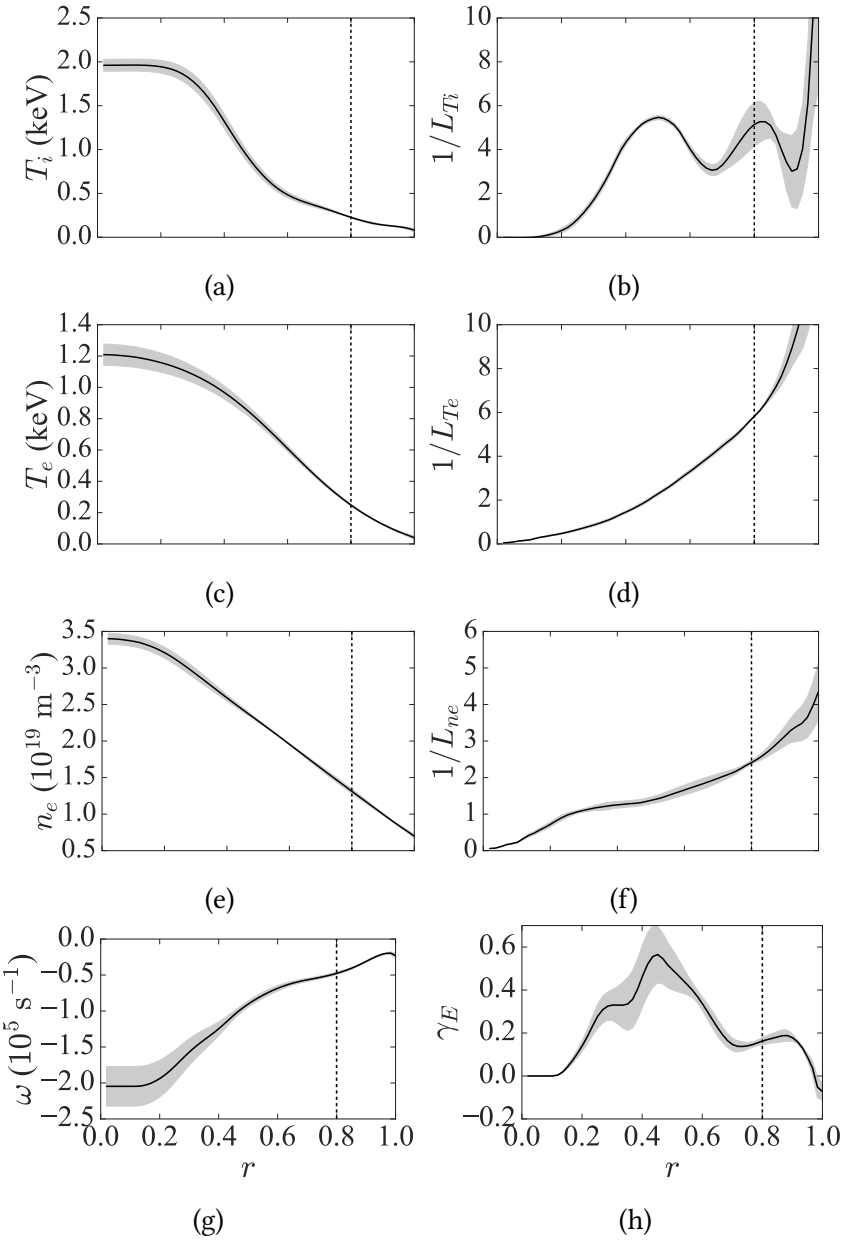



Figure 2.3: Radial profile measurements from MAST discharge #27274 (see Section 2.2.3) of (a) the ion temperature, $T_i$, (b) the ion temperature gradient, $1/L_{Ti}$, calculated using (2.3), (c) the electron temperature, $T_e$, (d) the electron temperature gradient, $1/L_{Te}$, calculated using (2.4), (e) the electron density, $n_e$, (f) the electron density gradient, $1/L_{ne}$, calculated using (2.5), (g) the toroidal angular frequency, $\omega$, and (h) the flow shear, $\gamma_E$, calculated using (2.6). The dashed line in each plot indicates $r = 0.8$ and the shaded regions indicate the standard deviation of the profiles over a 20-ms time window around $t = 0.25$ s.

Table 2.2: Equilibrium values for MAST discharge #27274 at $t = 0.25$ s.

| Name | Value |
|---|---|
| Electron density $n_e(= n_i)$ | $1.31 \times 10^{19}$ m$^{-3}$ |
| Electron temperature $T_e$ | $0.24$ keV |
| Half diameter of LCFS $a$ | $0.58$ m |
| Ion gyroradius $\rho_i$ | $6.08 \times 10^{-3}$ m |
| Ion temperature $T_i$ | $0.22$ keV |
| Toroidal magnetic field $B_\phi(r = 0)$ | $0.46$ T |
| Toroidal angular frequency $\omega$ | $4.71 \times 10^4$ s$^{-1}$ |

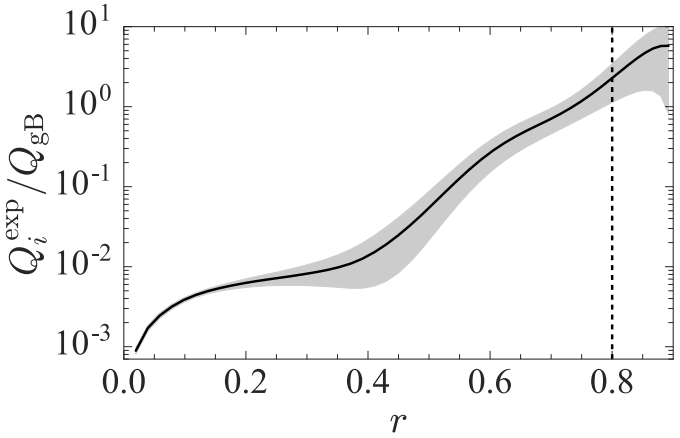



Figure 2.4: Experimental ion heat flux determined from power balance by the TRANSP analysis code as a function of $r$. The dashed line indicates $r = 0.8$ and the shaded region indicates the uncertainty estimated by TRANSP.

### 2.2.5 Sign of $\omega$ and $\gamma_E$

Determining the appropriate sign of $\gamma_E$ is essential when running numerical simulations and comparing with experimental measurements, such as from the BES diagnostic. Given that $r_0$ and $q_0$ are positive numbers, the sign of $\gamma_E$ is completely determined by the sign of $\mathrm{d}\omega/\mathrm{d}r$, as in (2.6). The sign of $\mathrm{d}\omega/\mathrm{d}r$ is determined by the convention used

in the experiment. For MAST, the directions of $\boldsymbol{u}$ and $\boldsymbol{B}$ are defined with respect to the plasma current $\boldsymbol{I}_p$, which is in the toroidal direction at the magnetic axis [30]:

$$\mathrm{sgn}(\boldsymbol{B} \cdot \boldsymbol{I}_p) = -1, \tag{2.8}$$

$$\mathrm{sgn}(\boldsymbol{u} \cdot \boldsymbol{I}_p) = 1, \tag{2.9}$$

i.e, $\boldsymbol{B}$ and $\boldsymbol{u}$ are in opposite directions. We will be simulating this experimental configuration using the GS2 code and we employ the GS2 sign conventions, which is to define $\boldsymbol{B}$ in the direction of increasing $\phi$ [84], and determine other signs with respect to increasing $\phi$:

$$\mathrm{sgn}(\boldsymbol{B} \cdot \nabla\phi) \equiv 1 \tag{2.10}$$

$$\mathrm{sgn}(\omega) = \mathrm{sgn}(\boldsymbol{u} \cdot \nabla\phi). \tag{2.11}$$

Therefore, given that $\boldsymbol{u}$ and $\boldsymbol{B}$ are in opposite directions, $\mathrm{sgn}(\omega) = -1$ and $\mathrm{d}\omega/\mathrm{d}r > 0$, as shown in Figure 2.3(g). We conclude that for the MAST configuration we are investigating, the appropriate sign of the flow shear is

$$\mathrm{sgn}(\gamma_E) > 0. \tag{2.12}$$

## 2.3 Beam emission spectroscopy

Turbulent eddies in tokamak plasmas are anisotropic due to the strong background magnetic field [67, 69]. In the parallel direction, turbulent eddies have a length scale comparable to the system size, which in a torus is the *connection length* $qR$, i.e., $l_\parallel \sim qR \sim 1$ m [67]. In the direction perpendicular to the magnetic field, ITG-unstable turbulent structures have a typical length scale of the order of the ion gyroradius $l_\perp \sim \rho_i \sim 1$ cm. Therefore, in the plane perpendicular to the magnetic field, we are interested in two-dimensional measurements of fluctuating quantities at approximately the scale of $\rho_i$. Beam emission spectroscopy is a diagnostic technique that was developed to address this need. Specifically, the BES diagnostic on MAST [54, 55] is designed to measure ion-scale density fluctuations in a radial-poloidal plane. Density fluctuations are inferred from $\mathrm{D}_\alpha$ emission produced by the NBI beam as it penetrates the plasma. The fluctuating intensity of the $\mathrm{D}_\alpha$ emission $\delta I$, is proportional to the local plasma density at

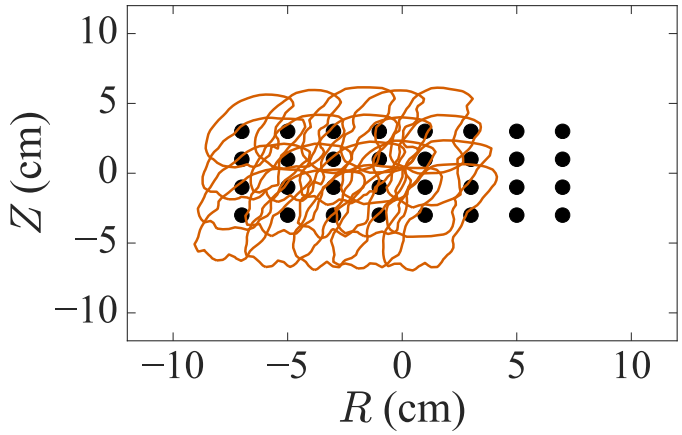



Figure 2.5: Point-spread functions for MAST discharge #27274 at $t = 0.25$ s centred around $1.35$ m. The points indicate the BES channels associated with each PSF. Approximately half of the BES is outside the plasma volume and no PSFs are calculated for those channels.

the corresponding viewing location, and the two quantities are related via point-spread functions (PSFs) [64–66],

$$\delta I_j = \int P_j(R - R_j, Z - Z_j)\delta n(R, Z)\mathrm{d}R\mathrm{d}Z, \tag{2.13}$$

where $\delta n(R, Z)$ is the fluctuating (laboratory-frame) density field, $R$ and $Z$ are the radial and poloidal coordinates, and $P_j(R - R_j, Z - Z_j)$ is the PSF for the BES channel $j$. The PSFs depend on the magnetic equilibrium, beam parameters, viewing location, and plasma profiles and as a result, have to be calculated explicitly for each measurement. The PSFs for MAST discharge #27274 at $t = 0.25$ s are shown in Figure 2.5. Note that only part of the BES is inside the plasma volume for this discharge [see Figure 2.2(b)], hence, only approximately half the PSFs are calculated. Recent work [66], has shown that the PSFs play an important role in the measurement of turbulence and the precise form that they take determines a lower bound on the BES resolution as well as affecting the measurement of the turbulent structures and density fluctuation levels – effects that we will also consider in this work. For further details on the MAST BES system the reader is referred to Ref. [54, 55, 64] and for a detailed study of the effect of PSFs on the measurement of turbulent structures to Ref. [66].

# Chapter 3

# *Modelling plasma turbulence*

## 3.1 Introduction

To model the scenario described in Chapter 2, we use gyrokinetics. The aim of modelling plasma turbulence, using gyrokinetics or any other theoretical framework, is to predict the properties of turbulent fluctuations given a description, or measurement, of the equilibrium conditions inside a fusion device (e.g., temperatures, densities, flows, etc.). Above all, we are interested in the turbulent transport of particles, momentum, and heat due to turbulence, since this is significantly enhanced by turbulence in an experimental plasma, and can adversely affect potential fusion performance.

The gyrokinetic equation is derived from the Fokker-Planck equation; however, a number of important approximations are employed that are specifically relevant to fusion plasmas in tokamaks, and, crucially, result in a reduction of the number of phase-space dimensions from six to five. The approximations made are, in short: only considering time scales longer than the gyrofrequency, but shorter than the time scales over which the equilibrium profiles vary; only considering spatial scales which are larger than the gyroradius, but smaller than the scale over which equilibrium profiles vary; and assuming that turbulent structures are elongated along the magnetic field lines. The formulation of *local* gyrokinetics takes this approximation one step further by introducing the "local approximation": that turbulence at a given radial location depends only on the equilibrium quantities and their first derivatives at that radial location. This allows

a further reduction of computational cost. In order for this local approximation to be valid, we require that $\rho_i/a \ll 1$, where we assume that other important length scales in the system, such as $L_{Ti}$, are of the same order as $a$. For the MAST discharge and radial location described in Chapter 2, one finds $\rho_i/a \sim 1/100$, where $\rho_i \approx 6 \times 10^{-3}$ m and $a \approx 0.6$ m. While this is a reasonably small number (which we formally assume to be zero in the local formulation of gyrokinetics), previous work has shown that non-local effects can reduce the level of turbulent transport at values similar to $1/100$ [85]. To test whether non-local effects change the level of turbulence, one could run a $\rho^*$ scan using a global gyrokinetic code. There is also ongoing work to extend GS2 to include finite radial effects, such as profile variation, which may be used to test their effect on MAST turbulence.

To solve the gyrokinetic system of equations we use the local gyrokinetic GS2 code [11, 50, 84], which has been under active development since the 1990s, when the algorithm for solving the linear gyrokinetic problem was first developed. Taking advantage of the local approximation as well as of the axisymmetric nature of tokamak plasmas, GS2 solves the gyrokinetic equation in a region known as a "flux tube", a thin radial region that follows the magnetic field where equilibrium quantities and their first derivatives are assumed be constant.

This chapter is organised as follows. In Section 3.2, we review the toroidal geometry relevant to plasmas in tokamak devices and define an appropriate coordinate system. In Section 3.3, we give an overview of gyrokinetics and the approximations that are required to derive the gyrokinetic equation. In Section 3.4 we give an overview of the GS2 code along with parts of the implementation that are relevant to our study. Finally, we give the specific numerical setup for the study that is the main purpose of this work in Section 3.5.

## 3.2 Toroidal geometry

In a tokamak, magnetic field lines lie on nested toroidal surfaces of constant $\psi$ called flux surfaces. These surfaces are roughly axisymmetric, and in such cases one may write

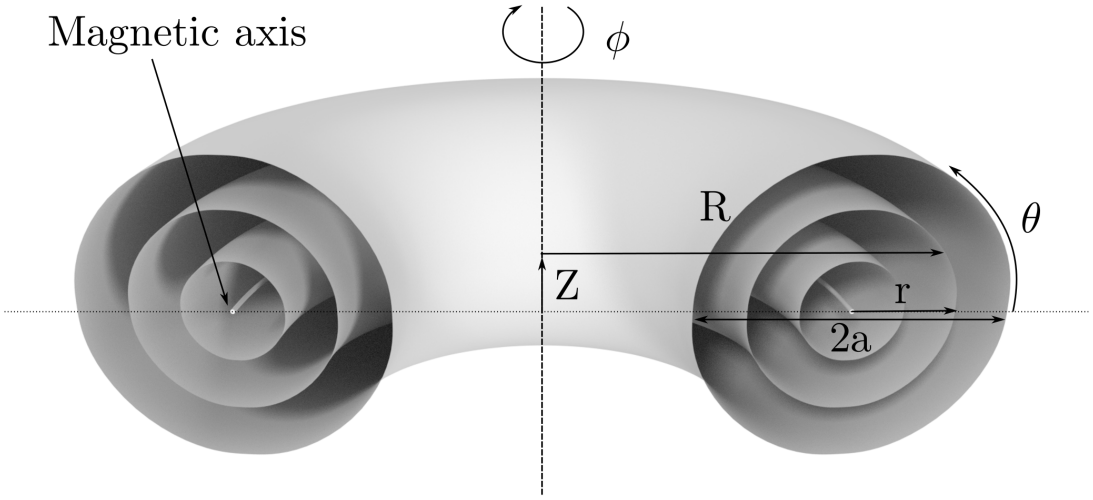



Figure 3.1: Illustration of circular nested flux surfaces of constant $\psi$ highlighting the axisymmetric toroidal geometry of a tokamak. Also shown is the magnetic axis (which need not be at the geometric centre of any flux surface for a finite Shafranov shift), the major radius $R$, the poloidal height $Z$ above the midplane of the machine, the minor radius $r$, the diameter of the LCFS at the height of the magnetic axis $2a$, the toroidal angle $\phi$, and the poloidal angle $\theta$.

the magnetic field as:

$$\boldsymbol{B} = B_\phi R \nabla\phi + \nabla\psi \times \nabla\phi, \tag{3.1}$$

where $B_\phi$ is the toroidal component of the magnetic field. Figure 3.1 is an illustration of the nested flux surfaces of constant $\psi$ in a system with circular flux surfaces, along with the coordinates we will use in this work: the major radius $R$, the poloidal height $Z$ above the midplane of the machine, the toroidal angle $\phi$, the minor radius $r$ (which is simply the distance from the magnetic axis in the case of concentric circular flux surfaces, but $r = D/2a$ in the case of more complicated flux surface shapes, such as MAST), the diameter of the LCFS at the height of the magnetic axis $2a$, and the poloidal angle $\theta$. The LCFS is the flux surface just inside the separatrix which separates flux surfaces with open and closed field lines [see Figure 2.2(b)].

## 3.3 Local gyrokinetic description

Gyrokinetics [47–49] describes the time-evolution of turbulent plasma in the toroidal geometry described in Section 3.2. The derivation of the gyrokinetic equation has been extensively covered and the reader is referred to Ref. [49], and references therein, for a detailed review. In this section, we will provide only an overview.

### 3.3.1 The Fokker-Planck equation

Our starting point is the Fokker-Planck equation that describes the evolution of the distribution function of species $s$, $f_s$. In simplified terms, $f_s$ is the probability that there is a particle of species $s$ at a given location $\boldsymbol{r}$ and travelling at a given speed $\boldsymbol{v}$. The Fokker-Planck equation for the evolution of $f_s$ is given by

$$\frac{\partial f_s}{\partial t} + \boldsymbol{v} \cdot \nabla f_s + \frac{Z_s e}{m_s}\left(\boldsymbol{E} + \frac{1}{c}\boldsymbol{v} \times \boldsymbol{B}\right) \cdot \frac{\partial f_s}{\partial \boldsymbol{v}} = C[f_s], \tag{3.2}$$

where $Z_s e$ is the charge of species $s$ as a multiple of the fundamental charge $e$, $m_s$ is the mass of species $s$, $c$ is the speed of light, $\boldsymbol{E}$ and $\boldsymbol{B}$ are the electric and magnetic fields, respectively, and $C[f_s]$ is the Landau collision operator. In theory, one could solve (3.2) directly; however, $f_s(t, \boldsymbol{r}, \boldsymbol{v})$ is a six-dimensional function (plus time) and solving (3.2) is impractical for the conditions of a magnetically confined fusion plasma. The gyrokinetic description makes several simplifying assumptions and, importantly, reduces the number of dimensions from six to five, resulting in a more tractable problem.

### 3.3.2 The gyrokinetic orderings and assumptions

We start by splitting $f_s$ into an equilibrium part $F_s$, and a fluctuating part $\delta f_s$:

$$f_s = F_s + \delta f_s. \tag{3.3}$$

We then make the following assumptions:

- perturbations of the distribution function and background electric and magnetic fields are small compared to their equilibrium values;

- the frequency of the turbulent fluctuations, $\omega_{\mathrm{turb}}$, is small compared to the frequencies at which the particles gyrate around the magnetic field $\Omega_s$, but large compared to the rate at which the equilibrium quantities change $\tau_E^{-1}$;

- the turbulent structures are anisotropic and, as such, vary more quickly across magnetic field lines compared to along the magnetic field; and

- the spatial scale of the turbulence perpendicular to the magnetic field is of the order of the gyroradius $\rho_s$, and is much smaller than the scale over which the equilibrium quantities vary, $a$.

We define the gyrokinetic parameter as

$$\epsilon_{\mathrm{GK}} \equiv \frac{\rho_i}{a}, \tag{3.4}$$

and impose the following order on the small parameters identified above [47, 49]:

$$\frac{|\delta \boldsymbol{B}|}{|\boldsymbol{B}|} \sim \frac{|\delta \boldsymbol{E}|}{|\boldsymbol{E}|} \sim \frac{\delta f_s}{f_s} \sim \frac{k_\parallel}{k_\perp} \sim \frac{\omega_{\mathrm{turb}}}{\Omega_i} \sim \frac{\rho_i}{a} = \epsilon_{\mathrm{GK}}, \tag{3.5}$$

where $k_\parallel$ and $k_\perp$ are the typical parallel and perpendicular wavelengths of the turbulence, respectively, and $\Omega_i = Z_i e B / m_i c$ is the gyrofrequency of the ions.

As this point we translate into a frame rotating with the plasma at velocity $\boldsymbol{u}$. Following from the above assumptions, it can be shown that, to lowest order in $\epsilon_{\mathrm{GK}}$, $\boldsymbol{u}$ is in the toroidal direction and independent of the species. It is defined such that

$$\boldsymbol{u} = \omega(\psi) R^2 \nabla \phi. \tag{3.6}$$

We now convert from $(\boldsymbol{r}, \boldsymbol{v})$ to the following variables, which reflect the roughly helical motion of the particles in the plasma, and the conserved quantities of that motion: the guiding-centre position $\boldsymbol{R}_s$, the particle energy $\varepsilon_s$, the magnetic moment $\mu_s$, the

gyrophase $\xi$, and the sign of the parallel velocity $\sigma$:

$$\boldsymbol{R}_s = \boldsymbol{r} - \frac{\hat{\boldsymbol{b}} \times \boldsymbol{w}}{\Omega_s} \tag{3.7}$$

$$\varepsilon_s = \frac{1}{2} m_s w^2 \tag{3.8}$$

$$\mu_s = \frac{m_s w_\perp^2}{2B} \tag{3.9}$$

$$\sigma = \frac{w_\parallel}{|w_\parallel|} \tag{3.10}$$

where $\hat{\boldsymbol{b}} = \boldsymbol{B}/B$ is a unit vector in the direction of the magnetic field, $w = |\boldsymbol{w}|$ is the velocity shifted into the rotating frame [49]

$$\boldsymbol{w} = \boldsymbol{v} - \boldsymbol{u} = w_\parallel + w_\perp(\cos\xi \boldsymbol{e}_2 - \sin\xi \boldsymbol{e}_1), \tag{3.11}$$

$w_\parallel$ and $w_\perp$ are the parallel and perpendicular components of $\boldsymbol{w}$, and $\boldsymbol{e}_1$ and $\boldsymbol{e}_2$ are arbitrary orthogonal unit vectors perpendicular to the magnetic field.

Finally, we will formally assume that the Mach number $M$ of the plasma rotation is small, but that the flow shear is large enough to affect the plasma dynamics:

$$\frac{R\omega}{v_{\mathrm{th}i}} \equiv M \ll 1, \quad |a\nabla \ln \omega| \sim \frac{1}{M}. \tag{3.12}$$

This allows us to formulate local gyrokinetics on a rotating surface, neglecting effects such as the Coriolis and centrifugal force, but retaining the effect of flow shear.

### 3.3.3 The gyrokinetic equation

Using the gyrokinetic orderings (3.5) and assuming that the plasma is sufficiently collisional, it can be shown that the background distribution function of species $s$, $F_s$, is a Maxwellian distribution, to lowest order,

$$F_s = F_{Ms} \equiv n_s \left(\frac{m_s}{2\pi T_s}\right)^{3/2} \exp\left(-\frac{\varepsilon_s}{T_s}\right), \tag{3.13}$$

where $n_s$ and $T_s$ are the density and temperature of species $s$, respectively. Furthermore, it may be shown that, to the first order in $\epsilon_{\mathrm{GK}}$, the fluctuating part of the perturbed

distribution function $\delta f_s$ can be written

$$\delta f_s = -\frac{Z_s e\varphi}{T_s} F_{Ms} + h_s(t, \boldsymbol{R}_s, \mu_s, \varepsilon_s, \sigma), \tag{3.14}$$

where $\varphi$ is the perturbed electrostatic potential and $h_s(t, \boldsymbol{R}_s, \mu_s, \varepsilon_s, \sigma)$ is the gyrophase-independent distribution function of Larmor rings that will completely determine the plasma dynamics in the gyrokinetic formulation. As $h_s$ is independent of the gyrophase, we have effectively removed one of the velocity space dimensions (with velocity space now described only by $\varepsilon_s$ and $\mu_s$) and reduced the problem to five dimensions instead of six, and in doing so, significantly reduced the computational requirements.

Applying the gyrokinetic orderings to the Fokker-Planck equation (3.2), we obtain the gyrokinetic equation, which describes the evolution of the gyrophase-independent distribution function $h_s$

$$\begin{aligned}\left(\frac{\partial}{\partial t} + \boldsymbol{u}\cdot\nabla\right)\left(h_s - \frac{Z_s e\left\langle\varphi\right\rangle_{\boldsymbol{R}s}}{T_s}F_s\right) + \left(w_\parallel \hat{\boldsymbol{b}} + \boldsymbol{V}_{\mathrm{D}s} + \left\langle \boldsymbol{V}_E\right\rangle_{\boldsymbol{R}s}\right)\cdot\nabla h_s - \left\langle C[h_s]\right\rangle_{\boldsymbol{R}s} \\ = -\left\langle \boldsymbol{V}_E\right\rangle_{\boldsymbol{R}s}\cdot\nabla r\left[\frac{\mathrm{d}\ln n_s}{\mathrm{d}r} + \left(\frac{\varepsilon_s}{T_s} - \frac{3}{2}\right)\frac{\mathrm{d}\ln T_s}{\mathrm{d}r} + \frac{m_s w_\parallel}{T_s}\frac{RB_\phi}{B}\frac{\mathrm{d}\omega}{\mathrm{d}r}\right]F_{Ms},\end{aligned} \tag{3.15}$$

where $\left\langle\ldots\right\rangle_{\boldsymbol{R}s}$ is an average over the particle orbit at constant guiding centre position $\boldsymbol{R}_s$,

$$\boldsymbol{V}_{\mathrm{D}s} = \frac{c}{Z_s e B}\hat{\boldsymbol{b}}\times\left[m_s w_\parallel^2 \hat{\boldsymbol{b}}\cdot\nabla\hat{\boldsymbol{b}} + \mu_s\nabla B\right] \tag{3.16}$$

is the magnetic drift velocity,

$$\boldsymbol{V}_E = \frac{c}{B}\hat{\boldsymbol{b}}\times\nabla\varphi \tag{3.17}$$

is the perturbed $\boldsymbol{E}\times\boldsymbol{B}$ drift velocity, and $C[h_s]$ is the linearised collision operator [86, 87].

To close our system of equations, we use the quasineutrality condition

$$\sum_s Z_s\delta n_s = 0 \quad\Rightarrow\quad \sum_s \frac{Z_s^2 e\varphi}{T_s} n_s = \sum_s Z_s\int \mathrm{d}^3\boldsymbol{w}\left\langle h_s\right\rangle_{\boldsymbol{r}}, \tag{3.18}$$

where $\left\langle\ldots\right\rangle_{\boldsymbol{r}}$ indicates a gyroaverage at constant $\boldsymbol{r}_s$, to calculate $\varphi$ using $h_s$.

The right-hand side of (3.15) represents the advection by the gyroaveraged $\boldsymbol{E}\times\boldsymbol{B}$ velocity of the Maxwellian equilibrium distribution function, which is characterised

by $n_s$, $T_s$, and $\omega$. The equilibrium quantities $n_s$, $T_s$, and $\omega$ are functions only of the poloidal magnetic flux $\psi$. However, for the purposes of this work, we have converted this dependence from $\psi$ to the Miller coordinate $r = D/2a$ introduced previously. Since $r$ is also a flux-surface label, it is simple to relate gradients in $\psi$ and $r$ via

$$\nabla r = \frac{\mathrm{d}r}{\mathrm{d}\psi}\nabla\psi. \tag{3.19}$$

The right-hand side of (3.15) contains terms proportional to $\mathrm{d}\ln T_s/\mathrm{d}r$ and $\mathrm{d}\omega/\mathrm{d}r$, which are related to the parameters $\kappa_T$ and $\gamma_E$, defined by (2.3) and (2.6), respectively. These terms are sources of free energy in the system and are responsible for the ITG and PVG instabilities. The stabilising effect of $\gamma_E$ on $h_s$ is contained in the term proportional to $\boldsymbol{u}\cdot\nabla$ and is further discussed in Section 3.3.4. In deriving (3.15), we have also assumed that the fluctuations are purely electrostatic, i.e., no fluctuating magnetic fields (see Section 3.5 for further details).

### 3.3.4 Flow shear stabilisation

*This section is based on Appendix A of Ref. [38].*

As noted in Section 3.3.3, flow shear enters (3.15) as a *destabilising* term on the right-hand side, but for the values of $\gamma_E$ that we will be considering, this effect is small compared to the destabilising effect of the ITG (see [38] for further details). However, flow shear also enters our system as a *stabilising* term, as we will now explain using a simplified magnetic geometry.

Consider a locally straight and uniform magnetic field that has constant magnitude, no curvature, and no shear. We define a local Cartesian coordinate system with unit vectors (note we do note use these definitions throughout this work, we define a related but slightly different coordinate system in Section 3.4):

$$\hat{\boldsymbol{x}} = \frac{\nabla\psi}{B_\theta R}, \qquad \hat{\boldsymbol{y}} = \frac{\hat{\boldsymbol{z}}\times\nabla\psi}{B_\theta R}, \qquad \hat{\boldsymbol{z}} = \hat{\boldsymbol{b}}. \tag{3.20}$$

We choose our local coordinate $x$ such that $x = 0$ at some reference flux surface labelled by $\psi_0$. In the vicinity of this flux surface, we may then Taylor expand $\psi$ in terms of this

local radial coordinate as $\psi(x) \approx \psi(x=0) + x\,\mathrm{d}\psi/\mathrm{d}x = \psi_0 + xB_\theta R$. The toroidal angular frequency is a function of $\psi$ only and we can again Taylor expand in $x$ (since we assume in (3.12) that the scale over which $\omega$ changes is much smaller than $a$) to get $\omega \approx \omega_0 + xB_\theta R\,\mathrm{d}\omega/\mathrm{d}\psi$. Now consider the $\boldsymbol{u}\cdot\nabla$ term on the left-hand side of (3.15), where $\boldsymbol{u}$ is given by (3.6). Using the axisymmetric representation of the magnetic field in a torus (3.1), we can write

$$\boldsymbol{u} = \omega R^2 \nabla\phi \approx \left(\omega_0 R + xB_\theta R^2 \frac{\mathrm{d}\omega}{\mathrm{d}\psi}\right)\left(\frac{B_\phi}{B}\hat{\boldsymbol{b}} + \frac{B_\theta}{B}\hat{\boldsymbol{y}}\right), \tag{3.21}$$

If we now go to the frame rotating with the flux surface at the rate $\omega_0$ and also use the fact that, in gyrokinetics, gradients of fluctuating quantities parallel to $\hat{\boldsymbol{b}}$ are always small compared to those perpendicular to it, we find

$$\boldsymbol{u}\cdot\nabla \approx x\frac{B_\theta^2 R^2}{B}\frac{\mathrm{d}\omega}{\mathrm{d}\psi}\hat{\boldsymbol{y}}\cdot\nabla = \left(\frac{qRB_\theta}{rB}|\nabla r|\right) x\gamma_E \frac{v_{\mathrm{th}i}}{a}\hat{\boldsymbol{y}}\cdot\nabla, \tag{3.22}$$

with $\gamma_E$ as defined in (2.6). The prefactor enclosed in the parentheses is close to unity and so $\gamma_E$ is the normalised shear that acts on the distribution function. The presence of this shear will have a stabilising effect on the turbulence.

## 3.4 Overview of GS2

In this work, we used the local gyrokinetic code GS2[1] [11, 50, 84] to solve the system of equations given by (3.15) and (3.18) to give us the time evolution of $h_s(t, \boldsymbol{R}_s, \varepsilon_s, \mu_s, \sigma)$ and $\varphi(t, \boldsymbol{R}_s)$. With knowledge of $h_s$ and $\varphi$, one can calculate a range of physical characteristics of the turbulence, e.g., density-, flow-, temperature-fluctuation fields, particle, momentum, and heat transport, and so on. Of particular interest is the ion density fluctuation field,

$$\frac{\delta n_i}{n_i} = \frac{1}{n_i}\int \mathrm{d}^3\boldsymbol{w}\,\langle h_i\rangle_{\boldsymbol{r}}\,, \tag{3.23}$$

and the radially outwards, time-averaged turbulent heat flux carried by the ions (for reasons which have been given previously),

$$Q_i = \left\langle \frac{1}{V}\int \mathrm{d}^3\boldsymbol{r}\int \mathrm{d}^3\boldsymbol{w}\frac{m_i v^2}{2} h_i \boldsymbol{V}_E\cdot\nabla r\right\rangle, \tag{3.24}$$

[1] `http://gyrokinetics.sourceforge.net`

where $V$ is the volume enveloping a given flux surface and $\langle \ldots \rangle$ is a flux-surface average. $Q_i$ can be normalised to the gyro-Bohm heat flux given in (2.7). It is a feature of the asymptotic ordering on which gyrokinetic theory is based that $Q_i/Q_{\mathrm{gB}}$ is a number of order unity [49].

In this section, we will review aspects of the GS2 code that are pertinent to our study. The geometry of the nested flux surfaces in GS2 is described by the Miller specification [79], which is detailed in Section 3.4.1. The Miller specification consists of nine parameters that control the aspects of the magnetic field lines and flux-surface shapes such as the safety factor, elongation, triangularity, and so on. In Section 3.4.1, we define the coordinate system relative to the magnetic flux surfaces used in GS2. By making the "local approximation" (Section 3.4.1), GS2 is able to solve the gyrokinetic equation on a single flux surface in a region known as a flux tube, which follows a single magnetic field line described by the Miller parameters. In Section 3.4.2, we detail the calculation of the ion-ion and electron-ion collision frequencies from equilibrium parameters and show how we can account for enhanced ion-ion collisionality due impurity ions without treating them as additional kinetic species in our simulations. The implementation of flow shear and its effect on turbulence is detailed in Section 3.4.3. Finally, we show the form of hyperviscosity used in GS2 to damp plasma dynamics at large values of $k_\perp$ and explain how this is beneficial in our simulations. For a detailed review of the algorithms and numerical implementations that are used in GS2 to solve the gyrokinetic equation, the reader is referred to [84], and references therein.

### 3.4.1 Geometry

#### The Miller flux-surface specification

Throughout this work we have used the Miller specification [79] of the magnetic equilibrium. The Miller specification is a nine-parameter parametrisation of up-down symmetric flux surfaces suitable for the description of MAST flux surfaces[2]. Table 3.1 lists the definitions of the Miller parameters. As explained in Section 2.2.3, experimental flux surfaces from MAST were obtained from an MSE-constrained EFIT equilibrium, or more conveniently, from a TRANSP output file, where TRANSP used the EFIT equilib-

Table 3.1: The Miller parametrisation of flux surfaces along with their associated variable names in the TRANSP output file. The derivatives of geometric quantities are calculated by manually taking a derivative with respect to $r$ (after transforming from the TRANSP $\rho_{\mathrm{tor}}$ grid onto an $r$ grid).

| Name | Definition | TRANSP variable |
|---|---|---|
| Elongation | $\kappa$ | ELONG |
| Elongation derivative | $\kappa' = \mathrm{d}\kappa/\mathrm{d}r$ | $\mathrm{d}/\mathrm{d}r$ (ELONG) |
| Magnetic shear | $\hat{s} = r_0/q_0\ \mathrm{d}q/\mathrm{d}r$ | $r_0/q_0\ \mathrm{d}/\mathrm{d}r$ (Q) |
| Major radius | $R_N = R/a$ | RMAJM$/a$ |
| Miller radial coordinate | $r_0 = D/2a$ | calc. using RMAJM |
| Safety factor | $q_0 = \partial\psi_{\mathrm{tor}}/\partial\psi_{\mathrm{pol}}$ | Q |
| Shafranov Shift | $1/a\ \mathrm{d}R/\mathrm{d}r$ | $1/a\ \mathrm{d}/\mathrm{d}r$ (RMJMP) |
| Triangularity | $\delta$ | TRIANG |
| Triangularity derivative | $\delta' = \mathrm{d}\delta/\mathrm{d}r$ | $\mathrm{d}/\mathrm{d}r$ (TRIANG) |

rium as input. For reference, we also list in Table 3.1 the associated variable names of the Miller parameters as they are listed or calculated from the TRANSP analysis output. The Miller parameter values and associated GS2 input parameters for our study are detailed, along with other equilibrium parameters, in Section 3.5.

### GS2 Coordinate system

We saw in Section 3.2 that the magnetic field lines in a tokamak form well-defined, nested flux surfaces of constant magnetic field and, hence, constant $\psi$. As well as this, magnetic field lines, in the absence of magnetic islands and other similar effects (the typical configuration in a tokamak), do not cross each other. Therefore, we can use these two observations to define a coordinate system, following Ref. [84, 89].

The first natural basis vector is the direction of the magnetic field, $\hat{\boldsymbol{b}} = \boldsymbol{B}/B$. As stated in Section 3.3, equilibrium quantities are functions only of the poloidal flux $\psi$

[2]For the specification of up-down *asymmetric* flux surfaces the reader is referred to recent work by Ball *et. al.* [88] that extends the Miller specification.

because that they are constant on a given flux surface (no poloidal dependence) and that the system is axisymmetric (no toroidal dependence). Therefore, we can use the gradient of $\psi$ to define the radial coordinate with basis vector:

$$\hat{\boldsymbol{\psi}} = \frac{\nabla\psi}{|\nabla\psi|}. \tag{3.25}$$

Finally, we define a third coordinate, $\alpha$, with basis vector

$$\hat{\boldsymbol{\alpha}} = \frac{\nabla\alpha}{|\nabla\alpha|}, \tag{3.26}$$

such that $\boldsymbol{B} = \nabla\alpha \times \nabla\psi$ (using the Clebsch representation of the magnetic field [90]). It was shown in [90] that $\alpha$ is a function of the form

$$\alpha = \phi + q(\psi)\theta + \nu(\theta, \psi), \tag{3.27}$$

where $\nu$ is a function which depends on the geometry and is periodic in $\phi$ and $\theta$ [90].

### The local approximation

Using the above coordinate system we define the coordinates used in GS2 after employing the "local approximation". Due to the fast motion of particles along the magnetic field lines and the relatively slow drift across them, turbulent structures are anisotropic in the parallel and perpendicular directions to the field line. Specifically, turbulent structures in a tokamak are elongated along field lines, with length scales of the order of the connection length $l_{\parallel} \sim qR$, and are much shorter in the perpendicular directions, with length scales of the order of the ion gyroradius $l_{\perp} \sim \rho_i$. GS2 takes advantage of this anisotropy by solving the gyrokinetic equation in a region known as a "flux tube" [89]. A flux tube is chosen to be several turbulence decorrelation lengths long in both the perpendicular and parallel directions, i.e., long enough to avoid spurious interactions of turbulence with the edges of the box, but still short enough to be highly resolved. Figure 3.2 shows the MAST flux surface and magnetic field lines at $r = 0.8$ with one field line highlighted in red to represent a flux tube. The actual flux tube is approximately rectangular at the outboard midplane and is highly twisted along the field line due to the magnetic shear (this is not shown in Figure 3.2 for clarity). Assuming axisymmetry,

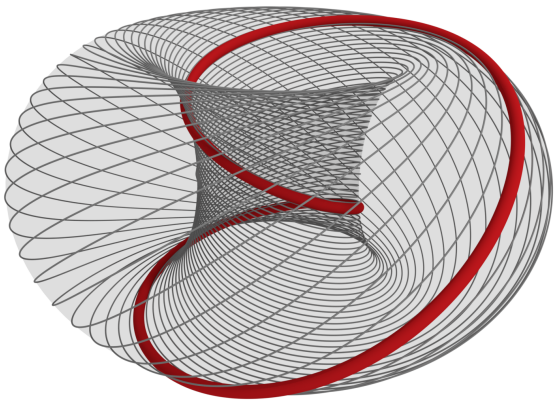


Figure 3.2: Magnetic field lines that lie on the flux surface at $r = 0.8$ (setting $q = 2$ so that field lines are closed for visualisation purposes). The field line marked in red is the centre line of the GS2 flux tube that we use to simulate the plasma. The GS2 flux tube itself is approximately rectangular at the outboard midplane but twists as it follows the magnetic field line due to the magnetic shear. The flux tube follows the field line once around the flux surface in the poloidal direction.

along with the anisotropy of the fluctuations, implies that we are in fact capturing the dynamics of the entire flux surface. Simulating only a single flux tube in this way leads to dramatic savings in computational cost.

The local approximation in gyrokinetics assumes that the gradients of equilibrium quantities (such as those shown in Figure 2.3) are constant across the radial simulation domain. It is also assumed that, provided the simulation domain in the plane perpendicular to the magnetic field is significantly larger than the spatial scales of the turbulence, it is acceptable to take periodic boundary conditions in the radial and binormal directions. For these two directions, the two perpendicular coordinates used in GS2 are $x$ and $y$, which measure the distance from the magnetic field line located at $(\psi_0, \alpha_0)$ [84]:

$$x = a\frac{q_0}{r_0}(\psi_N - \psi_{0N}), \tag{3.28}$$

$$y = a\left.\frac{\mathrm{d}\psi_N}{\mathrm{d}r}\right|_{r_0}(\alpha - \alpha_0), \tag{3.29}$$

where $\psi_N = \psi/a^2 B_{\mathrm{ref}}$ is the normalised poloidal flux. In the parallel direction, the poloidal angle $\theta$ is used in GS2 (noting that any coordinate that is not fixed at fixed

$\psi$ and $\alpha$ can be used as a parallel coordinate and noting in addition, some geometric quantities are more convenient to calculate when using $\theta$ as a parallel coordinate [84]).

### Spectral coordinates

In the absence of flow shear, the gyrokinetic equation (3.15) has no explicit dependence on $x$ or $y$ and can be solved using spectral methods in these directions. Spectral methods are computationally efficient and can be used to enforce the conservation properties required by the system exactly. More specifically, GS2 uses a pseudo-spectral algorithm with only the nonlinear term being calculated in $(x, y, \theta)$ coordinates. Otherwise, perturbed quantities have the following spectral representation [89]

$$A = \sum_{k_x, k_y} \hat{A}(t, \theta)_{k_x, k_y} e^{i(k_x x + k_y y)} \equiv \mathcal{F}^{-1}[\hat{A}(t, \theta)], \tag{3.30}$$

where $k_x$ and $k_y$ are the perpendicular coordinates used by GS2 in spectral space, and $\mathcal{F}^{-1}$ is the inverse Fourier transform.

One important caveat regarding the use of spectral coordinates and the conversion of GS2 perturbed quantities from spectral to real space (as we do in this work) is the normalisation convention used when performing the Fourier transform. GS2 uses the open-source FFTW[3] package to transform between $(x, y)$ and $(k_x, k_y)$ representations. FFTW performs the following calculations[4]:

$$\text{Forward: } \hat{A}(k) = \mathcal{F}[A(x)] = \sum_{j=0}^{n-1} A_j e^{-2\pi jki/n}, \tag{3.31}$$

$$\text{Backward: } A(x) = \mathcal{F}^{-1}[\hat{A}(k)] = \sum_{j=0}^{n-1} \hat{A}_j e^{2\pi jki/n}, \tag{3.32}$$

where $A$ is the real-space representation, $\hat{A}$ is the spectral-space representation, and $\mathcal{F}$ is the forward Fourier transform. We see that there is no implicit normalisation applied by the FFTW library, meaning that applying a forward (going from real to spectral space)

[3] http://www.fftw.org/

[4] http://www.fftw.org/doc/What-FFTW-Really-Computes.html

Table 3.2: Normalising quantities used in GS2.

| Quantity | Definition |
|---|---|
| $a$ | Half the diameter of the LCFS at the height of the magnetic axis |
| $B_{\mathrm{ref}}$ | Toroidal magnetic field strength at $r = 0$ |
| $v_{\mathrm{th}i}$ | $\sqrt{2T_i/m_i}$ |
| $Z_i \equiv 1$ | Charge number of ion species |
| $m_i$ | Mass of ion species |
| $\Omega_i$ | $Z_i e B_{\mathrm{ref}}/m_i c$ |
| $\rho_i$ | $v_{\mathrm{th}i}/\Omega_i$ |

and then a backward (going from spectral to real space) transform will multiply the input by $n$. Therefore, the following normalisation is commonly used:

$$\hat{A}(k) = \mathcal{F}[A(x)], \tag{3.33}$$

$$A(x) = \frac{\mathcal{F}^{-1}[\hat{A}(k)]}{n}. \tag{3.34}$$

In contrast, GS2 uses the following normalization:

$$\hat{A}(k) = \frac{\mathcal{F}[A(x)]}{n}, \tag{3.35}$$

$$A(x) = \mathcal{F}^{-1}[\hat{A}(k)]. \tag{3.36}$$

In other words, when converting GS2 fields from spectral space to real space, no normalisation is necessary and care must be taken when using FFT packages external to GS2 since they may be using the normalisations given in equations (3.31) and (3.32).

### GS2 variable Normalisations

Before detailing aspects of the GS2 algorithm, we note the normalisations used in GS2 and this work. The normalisations used within GS2 are chosen such that all quantities are of order unity. Table 3.2 lists the normalising quantities and Table 3.3 lists the main normalised quantities used within GS2 [84].

Table 3.3: The main normalised quantities used in this work [84].

| Name | Normalised definition |
|---|---|
| Binormal coordinate | $y/\rho_i$ |
| Binormal wavenumber | $k_y\rho_i$ |
| Charges | $Z_s/Z_i$ |
| Densities | $n_s/n_i$ |
| Density gradients | $\kappa_{ns} = 1/L_{ns}$ |
| Flow shear | $\gamma_E = (r_0/q_0)\,\mathrm{d}\omega/\mathrm{d}r\;(a/v_{\mathrm{th}i})$ |
| Magnetic field | $B/B_{\mathrm{ref}}$ |
| Masses | $m_s/m_i$ |
| Perturbed electrostatic potential | $\varphi/(\rho_i/a)(T_i/e)$ |
| Radial coordinate | $x/\rho_i$ |
| Radial wavenumber | $k_x\rho_i$ |
| Temperatures | $T_s/T_i$ |
| Temperature gradients | $\kappa_{Ts} = 1/L_{Ts}$ |
| Time | $t/(a/v_{\mathrm{th}i})$ |

### 3.4.2 Collisions

The fundamental effect of turbulence is to transfer energy from large spatial scales at which energy is injected to small scales where energy is dissipated, which leads to heating. As well as the transfer of energy due to turbulence, there are several mechanisms that lead to phase-space mixing, which produce small-scale structure and large gradients in velocity space (see [91] and references therein). It is these large gradients in velocity space that eventually bring collisions into effect regardless of how small the collisionality is. Therefore, in any plasma turbulence simulation some form of dissipation must be included to smooth out the small-scale structure that develops in velocity space. While dissipation due to collisions is the primary physical dissipation mechanism in kinetic plasmas, artificial dissipation is also possible, and useful, in numerical simulations (see Section 3.4.4).

Recent work [86, 87] has led to the implementation of a linearised Fokker-Planck collision operator in GS2 that satisfies the following important properties, (i) smooths out small-scale structure in velocity space; (ii) obeys Boltzmann's H-theorem (the condition that collisional processes are irreversible and cannot decrease entropy); and (iii) conserves particles, momentum, and energy. This collision operator includes the effect of both pitch-angle scattering and energy diffusion because small-scale structure can be generated in both $v_\perp$ and $v_\parallel$ by phase mixing. The level of collisional dissipation in GS2 is set by the collision frequencies calculated as follows.

In GS2, velocity space is represented by the particle energy $\varepsilon_s$ and the pitch-angle variable $\lambda_s' = \mu_s/\varepsilon_s$. The associated input parameters which control the grid sizes are `negrid` and `ngauss`. These parameters are only related to the real grid sizes used by GS2, because the exact magnetic geometry also plays a role through the calculation of bounce points of trapped particles (see Ref. [84] for further details). The input parameters that control the strength of the collisional dissipation in GS2 are the collision frequencies for each species. The electron-ion collisionality is calculated via [86, 92]

$$\texttt{vnewk_2} = \nu_{ei}\frac{a}{v_{\mathrm{th}i}} = \frac{4\pi n_e e^4 \ln\Lambda}{(2T_e)^{3/2} m_e^{1/2}}\frac{a}{v_{\mathrm{th}i}}, \tag{3.37}$$

where [93]

$$\ln\Lambda = 24 - \ln\left(10^4\sqrt{\frac{n_e^{1/2}}{10}}T_e^{-1}\right), \tag{3.38}$$

is the Coulomb logarithm where $n_e$ is in units of $10^{19}$ m$^{-3}$ and $T_e$ is in keV, and `vnewk_2` is the GS2 parameter denoting the electron collision frequency. We can derive a convenient form of (3.37) by converting to cgs units and eliminating physical constants [92]:

$$\texttt{vnewk_2} \approx 2.7913\times 10^{-3}\frac{n_e \ln\Lambda a A_i^{1/2}}{T_e^{3/2}T_i^{1/2}}, \tag{3.39}$$

where $A_i$ is the atomic mass of the ion species in units of the proton mass $m_p$ and $T_i$ is in units of keV.

In this work, we have simulated only a single ion species. However, the experiment contains several different ion impurities, such as $C^{+6}$ carbon impurity ions, and

beam ions, that may affect the ion equilibrium profiles and ion-ion collision frequencies. Unfortunately, including additional gyrokinetic ion species in our simulations is prohibitively expensive for the extensive parameter scan performed in this work. Instead, it is possible to improve the realism of our simulations by creating an aggregate ion species, instead of simulating a pure deuterium plasma. We achieve this by calculating an effective ion charge,

$$Z_{\text{eff}} = \frac{\sum_j n_j Z_j^2}{|\sum_j n_j Z_j|}, \tag{3.40}$$

where the summation is over all ion species present in the experiment, and $n_j$ and $Z_j$ are the density and charge of ion species $j$, respectively. This parameter is denoted `zeff` in GS2 and the value, determined from the experiment, is given in Section 3.5. This leads to the following enhancement of the ion-ion collision frequency [92]

$$\texttt{vnewk_1} = \texttt{vnewk_2} \times Z_i^2 Z_{\text{eff}} \left(\frac{m_e}{m_i}\right)^{1/2} \left(\frac{T_e}{T_i}\right)^{3/2}, \tag{3.41}$$

where `vnewk_1` is the GS2 parameter denoting the ion-ion collision frequency. The calculated values for the above collision frequencies that were inputs to our simulations are listed in Table 3.4 in Section 3.5.

### 3.4.3 Real-space effect of flow shear

Flow shear is implemented in GS2 by allowing $k_x$ to vary with time [94]:

$$k_x^*(t) = k_x - \gamma_E k_y t. \tag{3.42}$$

In simplified terms, GS2 shifts the fluctuation fields along the $k_x$ dimension as a function of time (see [84] for a complete review of the GS2 flow shear algorithm). This leads to finer radial structure and a displacement of fluctuations in the $y$ direction, as illustrated in Figure 3.3. However, complications arise in this implementation as a result of the fixed $k_x$ grid in GS2, which causes jumps in the displacement of fluctuations in the $y$ direction at the radial extremes of the box as we will now explain.

When $k_x^*$ changes by $\delta k_x = \gamma_E k_y \Delta t$, where $\Delta t$ is a GS2 time step, the value of the GS2 fluctuation fields at $k_x$ would ideally be shifted to $k_x \pm \delta k_x$. However, the $k_x$ grid is

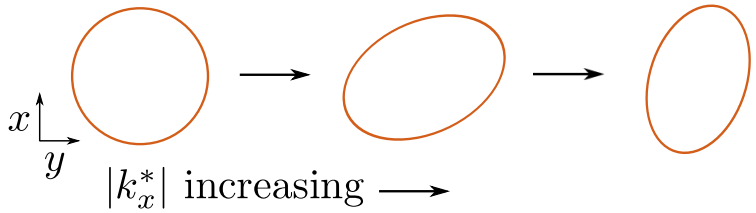



Figure 3.3: Illustration of the effect of flow shear of turbulent structures. As $k_x^*$ increases in time there is increased radial structure and displacement in the $y$ direction.

fixed in GS2 (with a grid separation of $\Delta k_x$) and so the fluctuation fields must be shifted by at least $\Delta k_x$. This issue is resolved in GS2 by keeping track of the difference between the exact shift in $k_x$ and the grid spacing $\Delta k_x$: when the exact shift is less than $\Delta k_x/2$, no shifting takes place but the value is recorded and added to the size of the shift at the next time step. This process is repeated until the shift is greater than or equal to $\Delta k_x/2$, at which point all fluctuation fields are shifted by $\Delta k_x$.

The distribution function calculated by GS2 is of the form

$$h \sim \exp[i(k_x^* x + k_y y)]. \tag{3.43}$$

Substituting for $k_x^*$ using (3.42), we get $h \sim \exp[i(k_x x + k_y y - \gamma_E k_y x t)]$ and we can identify the wave frequency $\omega_h = \gamma_E k_y x$ to calculate the group velocity

$$\boldsymbol{v}_g = \partial\omega_h/\partial\boldsymbol{k} = -\gamma_E x \hat{\boldsymbol{y}}. \tag{3.44}$$

Writing $\boldsymbol{v}_g = \Delta y/\Delta t$, we find the displacement of fluctuations in the $y$ direction, for an ideal $k_x$ shift of $\delta k_x = \gamma_E k_y \Delta t$,

$$\Delta y = -\frac{\delta k_x x}{k_y}. \tag{3.45}$$

However, $\delta k_x$ is forced to match the fixed $k_x$ grid with a spacing $\Delta k_x = 2\pi/L_x$, where $L_x$ is the size of the box in the $x$ direction. Using $k_y = 2\pi/\lambda_y$, where $\lambda_y$ is the wavelength of a given $k_y$ mode, we can finally write the displacement due to the flow shear as,

$$\Delta y = \lambda_y \frac{x}{L_x}. \tag{3.46}$$

This means that at the edges of the radial domain, where $x = \pm L_x/2$, the displacement in the $y$ direction for every shift in $k_x$ due to the flow shear is $\Delta y = \pm \lambda_y/2$. The rate of shifting is dependent on $k_y$ according to (3.42) and so the largest modes (smallest $k_y$s) will be acted on more infrequently than smaller modes (larger $k_y$s). However, the largest modes are then shifted by half the size of their wavelength according to (3.46). This causes visual separation (or multiplication) of structures at the edges of the GS2 domain in real space in a way that may affect our correlation analyses performed in Chapter 5.

We emphasise that the separation of turbulent structures we have described above is only present in the real-space representation of the GS2 distribution function. Given that GS2 performs calculations (apart from the calculation of nonlinear interactions) in Fourier space, this does not present a problem to the overall calculation. We note that the implementation of flow shear in GS2 is correct in the limit of infinitely small $\Delta k_x$ and so it is sufficient to check convergence with $\Delta k_x$ to be confident of our results. Ideally, some form of interpolation could be used to smooth out these shifts in $k_x$ and a future program of work is planned to implement this in GS2.

### 3.4.4 Implementation of hyperviscosity

In addition to the dissipation caused by collisions (see Section 3.4.2), it is possible to dissipate energy artificially at moderately small spatial scales, rather than having to resolve the entire spatial cascade of energies. However, this has to be done in such a way so as not to affect the turbulent transport that we are trying to predict by running simulations. The benefit of such artificial dissipation is that it allows us to damp the dynamics at small scales where we do not expect the contribution to the transport to be large, but would require significant computational resources to resolve (see Appendix A). Hyperviscosity is one such technique for artificially damping turbulent dynamics at small scales (large wavenumbers). Whereas collisional dissipation acts on large gradients in velocity space, hyperviscosity directly damps large wavenumbers.

The GS2 implementation is based on a 2D Smagorinsky-like hyperviscosity subgrid model [95]. It is a fourth-order damping model applied to the non-adiabatic part of the distribution function at every time step, with the result that a perturbed quantity like

the electrostatic potential $\varphi$ is multiplied at each time step by

$$\exp\left[-D_{\mathrm{hv}} S \Delta t \left(\frac{k_\perp}{k_{\perp,\max}}\right)^4\right], \tag{3.47}$$

where $D_{\mathrm{hv}}$ is a constant coefficient controlling the strength of the hyperviscosity (denoted by `d_hypervisc` in GS2), $k_\perp^2 = k_x^2 + k_y^2$, $k_{\perp,\max}$ is the largest perpendicular wavenumber in the simulation, and $S$ is the $x$-$y$ averaged shearing rate, defined in terms of the perturbed $\boldsymbol{E} \times \boldsymbol{B}$ drift velocity $\boldsymbol{V}_E = (c/B)\hat{\boldsymbol{b}} \times \nabla \langle\varphi\rangle_{\boldsymbol{R}_s}$ as [95]

$$\begin{aligned} S^2(\theta) &= \left\langle \left(\frac{\mathrm{d}V_{Ex}}{\mathrm{d}x}\right)^2 + \left(\frac{\mathrm{d}V_{Ey}}{\mathrm{d}y}\right)^2 + \frac{1}{2}\left(\frac{\mathrm{d}V_{Ex}}{\mathrm{d}x} + \frac{\mathrm{d}V_{Ey}}{\mathrm{d}y}\right)^2 \right\rangle_{x,y} \\ &= \sum_{k_x}\sum_{k_y} k_\perp^4 \frac{c}{B}|\varphi|^2, \end{aligned} \tag{3.48}$$

where $\langle\cdots\rangle_{x,y}$ indicates an average over $x$-$y$ space. We see that the damping rate in (3.47) is a function of $k_\perp$ and thus damps large wavenumbers most strongly.

Equation (3.48) shows that the damping due to hyperviscosity depends on the amplitude of $\varphi$. This is beneficial when focusing on nonlinear simulations since it reduces the importance of choosing the right value of $D_{\mathrm{hv}}$, i.e., the damping rate will change dynamically with the amplitude of the plasma dynamics. However, it complicates the study of the linear dynamics, where the amplitude of $\varphi$ grows exponentially in time – with the implication that hyperviscous damping would have an ever-increasing effect. Whereas in a saturated nonlinear simulation, the damping due to hyperviscosity would be roughly constant (since $\varphi$ is roughly constant). For this reason, there are two methods for using hyperviscosity in GS2, controlled by the input flag `const_amp`:

- `const_amp = True`: The shearing rate (3.48) $S = 1$ and the level of damping will only depend on the value of $D_{\mathrm{hv}}$ and the wavenumber.
- `const_amp = False`: The level of damping will depend on the fluctuation amplitude of $\varphi$ via (3.48).

In this work, we are interested in both the linear and nonlinear behaviour, and so our simulations were all run with `const_amp = False`. This allows us to study linear

growth rates and be sure they are relevant to our nonlinear simulations. When using hyperviscosity, it is important to study its effect on linear growth rates and turbulent transport. We investigate this in Appendix A and show that by damping electron spatial scales we are able to keep simulations resolutions modest while not significantly affecting the turbulent transport. This was further tested by sensitivity scan for nonlinear simulations: assessing that the precise value of $D_{\mathrm{hv}}$ did not affect any measured quantities.

## 3.5 Numerical set-up

The MAST equilibrium parameters used in our simulations were extracted from the MAST diagnostics and EFIT equilibrium, as explained in Section 2.2. In practise, these diagnostic measurements and equilibria are cleaned and serve as input to a TRANSP analysis to calculate the transport coefficients. As a result, the output from a TRANSP analysis contains all the information necessary to run GS2 simulations. To extract these parameters, an open-source, and freely available package[5] was developed that reads a TRANSP output file and calculates all the required GS2 parameters. The equilibrium parameters at $r = 0.8$ and $t = 0.25$ s, for the MAST discharge #27274 we will be investigating in this work, are listed in Table 3.4. The two nominal experimental values for the parameters we vary in this study were $\kappa_T = 5.1 \pm 1$ and $\gamma_E = 0.16 \pm 0.02$; however, we also scanned outside the region of experimental uncertainty in order to map out the turbulence threshold more fully. Overall, our parameter scan consisted of 76 simulations over the regions $\kappa_T \in [4.3, 8.0]$ and $\gamma_E \in [0, 0.19]$. Figure 3.4 shows the parameter values for the full parameter scan in this study, where the highlighted region indicates parameters that lie within the experimental uncertainty. Due to resolution constraints, we were not able to simulate between $0 < \gamma_E \lesssim 0.08$ (as explained in Appendix B).

Previous investigations [30, 35] of similar MAST discharges have found that electrons play an important role in driving turbulence in MAST, even at ion scales. Our study confirmed these findings: in Appendix C we present a series of linear simulations with $\gamma_E = 0$ while varying $\kappa_T$. We show that the maximum linear growth rates at ion

[5] https://github.com/ferdinandvanwyk/transp_to_gs2

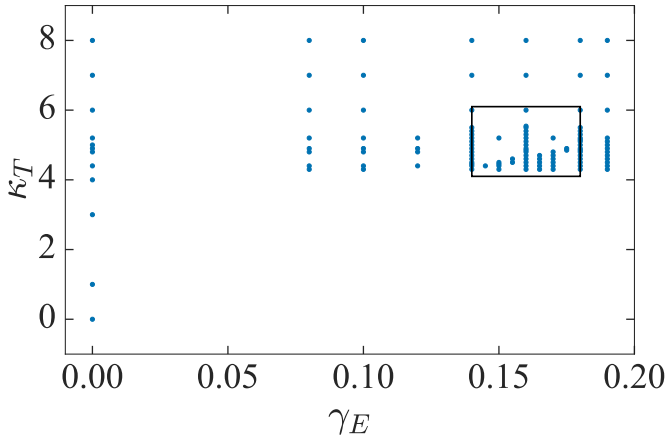



Figure 3.4: Equilibrium values of $\kappa_T$ and $\gamma_E$ for the parameter scan in this study. The highlighted region indicates the region of experimental uncertainty. Simulations in the region $0 < \gamma_E < 0.08$ were not reliable due to resolution constraints (see main text).

scales for simulations with a kinetic electron species is $\sim$ 2–3 times larger than linear simulations with adiabatic electrons. Initial simulations with adiabatic electrons confirmed that sustained turbulence required $\kappa_T$ significantly higher than even the upper estimate based on the experimental uncertainties. Accordingly, we have included electrons in our simulations as a kinetic species. Given that our simulations contained only two kinetic species (deuterium ions and electrons), it follows from the quasineutrality condition that they must have the same density and density gradient, i.e., $n_i = n_e$ and $L_{ni} = L_{ne}$.

Previous work investigating electromagnetic effects in MAST plasmas [96, 97], found that electromagnetic effects were only significant at $r \sim 0.5$, where $\beta \geq 0.1$. In the outer-core region we consider in this work, where $\beta \sim 0.005$, these effects are not significant and we are thus able to assume the plasma is electrostatic.

We determined the appropriate grid sizes for our nonlinear simulations using the results from the linear simulations without flow shear presented in Appendix A and C. Without hyperviscosity, we found strong linear growth at both ion and electron scales without a clear separation – suggesting expensive multiscale simulations are required. However, we are only interested in ion scales (given that the BES diagnostic measures turbulent dynamics at this scale), while still including the effect of kinetic electrons.

Therefore, we have made use of hyperviscosity and show in Appendix A that we can truncate our nonlinear simulations at $k_y\rho_i \gtrsim 2$, where we have chosen $k_y\rho_i \sim 3$, and verified that changes in this cut-off scale or the number of $k_y$ modes (where we were only able to test with $\sim 20\%$ more $k_y$ modes due to cost constraints) do not significantly affect the turbulence.

In the $x$ direction, we have chosen our grid based on the grid spacing $\Delta k_x$ such that we could resolve reasonably small values of $\gamma_E$ (as explained above and in Section 3.4.3). Again, we have verified that changes in $k_{x,\max}$ or the number of $k_x$ modes (where we increased the number by $50\%$) do not significantly affect the turbulence. In both the $x$ and $y$ directions, we chose the truncation scale to be somewhat higher than necessary to ensure a sufficient "inertial range" between the injection and dissipation scales and such that favourable parallelisation was achieved when decomposing our grids over supercomputing nodes.

In the parallel direction we chose the smallest grid that adequately resolved the eigenfunction and ensured that it reached very small values at the edges of the parallel domain. The cost of GS2 simulations is a strong function of the parallel resolution and so minimising parallel resolution was key to being able to run such a large numerical study.

In velocity space, we again chose grid sizes as small as possible in order to minimise computational cost. We tested this by ensuring that the velocity-space integrals had small errors when velocity-space grid points were added or taken away.

Table 3.5 lists the GS2 resolution input parameters used for our nonlinear simulations. We note that the pseudo-spectral method employed by GS2 requires additional Fourier modes to prevent aliasing [98]. As a result, the number of physical grid points were $85 \times 32 \times 20$ in the radial, binormal, and parallel directions (while the number of grid points in the code was $128 \times 96 \times 20$), and $27 \times 16$ pitch-angle and energy-grid points, respectively. We chose the box sizes in $x$ and $y$ to be $L_x \approx 200\rho_i$ and $L_y \approx 62\rho_i$, respectively, while $\theta \in [-\pi, \pi]$. We note that while $L_x$ is comparable to the size of MAST, the turbulence predicted by GS2 can only be compared to experimental MAST turbulence at $r = 0.8$. All of the GS2 parameters summarised in this section can be found in the example GS2 input file in Appendix F.

Table 3.4: GS2 equilibrium parameters calculated from diagnostic measurements and from the EFIT equilibrium of the MAST discharge #27274 and appropriately normalised. The nominal experimental values for $\kappa_T$ and $\gamma_E$ are $\kappa_T = 5.1 \pm 1$ and $\gamma_E = 0.16 \pm 0.02$. The reference magnetic field is the toroidal magnetic field strength at the magnetic axis, i.e., $B_{\text{ref}} = B_\phi(r = 0)$. See Appendix F for an example GS2 input file with these parameters.

| Quantity | GS2 variable | Value |
|---|---|---|
| $\beta = 8\pi n_i T_i / B_{\text{ref}}^2$ | `beta` | 0.0047 |
| $\beta' = \partial\beta/\partial r$ | `beta_prime_input` | -0.12 |
| Eff. ion charge $Z_{\text{eff}} = \sum_i n_i Z_i^2 / \lvert\sum_i n_i Z_i\rvert$ | `zeff` | 1.59 |
| Elec.-ion collisionality $\nu_{ei}$ | `vnewk_2` | 0.59 |
| Elec. density $n_{eN} = n_e/n_i$ | `dens_2` | 1.00 |
| Elec. density grad. $1/L_{ne} = -\,\mathrm{d}\ln n_e/\mathrm{d}r$ | `fprim_2` | 2.64 |
| Elec. mass $m_{eN} = m_e/m_i$ | `mass_2` | $1/(2 \times 1836)$ |
| Elec. temp. $T_{eN} = T_e/T_i$ | `temp_2` | 1.09 |
| Elec. temp. grad. $1/L_{Te} = -\,\mathrm{d}\ln T_e/\mathrm{d}r$ | `tprim_2` | 5.77 |
| Elongation $\kappa$ | `akappa` | 1.46 |
| Elongation derivative $\kappa' = \mathrm{d}\kappa/\mathrm{d}r$ | `akappri` | 0.45 |
| Flow shear $\gamma_E = (r_0/q_0)\,\mathrm{d}\omega/\mathrm{d}r\;(a/v_{\text{th}i})$ | `g_exb` | [0, 0.19] |
| Ion collisionality $\nu_i$ | `vnewk_1` | 0.02 |
| Ion density $n_{iN} = n_i/n_i$ | `dens_1` | 1.00 |
| Ion density grad. $1/L_{ni} = -\,\mathrm{d}\ln n_i/\mathrm{d}r$ | `fprim_1` | 2.64 |
| Ion mass $m_{iN} = m_i/m_i$ | `mass_1` | 1.00 |
| Ion temp. $T_{iN} = T_i/T_i$ | `temp_1` | 1.00 |
| Ion temp. grad. $\kappa_T \equiv 1/L_{Ti} = -\,\mathrm{d}\ln T_i/\mathrm{d}r$ | `tprim_1` | [4.3, 8.0] |
| Magnetic shear $\hat{s} = r_0/q_0\,\mathrm{d}q/\mathrm{d}r$ | `s_hat_input` | 4.00 |
| Magnetic field reference point $R_{\text{geo}}$ | `r_geo` | 1.64 |
| Major radius $R_N = R/a$ | `rmaj` | 1.49 |
| Miller radial coordinate $r_0 = D/2a$ | `rhoc` | 0.80 |
| Safety factor $q_0 = \partial\psi_{\text{tor}}/\partial\psi_{\text{pol}}$ | `qinp` | 2.31 |
| Shafranov Shift $1/a\;\mathrm{d}R/\mathrm{d}r$ | `shift` | -0.31 |
| Triangularity $\delta$ | `tri` | 0.21 |
| Triangularity derivative $\delta' = \mathrm{d}\delta/\mathrm{d}r$ | `tripri` | 0.46 |

Table 3.5: Resolution parameters used in our nonlinear simulations. See Appendix F for and example GS2 input file with these parameters.

| Name | GS2 variable | Value |
|---|---|---|
| No. of $k_x$ modes | `nx` | 128 |
| No. of $k_y$ modes | `ny` | 96 |
| $\theta$ grid points | `ntheta` | 20 |
| $\varepsilon_s$ grid points | `negrid` | 16 |
| $\lambda'_s$ grid points | `ngauss` | 8 |
| $x$ box size parameter | `x0` | 10 |
| $y$ box size parameter | `y0` | 10 |
| No. of $2\pi$ parallel segments | `nperiod` | 1 |
| Hyperviscosity coefficient | `d_hypervisc` | 9 |

# Chapter 4

# *Nonlinear simulations*

## 4.1 Introduction

In this chapter, we present the results of a parameter scan in $\kappa_T$ and $\gamma_E$. We focus on the prediction of the ion heat flux $Q_i$ and make comparisons with experimental estimates of the ion heat flux $Q_i^{\exp}$ calculated from TRANSP results. In a fusion reactor we would like to maximise the core temperature (and hence the temperature gradient between the edge and the core) at a given heat flux. In local simulations, the heat flux is a useful measure of the level of turbulence and we would, therefore, like to explore how the heat flux changes with the equilibrium parameters that we vary and whether our simulations are in agreement with experimental measurements. This will allow us to gain confidence in our models and eventually make predictions for the optimal parameters to maximise the fusion power for a given reactor. We exclusively vary $\kappa_T$ and $\gamma_E$, while keeping all other equilibrium quantities constant. In other words, we do not self-consistently recalculate other equilibrium quantities that would be needed to support the values of $\kappa_T$ and $\gamma_E$ that we use. However, this allows us to isolate the effect of these two parameters on MAST turbulence. We demonstrate in Section 4.2 that GS2 is able to match the experimental heat flux at equilibrium values within the experimental uncertainty and that the experiment lies close to the turbulence threshold.

We showed in Sections 3.3.3 and 3.3.4, that the ITG is a source of free energy, which drives instabilities, while flow shear has a stabilising effect on turbulence. In the ab-

sence of a background flow shear, numerical studies have suggested that ITG-unstable plasma reaches a statistically steady-state in the following way [31, 99, 100]. Linear modes are unstable due to the ITG instability and grow exponentially in time. Once the modes have sufficient amplitude, they interact nonlinearly to give rise to a turbulent state. The nonlinear interactions spontaneously generate "zonal flows" (poloidally symmetric flows with finite radial wavenumber). The zonal flows give rise to an $\boldsymbol{E} \times \boldsymbol{B}$ shear and have a suppressing effect on turbulence. When the nonlinear interaction is sufficiently suppressed, linear growth due to the ITG instability returns and the process repeats.

In the presence of a background flow shear, the situation may become more complicated. It has been shown, in simple geometries, that the turbulence can become subcritical [36, 38, 39], i.e., large initial perturbations are required to ignite turbulence, as opposed to only requiring infinitesimal perturbations in conventional supercritical turbulence. In Section 4.3, we show that the turbulence for the MAST configuration we are investigating is subcritical. We study the linear dynamics and estimate the conditions necessary to ignite turbulence, namely the transient-amplification factor and time. Studying the real-space structure of turbulence (Section 4.4), we show that coherent, long-lived structures dominate the saturated state close to the turbulence threshold. Furthermore, the fluctuations in the system have a clear minimum amplitude needed to sustain turbulence. We present a novel structure counting analysis and show that the number of turbulent structures increases rapidly as one moves away from the turbulence threshold into more strongly driven regimes. Finally, we show that far from the turbulence threshold, the turbulence is similar to turbulence in the absence of flow shear, characterised by many interacting eddies. This suggests that the observed nonlinear state dominated by coherent structures is an intermediate state between completely suppressed turbulence and the zonal-flow regulated scenarios observed in conventional ITG-unstable plasmas. We estimate the $\boldsymbol{E}\times\boldsymbol{B}$ shear due to the zonal flows (Section 4.4.5) and show that it is small compared to the background flow shear close to the turbulence threshold, but becomes comparable and eventually dominates over the flow shear far from the threshold, again resembling a system in the absence of flow shear.

## 4.2 Heat flux

We performed a parameter scan in $\kappa_T$ and $\gamma_E$ around their respective experimental values to investigate the resulting changes in turbulent transport. The experimental values and associated uncertainties were $\kappa_T = 5.1 \pm 1$ and $\gamma_E = 0.16 \pm 0.02$. However, we also performed simulations outside the experimental uncertainty ranges to aid our understanding of how the nature of the turbulence changes with $\kappa_T$ and $\gamma_E$ and, in particular, how it is different near to versus far from the (nonlinear) stability threshold. Our entire study covered $\kappa_T \in [4.3, 8.0]$ and $\gamma_E \in [0, 0.19]$ and consisted of 76 simulations. All simulations were run until they reached a statistical steady state, i.e., until the running time average became independent of time. Averages were taken over a time period of approximately $200$–$400$ $(a/v_{\mathrm{th}i})$ (which corresponds to $\sim 800$–$1600$ $\mu$s) and in many cases longer.

Figures 4.1 and 4.2 show the anomalous ion heat flux versus $\kappa_T$ and $\gamma_E$ found in our simulations. Figure 4.1 shows the full parameter scan with the rectangular region indicating the extent of the experimental errors in each equilibrium parameter. The dashed line indicates the value of experimental heat flux, $Q_i^{\mathrm{exp}}/Q_{\mathrm{gB}}$, and the shaded region the experimental uncertainty. Figure 4.1 demonstrates two of the important conclusions of this work: (i) GS2 is able to match the experimental heat flux within the experimental uncertainties of $\kappa_T$ and $\gamma_E$, and (ii) the experiment regime is located close to the turbulence threshold (defined as the separating line between the regions of parameter space with $Q_i = 0$ and $Q_i > 0$). Figure 4.2 shows part of the region of experimental uncertainty around the turbulence threshold giving the specific values of $Q_i/Q_{\mathrm{gB}}$ in each simulation. It demonstrates that transport is "stiff", i.e., that relatively small changes in the equilibrium parameters lead to large changes in $Q_i/Q_{\mathrm{gB}}$ as one moves away from the turbulence threshold. From Figure 4.2, we can identify several simulations that represent the marginally unstable cases in our parameter scan: $(\kappa_T, \gamma_E) = (4.4, 0.14), (4.8, 0.16), (5.1, 0.18)$. We will consider these parameter values when studying the conditions necessary to reach a saturated turbulent state in Section 4.3.

The plots in Figure 4.3 give another view of the data in Figure 4.1 and also demon-

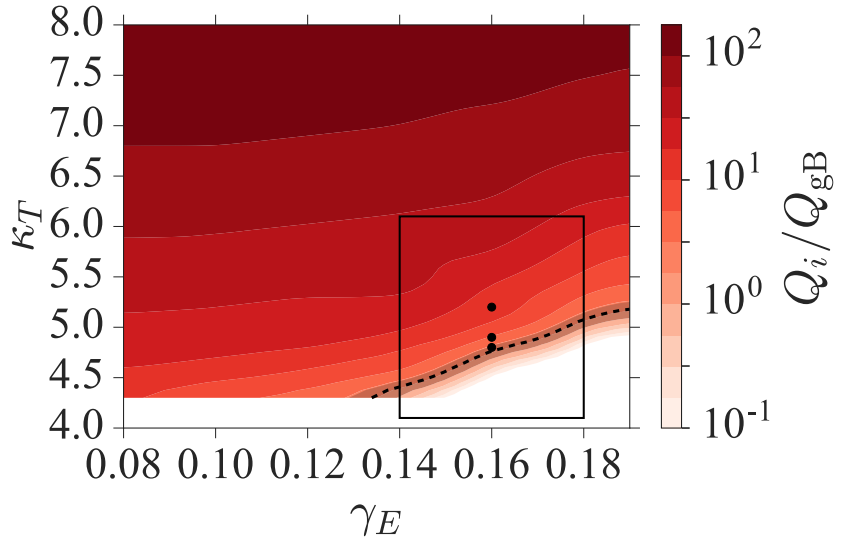



Figure 4.1: $Q_i/Q_{\mathrm{gB}}$ as a function of $\kappa_T$ and $\gamma_E$ for all simulations with $\gamma_E > 0$. The rectangular region indicates the range in $\kappa_T$ and $\gamma_E$ consistent with the experiment within measurement uncertainties. The dashed line indicates the value of $Q_i^{\mathrm{exp}}/Q_{\mathrm{gB}}$ and the shaded area the experimental uncertainty. The experiment is clearly near the turbulence threshold defined by $(\kappa_T, \gamma_E)$. The points indicate the parameter values for which the density-fluctuation fields are shown in Figure 4.10.

strate the stiffness of the transport. Figure 4.3(a) shows the values of $Q_i/Q_{\mathrm{gB}}$ for several values of $\gamma_E$ (including $\gamma_E = 0$) as a function of $\kappa_T$, whereas Figure 4.3(b) shows $Q_i/Q_{\mathrm{gB}}$ as a function of $\gamma_E$ for several values of $\kappa_T$. We see that an $O(1)$ change in $\kappa_T$ gives rise to an $O(10)$ change in $Q_i/Q_{\mathrm{gB}}$, and even more dramatically for changes in $\gamma_E$, which requires only an $O(0.1)$ change to cause $O(10)$ changes in the turbulent heat flux. The important conclusion from Figure 4.3(a) is that the presence of flow shear does not significantly affect the transport stiffness, i.e., the rate of increase of $Q_i/Q_{\mathrm{gB}}$ with respect to $\kappa_T$, but only changes the threshold value of $\kappa_T$ above which turbulence is present. This increase in critical ITG without a change in the stiffness of $Q_i/Q_{\mathrm{gB}}$ with respect to $\kappa_T$ has been observed in numerical simulations of simplified ITG-unstable plasmas in the presence of flow shear [26, 27]. It is also in agreement with experimental [17, 20] and numerical [101] findings in the outer core of the JET experiment, which also showed that ion heat transport stiffness is not affected by an increase in $\gamma_E$, but may increase

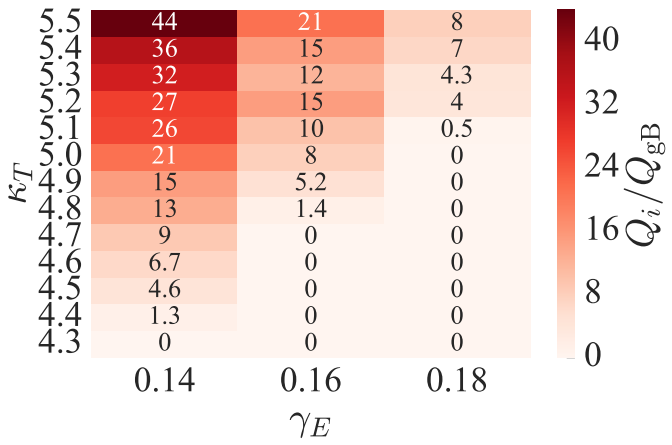
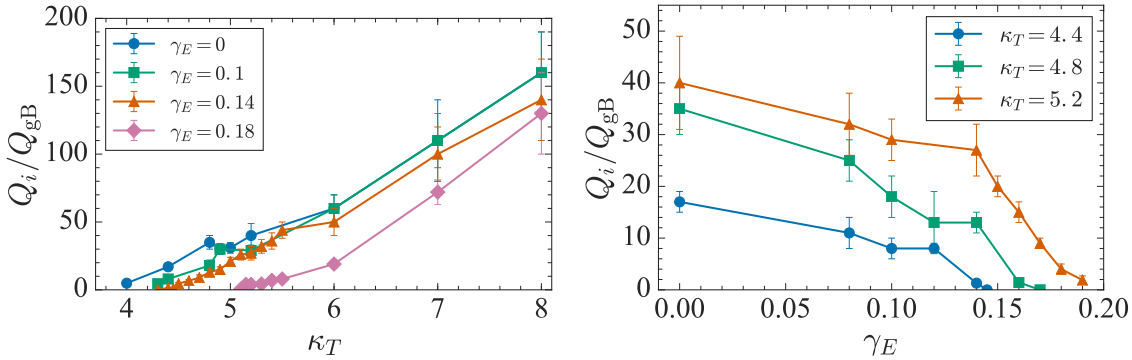



Figure 4.2: Values of the ion heat flux $Q_i/Q_{\mathrm{gB}}$ as a function of $\kappa_T$ and $\gamma_E$ for part of the region of experimental uncertainty around the turbulence threshold. It is clear that the system is subject to "stiff transport" as shown by the dramatic increase in heat flux for small changes in our equilibrium gradient stability parameters.




(a) (b)

Figure 4.3: (a) $Q_i/Q_{\mathrm{gB}}$ as a function of $\kappa_T$ for several values of $\gamma_E$ (including $\gamma_E = 0$). (b) $Q_i/Q_{\mathrm{gB}}$ as a function of $\gamma_E$ for several values of $\kappa_T$.

the critical ITG threshold.

Figure 4.4 shows $Q_i/Q_{\mathrm{gB}}$ as a function of $\kappa_T$ strictly within the region of measurement uncertainty of $\kappa_T$ and $\gamma_E$, close to the turbulence threshold. The dashed line and shaded region indicate $Q_i^{\mathrm{exp}}/Q_{\mathrm{gB}}$ and its associated uncertainty. We see that there is a range of $\kappa_T$ and $\gamma_E$ values where we might expect $Q_i/Q_{\mathrm{gB}}$ to match $Q_i^{\mathrm{exp}}/Q_{\mathrm{gB}}$, and we

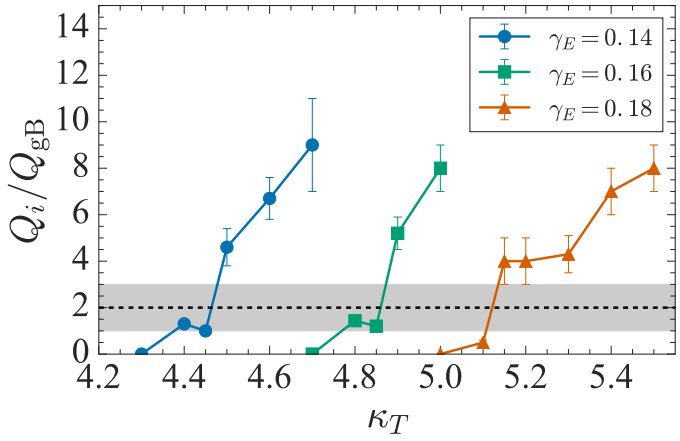



Figure 4.4: $Q_i/Q_{\mathrm{gB}}$ as a function of $\kappa_T$ strictly within experimental uncertainty of $\kappa_T$ and $\gamma_E$, and close to the turbulence threshold. The shaded region indicates the experimental heat flux $Q_i^{\mathrm{exp}}/Q_{\mathrm{gB}} = 2 \pm 1$, determined from Figure 2.4.

Table 4.1: Parameter values for simulations that match the experimental heat flux, $Q_i^{\mathrm{exp}}/Q_{\mathrm{gB}} = 2 \pm 1$.

| $\kappa_T$ | $\gamma_E$ | $Q_i/Q_{\mathrm{gB}}$ |
|---|---|---|
| 4.4 | 0.14 | $1.3 \pm 0.1$ |
| 4.45 | 0.14 | $1.0 \pm 0.1$ |
| 4.8 | 0.16 | $1.44 \pm 0.05$ |
| 4.85 | 0.16 | $1.2 \pm 0.1$ |
| 5.15 | 0.18 | $4 \pm 1$ |
| 5.2 | 0.18 | $4 \pm 1$ |

have a number of individual simulations that match the value of $Q_i^{\mathrm{exp}}/Q_{\mathrm{gB}}$. A list of these is given in Table 4.1 . We will investigate these simulations further when we make more detailed comparisons with the experiment.

## 4.3 Subcritical turbulence

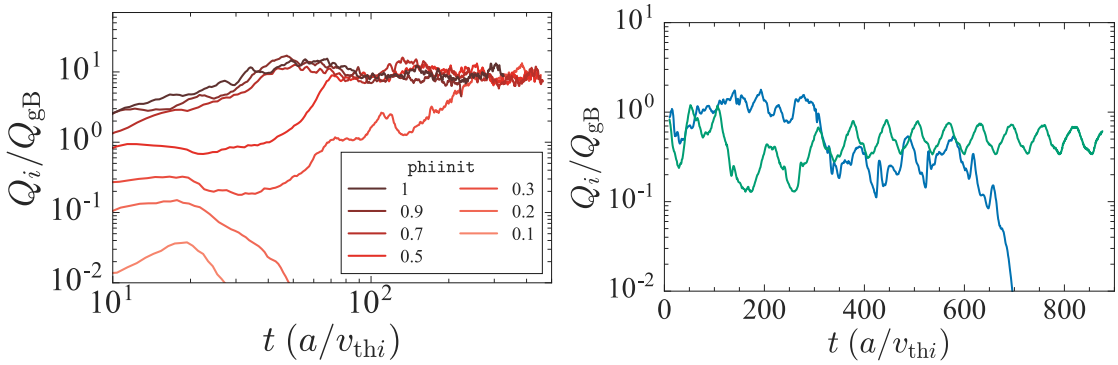
We have found that in all our simulations with $\gamma_E > 0$, a finite initial perturbation was required in order to ignite turbulence and reach a saturated turbulent state. In sub-

critical systems [38, 39, 42, 102], linear modes are formally stable, but may be transiently amplified by a given factor over a given time. If the transient amplification is sufficient for nonlinear interactions to become significant before the modes decay, then a turbulent state may persist, provided the fluctuation amplitudes do not fall below the critical values (by way of random fluctuations that characterise the turbulent state) that prevent them being transiently amplified once again to amplitudes where nonlinear interactions are dominant.

In our simulations, the amplitude of the initial condition required was found to depend on how far the system was from the turbulence threshold, i.e., simulations far from the turbulence threshold required a smaller initial perturbation because they were shown to amplify transiently growing modes by a larger factor (see below). This suggests that the turbulence threshold identified in Section 4.2 in terms of $\kappa_T$ and $\gamma_E$ is also a function of the amplitude of the initial condition. However, in this work, we have assumed that the fluctuations in the experiment (e.g., due to large-scale MHD modes or more virulent turbulence on neighbouring flux surfaces) can generate arbitrarily large perturbations as an initial condition to our system. For this reason, we have used the largest initial perturbation allowed by the numerical algorithm used in GS2 in this work, i.e., as large as possible without forcing the system to evolve the distribution function with time steps so small that the simulations would require prohibitively long simulation times. The nonlinear simulations presented in Section 4.2 were run with such large initial conditions. Thus, for the regions where we have indicated $Q_i = 0$, we could not ignite turbulence using even the largest initial condition allowed by the GS2 algorithm. We will demonstrate the subcritical nature of the turbulence in this section by investigating the effect of changing the amplitude of the initial perturbation in both linear and nonlinear simulations.

### 4.3.1 Minimum initial perturbation amplitude

GS2 initialises the distribution function (both wavenumbers and velocity space) with random complex numbers between $-0.5$ and $0.5$, and scales these numbers via the input parameter `phiinit`. We start by considering the nonlinear time evolution of $Q_i/Q_{\mathrm{gB}}$ at the nominal equilibrium parameters $(\kappa_T, \gamma_E) = (5.1, 0.16)$ varying the value of `phi-`




(a) (b)

Figure 4.5: (a) The ion heat flux $Q_i/Q_{\mathrm{gB}}$ as a function of time for different initial-condition amplitudes for $(\kappa_T, \gamma_E) = (5.1, 0.16)$, keeping all other parameters the same. (b) $Q_i/Q_{\mathrm{gB}}$ as a function of time for identical simulations at $(\kappa_T, \gamma_E) = (5.1, 0.18)$. The difference between the blue and green time series is random noise with which GS2 initialises a simulation (having again excluded the noisy initial time evolution). Beyond $t = 300\ (a/v_{\mathrm{th}i})$, the simulations seem to converge to a similar average value before one is abruptly quenched due to the amplitudes falling below the critical values required to sustain a saturated state.

`init`, shown in Figure 4.5(a). These equilibrium parameter values represent a simulation far from the turbulence threshold (see Figure 4.1) and yet, for a range of initial amplitudes, we see that the system decays rapidly. This is a clear demonstration that the turbulence is subcritical. We see that there is a certain minimum value of `phiinit` between $0.2$ and $0.3$, starting from which it is possible for the system to reach a saturated state, rather than decay. Importantly, for simulations that do reach a saturated state, the level of saturation does not depend on the amplitude of the initial perturbation. However, a large initial perturbation is not sufficient to guarantee that a subcritical system continues in a statistically steady state indefinitely, as we explain in the next section.

### 4.3.2 Finite lifetime of turbulence

In simulations with equilibrium parameters close to the turbulence threshold, we found that turbulence could be quenched at a seemingly unpredictable time. For example, Figure 4.5(b) shows the time trace of $Q_i/Q_{\mathrm{gB}}$ for two identical simulations at the

parameter values $(\kappa_T, \gamma_E) = (5.1, 0.18)$, close to the turbulence threshold. Our simulations were initialised with random noise in each Fourier mode (with `phiinit` $= 1$) and the only difference between the two simulations is the realisation of this random noise. We see the simulations saturate at a similar level beyond $t = 300\ (a/v_{\mathrm{th}i})$ before one of them abruptly decays. This is another indication that the system is subcritical: the decaying simulation has fallen below the critical amplitude to sustain turbulence. Practically, we decided that a simulation reached a saturated state if the heat flux evolved at a roughly constant value for at least $200\ (a/v_{\mathrm{th}i})$.

The finite life time of turbulence in subcritical systems is well established in some hydrodynamic systems, such as fluid flow in a pipe [103]. By running a large number of identical pipe-flow experiments [44, 104, 105] and numerical simulations [44, 103, 105, 106], it was shown that the "lifetime" of subcritical turbulence (the characteristic time it takes before turbulence decays to laminar flow) is a function of the Reynolds number. The Reynolds number in pipe flows characterises the tendency of the system to be turbulent and is used to quantify the "distance from the turbulence threshold". In particular, it was shown that the larger the value of the Reynolds number (i.e., the further the system is from the turbulence threshold), the longer the turbulence is likely to persist. More recently, this same phenomenon of finite turbulence lifetime has been observed in MHD simulations of astrophysical Keplerian shear flow systems [107], where the magnetic Reynolds number characterises the distance from threshold and the turbulence persists longer for larger values.

Given the above findings, we would also expect the turbulence to persist longer for larger values of $Q_i/Q_{\mathrm{gB}}$ in the subcritical turbulence we consider here. However, the pipe flow and astrophysical studies referred to above relied on running many experiments in order to build up sufficient statistics to determine the dependence of the turbulence lifetimes on the system parameters. Currently, we are neither able to run enough simulations nor run them for a sufficient amount of time to determine the turbulence lifetimes for our system, given the high resolutions demanded by nonlinear gyrokinetic simulations of plasmas in the core of tokamaks. However, this may be possible in future, given advances in computing and numerics or through the use of reduced models (upon being shown to be valid for this MAST regime).

### 4.3.3 Transient growth of perturbations

A system can reach a saturated turbulent state despite being stable to infinitesimal perturbations due to transient growth of perturbations. This transient growth is sufficient to sustain turbulence provided perturbations reach an amplitude sufficient for nonlinear interaction. The question we would like to answer now is how much transient growth is sufficient for the system to reach a turbulent state. We have already seen which values of $\kappa_T$ and $\gamma_E$ lead to a turbulent state (see Figure 4.1) and we now investigate transient growth of perturbations via linear GS2 simulations.

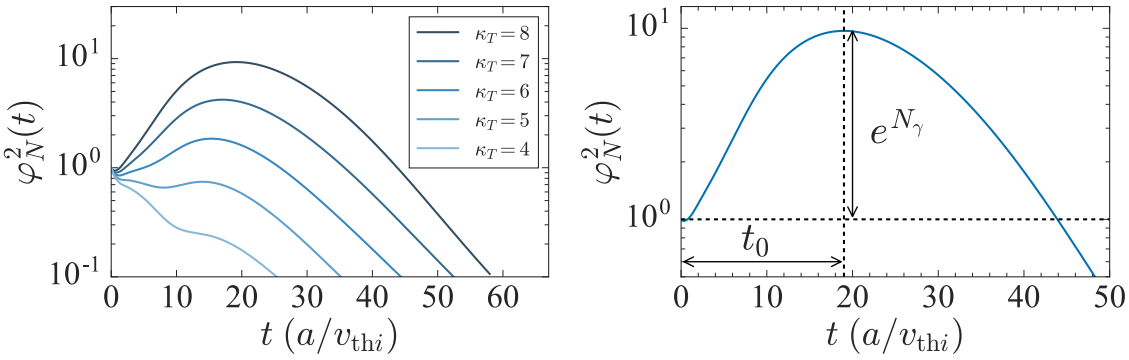
We performed an extensive series of linear simulations and calculated the time-evolution of the electrostatic potential as a function of $k_y\rho_i$, $\kappa_T$, and $\gamma_E$. Figure 4.6(a) shows the time evolution of $\varphi$ (at $k_y\rho_i = 0.2$ and $\gamma_E = 0.16$) for a range of $\kappa_T$, normalised to the value at the time when the flow shear is switched on, i.e., $\varphi^2_N(t) = \varphi^2(t)/\varphi^2(0)$, where $t = 0$ defines the time at which $\gamma_E$ is changed from $0$ to $0.16$. We have averaged $\varphi$ over $k_x$. Figure 4.6(a) illustrates the phenomenon of transient growth in a subcritical system and we see that, as $\kappa_T$ is increased, the system shows stronger transient growth. At $\gamma_E = 0.16$, we saw in Figure 4.1 that turbulence could be sustained at $\kappa_T \approx 4.8$. Figure 4.6(a) shows only a marginal amount of transient growth for $\gamma_E = 0.16$

We investigate the linear dynamics in the absence of flow shear in Appendix A and C.

### 4.3.4 Characterising transient growth

For linear simulations such as those shown in Figure 4.6(a), it is problematic to define a "linear growth rate", as we do for linear simulations with $\gamma_E = 0$, where $\varphi(t)$ grows exponentially. Methods for determining an "effective" linear growth rate have been outlined in Refs. [35] and [38]. Here, we follow Ref. [38] and use the "transient-amplification factor" as a measure of the vigour of the transient growth. For a total amplification factor, $e^{N_\gamma}$, the amplification exponent $N_\gamma$ is defined by

$$N_\gamma = \int_0^{t_0} \mathrm{d}t\gamma(t) = \frac{1}{2}\ln\frac{\varphi^2(t_0)}{\varphi^2(0)}, \tag{4.1}$$




(a) (b)

Figure 4.6: (a) Transient growth of initial perturbations of the electrostatic potential $\varphi_N^2(t)$ (normalised to the time at which flow shear is switched on ) at $\gamma_E = 0.16$, for a range of $\kappa_T$ values. These time evolutions were obtained from purely linear simulations for a binormal wavenumber $k_y\rho_i = 0.2$, approximately the wavenumber that gives the largest transient growth (see Figure 4.7(a)), and averaged over $k_x$. As $\kappa_T$ is increased, the strength of the transient growth is also increased. (b) $\varphi_N^2(t)$ as a function of time for a strongly growing mode at $(\kappa_T, \gamma_E, k_y\rho_i) = (5.1, 0.16, 0.2)$ to further illustrate transient amplification. The total amplification is given by $e^{N_\gamma}$ and the time taken to reach maximal amplification is $t_0$.

where $t_0$ is the time taken to reach the maximum amplification, and $\gamma(t)$ is the time-dependent growth rate. We note that both the transient-amplification factor and time are functions of $k_y$: $N_\gamma = N_\gamma(k_y)$ and $t_0 = t_0(k_y)$, however, we will write these as $N_\gamma$ and $t_0$ for convenience. The concept of transient growth is more clearly illustrated in Figure 4.6(b), which shows a typical linear simulation with strong amplification at $(\kappa_T, \gamma_E, k_y\rho_i) = (5.1, 0.16, 0.2)$. The total amplification $e^{N_\gamma}$ and the time taken to reach maximal amplification $t_0$, are also indicated in Figure 4.6(b).

It was shown in Ref. [38] that the parameters $N_\gamma$ and $t_0$ determine whether turbulence can be sustained in the following way. Perturbations grow transiently because they are swept from values of $k_x(t)$ that are unstable to values that are stable, where $k_x(t)$ evolves according to (3.42). If nonlinear interactions scatter energy back into the unstable modes before perturbations decay to values too small to be acted upon by the nonlinearity, they can be transiently amplified once again, and so on. In this way, a nonlinear saturated state can be sustained. The typical timescale for nonlinear interactions

is the nonlinear decorrelation time $\tau_{\mathrm{NL}} \sim 1/k_\perp V_E$, where $k_\perp$ is the typical perpendicular wavenumber, and $V_E \sim k_\perp(c\varphi/B)$ from (3.17). To sustain turbulence, transient growth should last at least as long as one nonlinear decorrelation time:

$$t_0 \gtrsim \tau_{\mathrm{NL}}. \tag{4.2}$$

At the same time, the rate of amplification should be comparable to the nonlinear decorrelation rate for a sustained turbulent state:

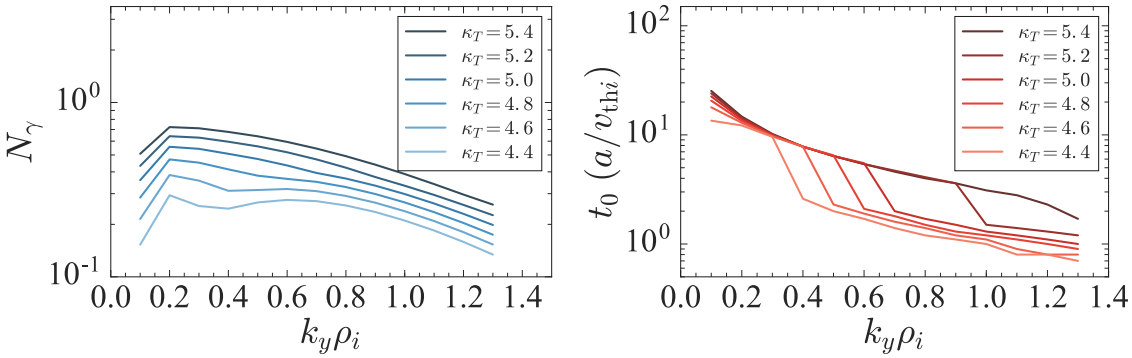
$$\frac{N_\gamma}{t_0} \sim \frac{1}{\tau_{\mathrm{NL}}}. \tag{4.3}$$

Combining (4.2) and (4.3), we see that a sustained turbulent state requires

$$N_\gamma \gtrsim 1. \tag{4.4}$$

We will now investigate the values of $N_\gamma$ and $t_0$ for experimentally-relevant equilibrium parameters and return to the comparison of $t_0$ with $\tau_{\mathrm{NL}}$ in Section 5.5 after estimating $\tau_{\mathrm{NL}}$ using the results from our correlation analysis.

Considering figures 4.6(a) and (b), we want to estimate the critical values of $N_\gamma$ and $t_0$ above which turbulence is triggered and a saturated state can be established in our system. We note that reaching a saturated state would still require a sufficiently large initial perturbation, as we showed in Figure 4.5(a). Figure 4.7 shows $N_\gamma$ and $t_0$ as functions of $k_y\rho_i$ for a range of different $\kappa_T$ values at $\gamma_E = 0.16$. The linear simulations are only shown up to $k_y\rho_i = 1.3$, because hyperviscosity effectively suppresses transient growth beyond this value (this is discussed in more detail in appendix A). As a point of reference, Figure 4.2 previously showed that for $\gamma_E = 0.16$, the transition to turbulence occurs at $\kappa_T = 4.8$. For the linear simulations in Figure 4.7, we see a relatively smooth increase in $N_\gamma$ and $t_0$ as $\kappa_T$ is increased across this nonlinear threshold. We see larger transient amplification and modes with smaller $k_y\rho_i$ experiencing amplification over a longer time period as $\kappa_T$ is increased. The fact that neither Figure 4.7(a) nor Figure 4.7(b) show significant changes as the nonlinear turbulence threshold is passed suggests that nonlinear simulations are essential for predicting whether the system will exhibit turbulence for this experimental configuration.



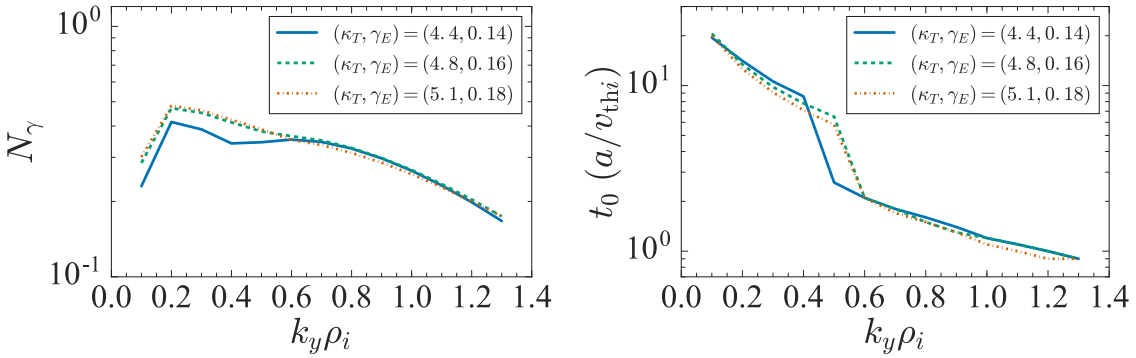

(a) (b)

Figure 4.7: (a) The transient-amplification factor $N_\gamma$ (4.1) for a range of values of $\kappa_T$ at $\gamma_E = 0.16$. $N_\gamma$ increases with increasing $\kappa_T$ and increases smoothly as the nonlinear threshold is passed. (b) Time taken to reach maximum amplification $t_0$ for a range of values of $\kappa_T$, also at $\gamma_E = 0.16$. Increasing $\kappa_T$ leads to transient amplification lasting for a longer time.

### 4.3.5 Conditions for the onset of subcritical turbulence

For supercritical turbulence, the onset of turbulence is typically characterised by a critical value of the linear growth rate. Similarly, for subcritical systems, we may reasonably expect that critical values of $N_\gamma$ and/or $t_0$ exist that lead to a saturated turbulent state. To investigate the conditions for the onset of turbulence we consider $N_\gamma$ and $t_0$ for the marginally unstable simulations identified in Section 4.2. Figures 4.8(a) and (b) show $N_\gamma$ and $t_0$ as functions of $k_y\rho_i$ for $(\kappa_T, \gamma_E) = (4.4, 0.14), (4.8, 0.16), (5.1, 0.18)$. We see that both $N_\gamma$ and $t_0$ are roughly the same for our marginally unstable simulations, suggesting that the values shown in Figures 4.8(a) and (b) are the critical values necessary for the onset of turbulence. Assuming that low $k_y$ modes are the dominant scales in the system, it is reasonable to estimate from Figures 4.7(b) and 4.8(b) that the onset of turbulence requires $t_0 \gtrsim 10\ (a/v_{\mathrm{th}i})$.

To determine a critical condition for $N_\gamma$, we consider the value at the peak of the $N_\gamma$ spectrum, $k_y\rho_i \sim 0.2$, shown in Figure 4.7(a). Figure 4.9 shows the maximum value of the transient-amplification factor $N_{\gamma,\mathrm{max}}$, as a function of $\kappa_T$. The marked simulations are for the critical values of $\kappa_T$ above which turbulence can be sustained, given a sufficiently




(a) (b)

Figure 4.8: (a) Transient-amplification factor $N_\gamma$ and (b) transient-amplification time $t_0$ for the three marginal simulations identified in Section 4.2. The values of $N_\gamma$ and $t_0$ that correspond to the marginally unstable equilibria are approximately the same, suggesting that these are the critical values required in order to reach a saturated turbulent state.

large initial perturbation amplitude. Figure 4.9 shows that $N_{\gamma,\max}$ is linear in $\kappa_T$ for each $\gamma_E$, with higher values of $\gamma_E$ resulting in lower values of $N_{\gamma,\max}$. The other important feature is that the values of $N_{\gamma,\max}$ at the critical values of $\kappa_T$ are similar, giving an approximate critical condition: $N_{\gamma,\max} \sim 0.4$. We can conclude that, for the system we are investigating, the conditions for the onset of turbulence (given a sufficiently large initial perturbation) are:

$$\begin{aligned} N_{\gamma,\max} &\gtrsim 0.4, \\ t_0 &\gtrsim 10\ (a/v_{\mathrm{th}i}). \end{aligned} \tag{4.5}$$

The value of $N_{\gamma,\max}$ in (4.5) is comparable to that found in previous work [38, 102]. We will return to the comparison of $t_0$ with $\tau_{\mathrm{NL}}$ after estimating $\tau_{\mathrm{NL}}$ in Section 5, where we confirm that $t_0 \gtrsim \tau_{\mathrm{NL}}$ and, therefore, that a sustained turbulent state requires an amplification time comparable to the nonlinear decorrelation time.

We can summarise the linear behaviour described above as follows. Flow shear sweeps perturbations in time from regions of $k_x$ space where modes are unstable to where they are damped. This sweeping through unstable regions leads to the transient growth of the perturbations. The turbulent state is sustained through transient amplification of sufficient strength and duration. We showed that the changes in $N_\gamma$ and $t_0$ are

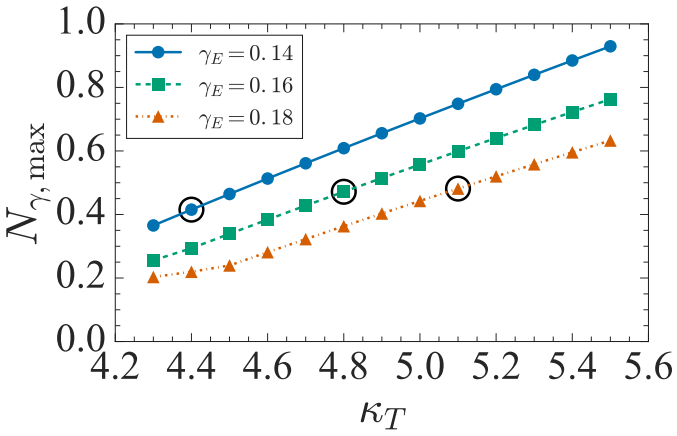



Figure 4.9: Maximum transient-amplification factor $N_{\gamma,\max}$ versus $\kappa_T$ for three values of $\gamma_E$ within the range of experimental uncertainty. The simulations circled in black represent the critical values of $\kappa_T$ above which turbulence can be sustained, suggesting the onset to turbulence occurs at $N_{\gamma,\max} \sim 0.4$.

relatively smooth as the turbulence threshold is surpassed (determined from our simulations in Section 4.2), suggesting nonlinear simulations are essential in predicting the transition to turbulence. Therefore, we will now investigate our nonlinear simulations further to determine the nature of this transition to turbulence.

## 4.4 Structure of turbulence close to and far from the threshold

*Much of this section is based on Ref. [108].*

Having established the subcritical nature of the system, we want to investigate the consequences for the structure of turbulence. We will argue that a subcritical system such as ours supports the formation of coherent structures close to the turbulence threshold, that the heat flux is proportional to the product of number of structures and their maximum amplitude, and that the properties of the turbulence are characterised by the "distance from threshold" (as opposed to the specific values of the stability parameters $\kappa_T$ and $\gamma_E$), as measured, for example, by the turbulent ion heat flux.

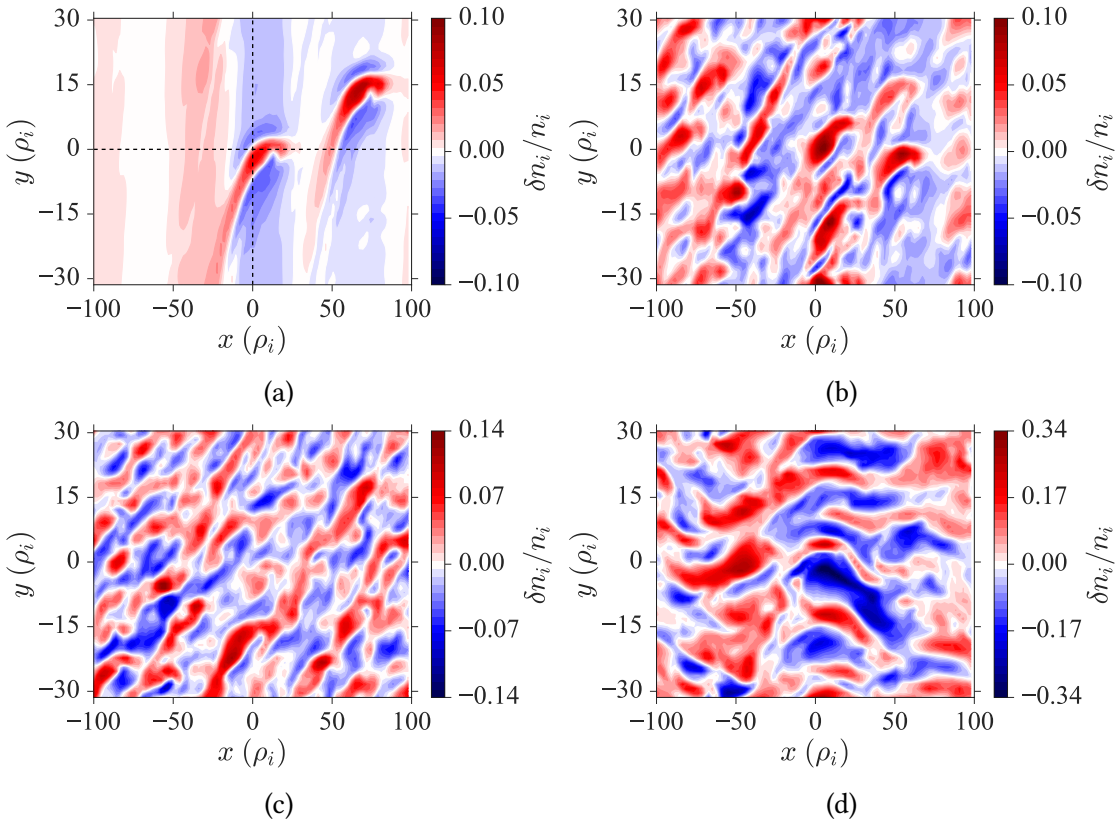



Figure 4.10: Density-fluctuation field $\delta n_i/n_i$ at the outboard midplane of MAST as a function of the local GS2 coordinates $x$ and $y$, for four combinations of stability parameters. (a) Near-threshold turbulence, $(\kappa_T, \gamma_E) = (4.8, 0.16)$. The dashed lines indicate the planes of constant $x$ and $y$ used to demonstrate the parallel structure in Figure 4.13. (b) Turbulence intermediate between the near-threshold and strongly driven cases, $(\kappa_T, \gamma_E) = (4.9, 0.16)$. (c) Strongly driven turbulence, $(\kappa_T, \gamma_E) = (5.2, 0.16)$. (d) Turbulence without flow shear, $(\kappa_T, \gamma_E) = (5.2, 0)$, showing strong zonal flows.

### 4.4.1 Coherent structures in the near-marginal state

Figure 4.10 shows the density-fluctuation field $\delta n_i/n_i$ at the outboard midplane of MAST as functions of the local GS2 coordinates $x$ and $y$ (see Appendix D for how these are related to real-space $(R, Z)$ coordinates). The simulations shown in Figures (a)–(c) are marked by points in Figure 4.1 and importantly they are all well within the region of experimental uncertainty. We choose four combinations of the stability param-

eters $(\kappa_T, \gamma_E)$ as the system is taken away from the turbulence threshold: $(4.8, 0.16)$, which is close to the turbulence threshold [Figure 4.10(a)], $(4.9, 0.16)$, an intermediate case between the marginal and strongly driven turbulence [Figure 4.10(b)], $(5.2, 0.16)$, a strongly driven case further from the threshold [Figure 4.10(c)], and $(5.2, 0)$, a case without flow shear [Figure 4.10(d)], representative of the basic ITG turbulence that has been thoroughly studied in the past [23, 25, 100].

We can describe the change in the nature of the density-fluctuation field as follows. The near-threshold state [Figure 4.10(a)] is dominated by intense (compared to the background fluctuations), coherent, and long-lived structures. As $\kappa_T$ is slightly increased (in this case by only 0.1), these structures become more numerous [Figure 4.10(b)], but have roughly the same maximum amplitude: $(\delta n_i/n_i)_{\max} \sim 0.08$. The strongly driven state [Figure 4.10(c)] exhibits a more conventional chaotic turbulent state characterised by many interacting eddies with larger amplitudes. The coherent structures in the marginal case are unlike the strongly interacting eddies that characterise the strongly driven turbulent state and more likely constitute nonlinear travelling wave (soliton-like) solution to the gyrokinetic equation. We note that these simulations are representative of the regions close to and far from the turbulence threshold, i.e., in simulations near the threshold, we always find sparse but well-defined coherent structures that survive against a backdrop of weaker fluctuations. An important exception are simulations with $\gamma_E = 0$, where we do not observe such coherent structures. As the system is taken away from the threshold by increasing $\kappa_T$, or decreasing $\gamma_E$, the structures become more numerous, while maintaining roughly the same amplitude, until they fill the entire domain, interact with each other, and break up. For parameter values far from the threshold, we observe no discernible coherent structures, but rather strongly time-dependent fluctuations with amplitudes that increase with $\kappa_T$. For completeness, Figures 4.11 and 4.12 show the perturbed radial $\boldsymbol{E} \times \boldsymbol{B}$ velocity $V_{Er}$ and the perpendicular temperature-fluctuation $\delta T_{\perp i}/T_{\perp i}$ fields. We have calculated $V_{Er}$ velocity by taking the radial component of (3.17), given by (see equation (3.42) in Ref. [84])

$$V_{Er} = \frac{c}{aB_{\text{ref}}} \frac{1}{|\nabla\psi|} \left|\frac{\partial\psi}{\partial r}\right|_{r_0} \frac{\partial\varphi}{\partial y}. \tag{4.6}$$

We see that the coherent structures have both high $V_{Er}$ and $\delta T_{\perp i}/T_{\perp i}$.

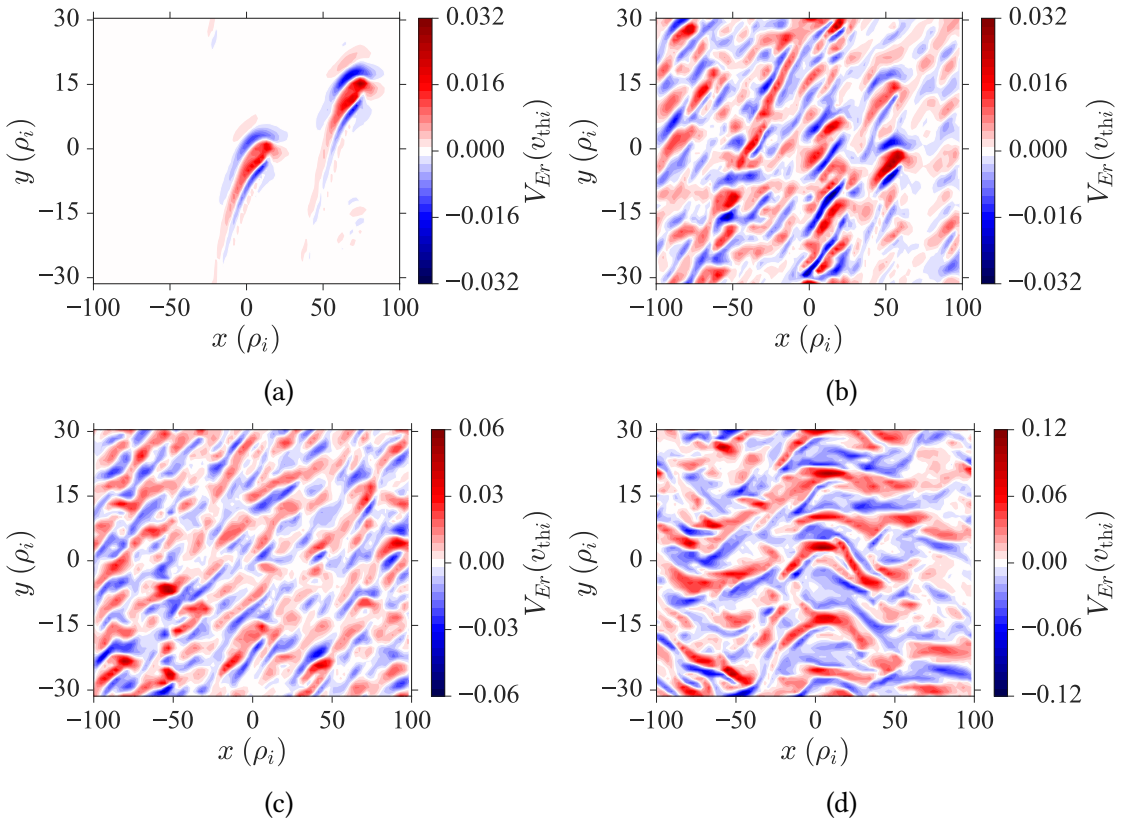



Figure 4.11: Radial $\boldsymbol{E}\times\boldsymbol{B}$ velocity $V_{Er}$ at the outboard midplane of MAST as a function of the local GS2 coordinates $x$ and $y$ for the same equilibrium parameters as in Figure 4.10.

We now consider the marginal cases, and the dynamics of the coherent structures, more carefully, starting with their parallel structure. Figure 4.13 shows two views of the coherent structures in Figure 4.10(a) in the parallel direction (which in GS2 is quantified by the poloidal angle $\theta$; see Appendix D) at constant $y$ [Figure 4.13(a)] and at constant $x$ [Figure 4.13(b)]. It is clear that the coherent structures are elongated in the parallel direction and have an amplitude much larger than the "background" fluctuations.

In time, the coherent structures are advected by the flow imposed by the flow shear in the poloidal direction, but also drift in the radial direction. Figures 4.14(a) and (b) show $\delta n_i/n_i$ for a marginal nonlinear simulation at $(\kappa_T, \gamma_E) = (5.1, 0.18)$, which has only one coherent structure, as a function of $(t, x)$ and $(t, y)$ (taking the maximum value of $\delta n_i/n_i$ in the other direction), respectively. Figure 4.14(a) shows the radial motion

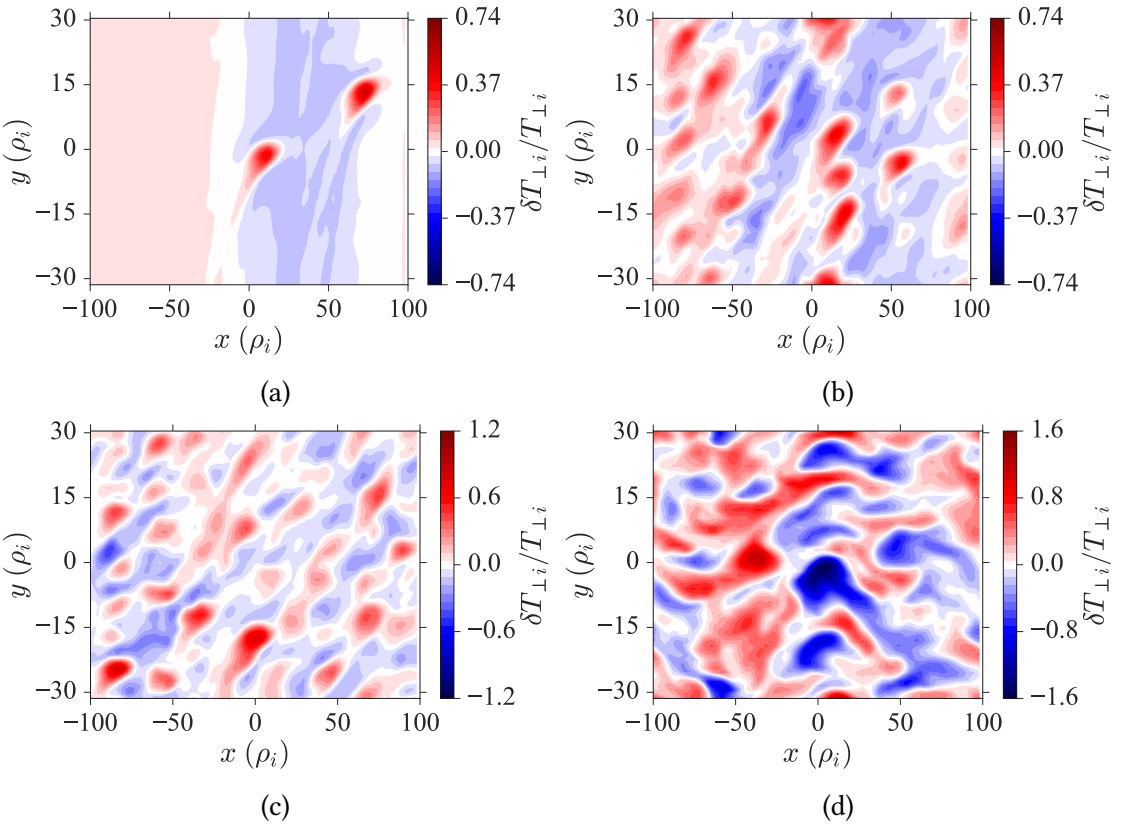
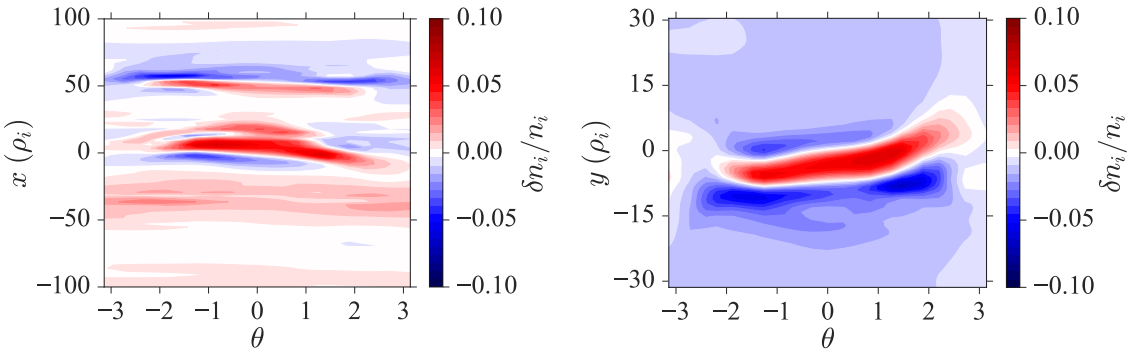



Figure 4.12: Perpendicular-temperature fluctuation field $\delta T_{\perp i}/T_{\perp i}$ outboard midplane of MAST as a function of the local GS2 coordinates $x$ and $y$ for the same equilibrium parameters as in Figure 4.10.

of the structure across the domain, which the structures crosses in a time of roughly $50\ (a/v_{\mathrm{th}i})$. The radial motion of the structures in Figure 4.14(a) has a constant velocity and fitting the trajectory with a straight line (the dashed line) gives a radial velocity of $v_x = 0.0330 \pm 0.0001\ v_{\mathrm{th}i}$. Figure 4.14(b) shows the poloidal advection of the structure with a much shorter poloidal crossing time of roughly $5\ (a/v_{\mathrm{th}i})$. The poloidal motion of the structure is entirely due to the advection caused by the flow shear as we will now explain. As we saw in Figure 4.14(a), $v_x$ is constant and the radial position is given by $x(t) = v_x t$. The poloidal advection due to the flow shear is given by $v_y(t) = \gamma_E x(t)$ and so the direction of the flow shear reverses at $x = 0$. Combining the expressions for $x(t)$ and $v_y(t)$ and integrating, we find that $y(t) \propto \gamma_E v_x t^2$, and, as shown by the




(a) (b)

Figure 4.13: (a) Density-fluctuation field $\delta n_i/n_i$ in the $x$-$z$ plane at $y = 0$. (b) Density-fluctuation field $\delta n_i/n_i$ in a $y$-$z$ plane at $x = 0$. Both plots are shown for the same simulation and at the same time as in Figure 4.10(a); the corresponding planes are indicated by the dashed lines in Figure 4.10(a). The parallel direction in GS2 is quantified by the poloidal angle $\theta$ (see Section 3.4.1).

dashed line in Figure 4.14(b), this explains the poloidal motion of the structure, which indeed reverses direction at $x = 0$. The long-lived nature of coherent structures close to the turbulence threshold is illustrated by Figure 4.14(a) given that the GS2 domain is periodic in $x$ and $y$, and so the structure exists for $t > 100\ (a/v_{\mathrm{th}i})$.

### 4.4.2 $Q_i/Q_{\mathrm{gB}}$ as an order parameter

The results in Section 4.4.1 suggested that the nature of the turbulence is set by how far the system is from the turbulence threshold. Specifically, that the near threshold state is dominated by coherent structures that seem to increase in number and amplitude as the system is taken further from the threshold. This suggests that the important metric that should be used to quantify the state of the system is the "distance from threshold" and not the specific values of $\kappa_T$ and $\gamma_E$ (although both can be used to control the distance from threshold). $Q_i/Q_{\mathrm{gB}}$ is a strong function of $\kappa_T$ and $\gamma_E$, with the dependence that we showed in Figure 4.1, and so we can use $Q_i/Q_{\mathrm{gB}}$ as a control parameter to measure the distance from the turbulence threshold. In Sections 4.4.3 and 4.4.4, we will quantify the changes in the amplitude and number of structures for our parameter

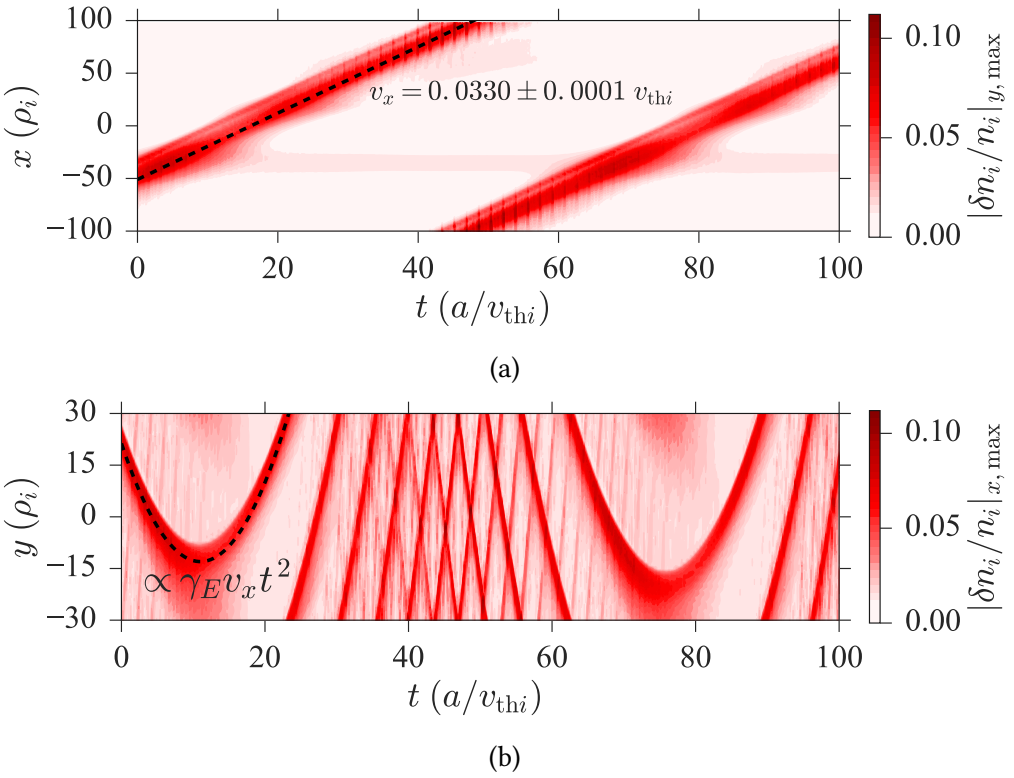



Figure 4.14: Density-fluctuation field $\delta n_i/n_i$ as a function of (a) $x$ and $t$ (taking the maximum in the $y$ direction) and (b) $y$ and $t$ (taking the maximum in the $x$ direction) for a marginally unstable case with $(\kappa_T, \gamma_E) = (5.1, 0.18)$, which contains only one coherent structure. The structure is advected both radially and poloidally. We note that the GS2 domain is periodic in $x$ and $y$ and so this is the same structure throughout the entire time period shown. The dashed line in (a) indicates $x = v_x t$, and in (b) indicates $y \propto \gamma_E v_x t^2$ showing that the poloidal advection is due to the flow imposed by the flow shear.

scan and show that the distance from threshold is the relevant order parameter.

### 4.4.3 Maximum amplitude

Considering the density-fluctuation fields shown in Figure 4.10, we see that a key property that changes as the system is taken away from the threshold is the amplitude of the eddies. We would like to know how the amplitude changes with the distance from

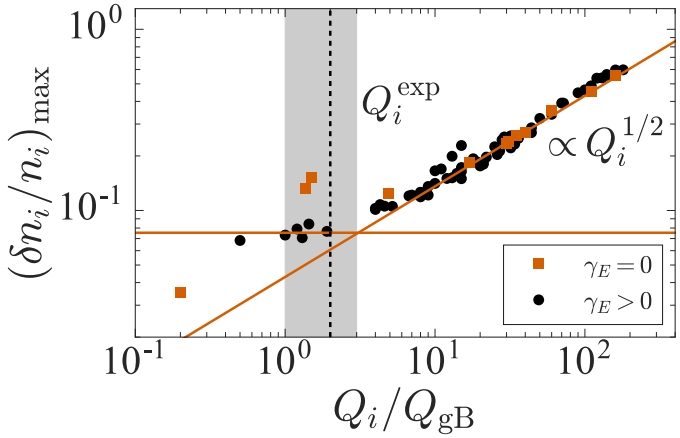



Figure 4.15: Maximum amplitude of the density fluctuations versus $Q_i/Q_{\mathrm{gB}}$. The naive scaling (4.7), $Q_i^{1/2} \propto \delta n_i/n_i$, is shown for reference and holds far from threshold, whereas for small values of $Q_i/Q_{\mathrm{gB}}$ (around and below the experimental value $Q_i^{\mathrm{exp}}$), the amplitude becomes independent of $Q_i/Q_{\mathrm{gB}}$.

threshold, which we quantify using $Q_i/Q_{\mathrm{gB}}$. For marginal cases, such as Figure 4.10(a), the dominant features are structures with high densities compared to the background fluctuations. In order to measure the changes in the amplitude of these structures we want to measure the maximum amplitude, as opposed to an $(x, y)$-averaged quantity, which would be small because of the relatively small volume taken up by the coherent structures. Therefore, we consider the maximum amplitude (taken over $x$ and $y$), $(\delta n_i/n_i)_{\max}$, of density perturbations averaged over time in a given simulation. Figure 4.15 shows the relationship between $(\delta n_i/n_i)_{\max}$ and $Q_i/Q_{\mathrm{gB}}$ for all the simulations in our parameter scan. The striking feature of Figure 4.15 is that $(\delta n_i/n_i)_{\max}$ hits a finite "floor" as $Q_i/Q_{\mathrm{gB}}$ approaches and goes below its experimental value. This coincides with the appearance of the long-lived structures shown in Figure 4.10(a). For $\gamma_E = 0$ simulations with values of $Q_i/Q_{\mathrm{gB}}$ below $Q_i^{\mathrm{exp}}$, we do not see a clear trend, and importantly do not see the flattening we see for $\gamma_E > 0$ simulations, suggesting that the turbulence is fundamentally different close to the turbulence threshold (as was also suggested by the absence of coherent structures).

Far from the turbulence threshold, we can estimate the expected behaviour of $\delta n_i/n_i$

via a naive estimate of the dependence of $Q_i/Q_{\mathrm{gB}}$ on $\delta n_i/n_i$ using (3.24):

$$\frac{Q_i}{Q_{\mathrm{gB}}} \sim \frac{a^2}{\rho_i^2}\frac{\delta n_i}{n_i}\frac{V_{Er}}{v_{\mathrm{th}i}} \sim k_y\rho_i\frac{T_e}{T_i}\left(\frac{a}{\rho_i}\frac{\delta n_i}{n_i}\right)^2, \tag{4.7}$$

where $(a/\rho_i)\delta n_i/n_i$ is an order-unity quantity in gyrokinetic theory [49]. In deriving (4.7), we have used (4.6) and assumed that fluctuations of $\varphi$ are related (by order of magnitude) to the electron (and, therefore, ion) density via the Boltzmann response $e\varphi/T_e \sim \delta n_e/n_e$. The scaling $\delta n_i/n_i \propto Q_i^{1/2}$ (obtained from (4.7) given that the prefactor is order unity) is indicated by the red line in Figure 4.15, and shows that this describes the scaling far from threshold well. We also see that $\gamma_E = 0$ and $\gamma_E > 0$ simulations are similar far from the threshold.

The above observations are entirely non-trivial. In the case of supercritical turbulence, we typically observe smaller fluctuation amplitudes all the way to the turbulence threshold – there is no minimum amplitude required to sustain turbulence. In contrast, Figure 4.15 shows that for the subcritical we are investigating, the maximum fluctuation amplitude remains constant, for low heat fluxes, while the heat flux decreases because there is a critical value required in order to sustain a saturated nonlinear state. The system reconciles the requirement of finite amplitude structures while allowing the heat flux to decrease via a reduction of the volume taken up by structures. This nonlinear state has not been previously observed in fusion plasmas. We further study the changes in the state of the system by performing a structure-counting analysis in the next section, explicitly showing the reduction in the volume taken up by the structures.

### 4.4.4 Structure counting

We demonstrate the change in volume taken up by finite-amplitude structures by measuring the typical number of these structures in our simulations as a function of the distance from threshold. While two-dimensional structures are easily discerned by the human eye (e.g., in the near-marginal case shown in Figure 4.10(a), there are two), counting them systematically is a non-trivial problem often encountered in computer vision and pattern recognition applications. Detection of coherent structures has been considered before in the context of experimental measurements of turbulence [109, 110];

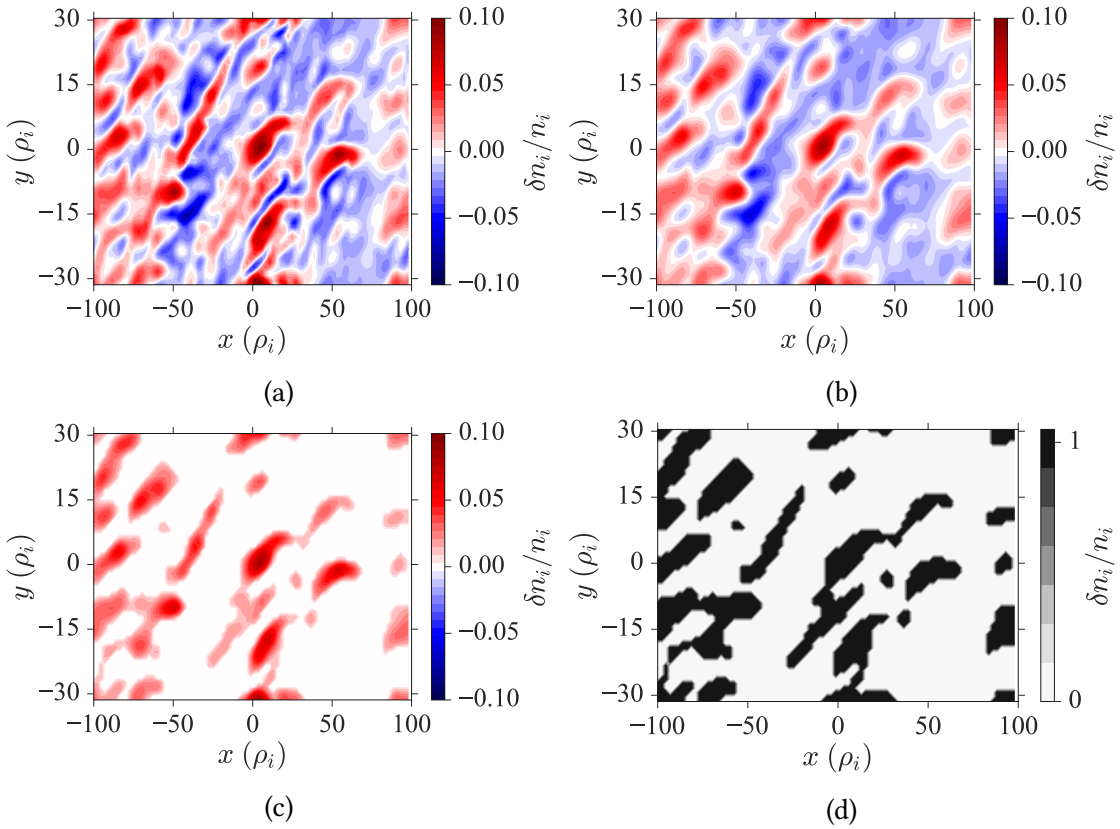



Figure 4.16: Stages of the structure counting procedure: (a) the original density-fluctuation field [as in Figure 4.10(b)]; (b) after the application of a Gaussian filter to smooth the structures; (c) after the application of a 75% threshold function; (d) after setting $\delta n_i/n_i > 0$ values to 1 for simplicity. The image-labelling algorithm is then applied to (d) and returns 19 structures for this case.

a review of various techniques is given in [111].

Structure counting can be reduced to an image-labelling, or "segmentation", problem in the following way. We applied a Gaussian image filter (with a standard deviation on the order of the grid scale) as a pre-processing step and also removed structures below 10% of the mean structure size as a post-processing step. These filtering steps are justified because we are interested in detecting intense, relatively large-scale structures, and simply applying a threshold function can lead to single points above the threshold scattered around the edges of structures that we are actually interested in counting.

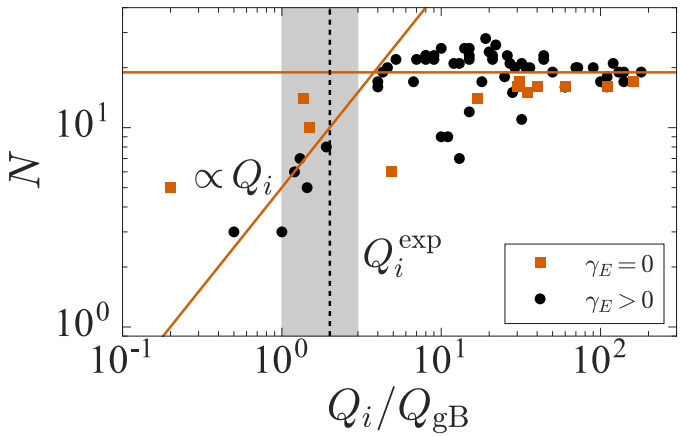



Figure 4.17: Number of structures (defined as having an amplitude above 75% of the maximum) versus $Q_i/Q_{\mathrm{gB}}$. It grows up to and slightly beyond the experimental value $Q_i^{\mathrm{exp}}$. Eventually the volume is filled with structures and their number tends to a constant. The scaling $Q_i \propto N$ is shown for reference.

We then set values below a certain percentile (here 75% of the maximum amplitude) to 0 and above it to 1. The level of the threshold function is somewhat arbitrary and the number of structures will depend on this level, but the trend as a function of our equilibrium parameters did not change as we increased or decreased the level of the threshold function. Choosing too low a level often leads to many structures being counted as only one, whereas too high a level led to only a handful of the most intense structures being counted. While this could be acceptable close to marginality, where we are interested in high-intensity structures compared to low-intensity background fluctuations, this would significantly underpredict the number of structures far from the threshold. We chose 75% as a reasonable compromise. After applying a threshold function, one is left with an array of 1's representing our structures against a background of 0's. To count these structures, we employed a general-purpose image processing package *scikit-image* [112], which implements an efficient labelling algorithm [113], then used by us to label connected regions. The structure-counting procedure is shown in Figure 4.16 where the image-labelling algorithm labelled 19 structures.

Figure 4.17 shows the results of the above analysis: the number of structures $N$ with amplitudes above the $75^{\mathrm{th}}$ percentile versus the ion heat flux $Q_i/Q_{\mathrm{gB}}$. As in Figure 4.15,

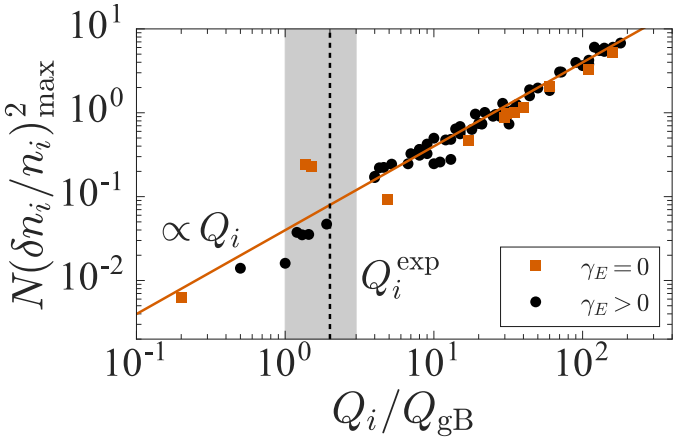



Figure 4.18: Confirmation of the scaling (4.8), where the red line indicates a line $\propto Q_i$. We note that simulations near marginality are relatively difficult to saturate leading to the low number of simulations around $Q_i^{\exp}$. However, the trend is still clear even for those simulations.

there are two distinct regimes: $N$ grows with $Q_i/Q_{\mathrm{gB}}$ until the structures have filled the simulation domain (which happens just beyond the experimental value of the flux), whereupon $N$ tends to a constant. Again, we see that the $\gamma_E = 0$ and the $\gamma_E > 0$ simulations are similar far from the threshold. Taking Figures 4.15 and 4.17 in combination, we have, roughly,

$$\frac{Q_i}{Q_{\mathrm{gB}}} \sim N\left(\frac{\delta n_i}{n_i}\right)^2_{\max}, \tag{4.8}$$

i.e., near the threshold, the turbulent heat flux increases because coherent structures become more numerous (but not more intense), whereas far from the threshold, it does so because the fluctuation amplitude increases (at a roughly constant number of structures). This relationship is confirmed by Figure 4.18, which shows $N(\delta n_i/n_i)^2_{\max}$ as a function of $Q_i/Q_{\mathrm{gB}}$, and we see that these quantities are, indeed, proportional to each other.

Thus, we have identified two types of nonlinear states depending on the distance from threshold: one dominated by coherent structures close to the threshold, and one characterised by many interacting eddies far from the threshold. We clearly showed that, far from the turbulence threshold, cases with $\gamma_E = 0$ (conventional ITG-driven

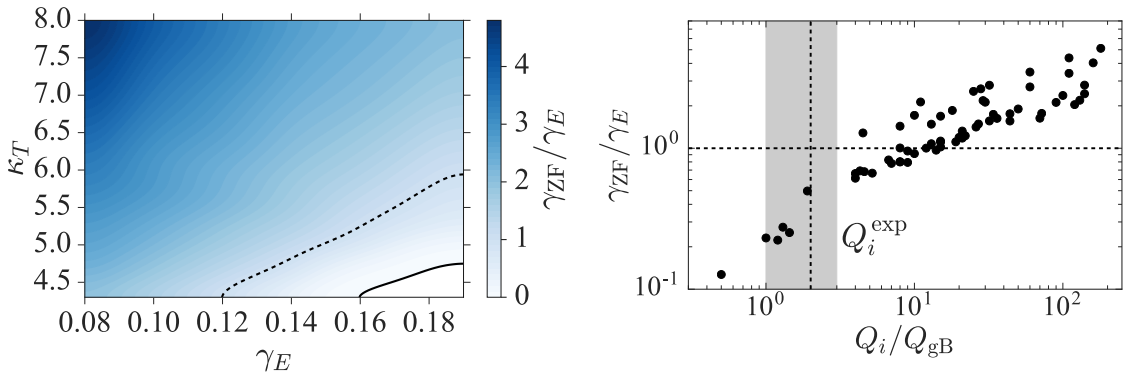
turbulence) have similar properties to $\gamma_E > 0$ cases. In the next section we investigate the role of zonal flows in regulating turbulence and come to the same conclusions as above: the presence of flow shear is important close to the threshold, but turbulence is similar for $\gamma_E = 0$ and $\gamma_E > 0$ cases far from the threshold.

### 4.4.5 Shear due to zonal flows

The dominant saturation mechanism for ITG-driven turbulence is thought to be the stabilisation caused by zonal modes [31, 99, 100, 114, 115]. Zonal modes are fluctuations in the system with $k_y = 0$ and $k_x > 0$, i.e., they have finite radial extent, but are poloidally symmetric. They are generated by nonlinear interactions in the system and contain sheared flows that can regulate turbulence. Previous work [99] on the transition to turbulence showed that near the turbulence threshold (approached by varying the equilibrium parameter $\kappa_T$), turbulence is regulated by strong zonal flows, which can cause an upshift in the critical $\kappa_T$ required for a saturated turbulent state. However, in the system under investigation, the marginal cases seem to be dominated by the background flow shear [see Figure 4.14(b)], which also has a suppressing effect on the turbulence. Thus, in this section, we investigate the role played by zonal flows in the turbulence regimes identified in Sections 4.4.1–4.4.4 and show that zonal flows do not play an important role in the near-marginal cases but become more important far from the threshold, where their effect is comparable to, and eventually dominate over that of the background flow shear.

In the MAST plasma we are investigating, there are two sources of shear that may regulate turbulence: shear due to strong toroidal rotation as a result of the injection of neutral particles by the NBI heating system, and shear due to zonal flows which are generated by nonlinear interactions. We have already seen that shear due to the toroidal rotation is controlled by the equilibrium parameter $\gamma_E$, which we vary in this study. The shear due to the zonal flows $V'_{\mathrm{ZF}}$ is calculated from (4.6) by considering only the poloidally symmetric component, and is given by

$$V'_{\mathrm{ZF}} = \frac{c}{aB_{\mathrm{ref}}} \frac{q_0}{r_0} \frac{1}{|\nabla\alpha|} \frac{\partial^2 \varphi_{\mathrm{ZF}}}{\partial x^2}, \tag{4.9}$$




(a) (b)

Figure 4.19: (a) The ratio of zonal shear to background flow shear $\gamma_{\rm ZF}/\gamma_E$ over the same range of $\kappa_T$ and $\gamma_E$ as shown in Figure 4.1. The effects of zonal shear and flow shear are comparable when $\gamma_{\rm ZF}/\gamma_E \sim 1$. The white region in the lower right-hand corner indicates the region where there is no turbulence, i.e., $Q_i = 0$ (see Figure 4.1), and the dashed black line indicates $\gamma_{\rm ZF}/\gamma_E = 1$. (b) $\gamma_{\rm ZF}/\gamma_E$ as a function of $Q_i/Q_{\rm gB}$. The vertical dashed line indicates the value of the experimental heat flux and the horizontal dashed line indicates $\gamma_{\rm ZF}/\gamma_E = 1$.

where $V'_{\rm ZF}$ is a function only of $t$ and $x$, and $\varphi_{\rm ZF}$ is the poloidally symmetric component of $\varphi$. To determine whether the zonal shear will dominate over $\gamma_E$ we calculate the RMS value of the zonal shear, $\gamma_{\rm ZF}$:

$$\gamma_{\rm ZF} = \left\langle V'^2_{\rm ZF} \right\rangle^{1/2}_{t,x}, \tag{4.10}$$

where $\langle \cdots \rangle_{t,x}$ indicates an average over $t$ and $x$. We can now compare $\gamma_{\rm ZF}$ with $\gamma_E$ to determine the relative importance of each as a function of our equilibrium parameters.

Figure 4.19(a) shows the ratio of the zonal shear to the flow shear, $\gamma_{\rm ZF}/\gamma_E$, as a function of $\kappa_T$ and $\gamma_E$ over the same parameter range as shown in Figure 4.1. The effects of $\gamma_{\rm ZF}$ and $\gamma_E$ are comparable where $\gamma_{\rm ZF}/\gamma_E \sim 1$, which is indicated by the dashed line. We see that the regime in which $\gamma_{\rm ZF}$ and $\gamma_E$ become comparable occurs some distance away from the turbulence threshold. Therefore, close to the threshold (small $\gamma_{\rm ZF}/\gamma_E$), we expect the shear due to the background flow do dominate, while far from the threshold (large $\gamma_{\rm ZF}/\gamma_E$), we expect the shear due to the zonal flows to dominate.

Similar to our findings in Section 4.4.4, Figure 4.19(a) suggests that the change in $\gamma_{\rm ZF}/\gamma_E$ is effectively a function of the distance from the turbulence threshold because

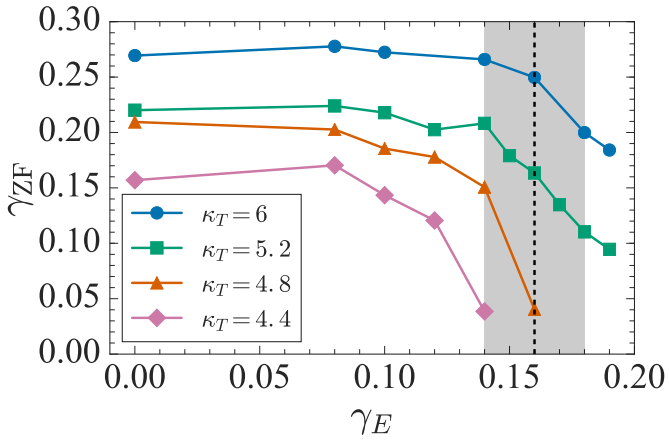



Figure 4.20: Zonal shear $\gamma_{\mathrm{ZF}}$ as a function of background flow shear $\gamma_E$ showing that zonal flow regulation of turbulence is comparable between low $\gamma_E$ (high $Q_i/Q_{\mathrm{gB}}$) cases and $\gamma_E = 0$ cases.

(after comparing to Figure 4.1) we see that regions of similar heat flux have similar values of $\gamma_{\mathrm{ZF}}/\gamma_E$. Figure 4.19(b) shows this dependence explicitly: $\gamma_{\mathrm{ZF}}/\gamma_E$ as a function of $Q_i/Q_{\mathrm{gB}}$. The vertical dashed line indicates $Q_i^{\mathrm{exp}}/Q_{\mathrm{gB}}$ and we see that $\gamma_{\mathrm{ZF}}/\gamma_E$ is small around this value. This suggests that zonal shear plays a weaker role than $\gamma_E$ in regulating experimentally relevant turbulence for this MAST configuration. Therefore, near-threshold and far-from-threshold turbulence are distinguished by the fact that $\gamma_E$ is important close to the threshold, whereas the $\gamma_{\mathrm{ZF}}$ dominates far from the turbulence threshold. Far from the threshold the turbulence is likely similar to conventional ITG-driven turbulence in the absence of background flow shear. This is demonstrated in Figure 4.20 which shows $\gamma_{\mathrm{ZF}}$ as a function of $\gamma_E$. We see that for low $\gamma_E$ and/or high $\kappa_T$ (i.e., cases far from the threshold), $\gamma_{\mathrm{ZF}}$ is comparable to cases where $\gamma_E = 0$ and so zonal flows are the likely mechanism for regulating turbulence in these simulations.

## 4.5 Summary

In this chapter we performed a parameter scan in $\kappa_T$ and $\gamma_E$ and showed that the experimental ion heat flux is consistent with equilibrium parameters $(\kappa_T, \gamma_E)$ close to the turbulence threshold. We demonstrated that in the presence of a background flow

shear, the system is subcritical: above a certain critical value of $\kappa_T$, and below a critical value of $\gamma_E$, a large initial perturbation is required to ignite turbulence. We studied the real-space structure of turbulence and found novel features of the transition to a turbulent state in an experimentally relevant fusion plasma when the system is subcritical. For equilibrium parameters near the threshold, the density and temperature fluctuations (and hence heat flux) are concentrated in long-lived, intense coherent structures. We demonstrated that flow shear (as opposed to zonal shear) is important at these experimentally relevant parameters. As the equilibrium parameters $(\kappa_T, \gamma_E)$ depart slightly from their critical values into the more strongly driven regime, the number of these structures increases rapidly while their amplitude stays roughly constant (in contrast to the conventional supercritical turbulence, where the amplitude increases with $\kappa_T$ because arbitrarily low-amplitude turbulence can be supported). Increasing $\kappa_T$ or decreasing $\gamma_E$ further leads to the structures filling the simulation domain and any further increase in the heat flux is caused by an increase in fluctuation amplitude. The latter regime is similar to the conventional plasma turbulence where zonal flows are the dominant mechanism for regulating turbulence.

# Chapter 5

# *Correlation analysis and comparison with experimental results*

## 5.1 Introduction

In Chapter 4, we discussed the results of our nonlinear simulations in terms of the observed transport and identified the conditions needed to sustain a turbulent state. In this chapter, we would like to make more quantitative comparisons with direct experimental measurements of the turbulent fluctuations. We are interested in doing such comparisons with experimental measurements in order to gain confidence in the predictions made by our simulations. Only once the numerical predictions have been extensively checked against existing experimental data in a range of different devices, can we attempt to make predictions of turbulence in future devices. This study is focused on MAST, but forms an important part of the wider effort of validating numerical models against experimental data. More broadly, we are interested in understanding the nature of turbulence itself and how it behaves in tokamaks as equilibrium quantities are varied, such as the flow shear and ITG as we do in this study. Ultimately, we want to find equilibrium configurations that maximise the fusion power and, by necessity, minimise the turbulence. However, in order to do this, we need to understand the key drivers of turbulence and how the turbulence responds to changes in equilibrium parameters. It has only recently become possible to extend the study of turbulence from the transport

of particles, momentum and heat, to the physical structure by measuring, for example, the density fluctuations. Beam emission spectrometry is one such technique and it is with measurements from this diagnostic that we compare our simulation predictions in this work.

The BES diagnostic on MAST infers density fluctuations on a poloidal $(R, Z)$-plane from $D_\alpha$ emission by excited neutral particles injected by the NBI heating system. Correlation-analysis techniques were developed [69] to measure the radial correlation length, $l_R$, the poloidal correlation length, $l_Z$, and the correlation time, $\tau_c$, of these measured density fluctuations. The results of such a correlation analysis for the MAST discharges that we consider in this work were reported in Ref. [65]. Also reported in Ref. [65] were the first comparisons of BES measurements with global, nonlinear particle-in-cell simulations using the NEMORB code [116], which found the following. The simulations explicitly showed that kinetic electrons, flow shear, and collisions between plasma particles played an important role in predicting the turbulence found in MAST – effects that we have included. In the outer-core region, which we consider in this work, global simulations with the physics effects listed above did not predict a turbulent state, possibly due to the boundary conditions, forcing fluctuations to be zero at the plasma boundary. However, at inner radii there was some agreement between simulations and experiment with respect to the heat flux, density fluctuation levels, and perpendicular correlation lengths. The correlation time, on the other hand, was found to be on average two orders of magnitude larger in the simulations compared to the experimental measurements over the whole radius. The inability of global gyrokinetic simulations to predict turbulence in a region where the BES diagnostic clearly finds the plasma to be turbulent as well as the significant overprediction of the correlation time may suggest that the resolution requirements for simulations of MAST plasmas are higher than those currently allowed by global simulations.

In this work, we have used local gyrokinetic simulations because they offer two desirable features compared to global gyrokinetic simulations: they only attempt to simulate plasma turbulence at a single radius and as a result allow increased resolution for resolving the turbulence, and they avoid the complications of having to speculate on the boundary conditions in the inner core and at the plasma edge. It is the goal of this study

to evaluate the merits of local gyrokinetic simulations in predicting the turbulence in MAST, both in terms of averaged quantities such as transport and in quantitative comparisons of the statistics of turbulent fluctuations.

In this chapter, we will make such quantitative comparisons between the fluctuations predicted by our simulations and those measured by the BES diagnostic. Before being able to make comparisons between our simulations and experimental measurements we converted our density fluctuation data from flux-tube geometry to a poloidal plane, further explained in Appendix D. We review the correlation-analysis techniques (Section 5.2) and experimental results (Section 5.3) in Ref. [65] and then present two types of correlation analysis of our nonlinear simulations. The first will be of GS2 density fluctuations with a "synthetic BES diagnostic" applied to simulate what would be measured by a real BES diagnostic (Section 5.4). We will consider the results from nonlinear simulations with values of $(\kappa_T, \gamma_E)$ within the experimental-uncertainty range and compare them with the experimental results. The second analysis will be of the raw GS2 density fluctuations as a function of $Q_i/Q_{\mathrm{gB}}$, done for our entire parameter scan (Section 5.5), emphasising the extent to which it is the distance from the threshold rather than individual values of $\kappa_T$ or $\gamma_E$ that determine the statistical characteristics of the density fluctuations.

## 5.2 Correlation analysis

We start by giving an overview of the correlation-analysis techniques used in Refs. [65, 69]. We will also present an alternative measurement of the poloidal correlation length $l_Z$, taking advantage of the increased resolution available in the poloidal direction from our simulations. While there is no experimental estimate of the parallel correlation length $l_\parallel$ available from the BES data, we are able to use the three-dimensional data available from GS2 to extend the correlation analysis to the parallel direction.

The two-point spatio-temporal correlation function is, by definition,

$$C(\Delta R, \Delta Z, \Delta\lambda, \Delta t) = \frac{\langle \delta n_i/n_i(R, Z, \lambda, t)\delta n_i/n_i(R+\Delta R, Z+\Delta Z, \lambda+\Delta\lambda, t+\Delta t)\rangle}{\left[\langle \delta n_i^2/n_i^2(R, Z, \lambda, t)\rangle \langle \delta n_i^2/n_i^2(R+\Delta R, Z+\Delta Z, \lambda+\Delta\lambda, t+\Delta t)\rangle\right]^{1/2}}, \quad (5.1)$$

where $\delta n_i/n_i$ is the density-fluctuation field calculated by GS2 (which has a mean of zero) and $\Delta R$, $\Delta Z$, $\Delta\lambda$ are the radial, poloidal, and parallel separations, respectively between the two reference points, $\Delta t$ is the time lag, and $\langle \ldots \rangle$ is an ensemble average, that is, an average over all possible pairs of points that have the appropriate separation and time lag. Note that the ensemble averages in the plane perpendicular to the magnetic field are calculated at $\theta = 0$, i.e., they are not averaged over $\theta$. Note also that we divide our data in the time domain into window of $\sim 100$–$400$ $\mu$s, and the calculated separate ensemble averages in each time window. This allows us to estimate the variance of the correlation parameters we calculate.

However, instead of calculating the full correlation function (5.1), we will estimate individual correlation lengths and times (which we will define below) by performing a one-dimensional correlation analyses separately in each direction. All of the representative correlation functions that are plotted in the sections that follow will be for the equilibrium parameters $(\kappa_T, \gamma_E) = (5.1, 0.16)$ over a real-space domain of $20 \times 20$ cm$^2$ (see Appendix D).

### 5.2.1 Radial correlation length

The radial correlation length $l_R$ is estimated by fitting the correlation function $C(\Delta R, \Delta Z = 0, \lambda(\theta = 0), \Delta t = 0)$ with a Gaussian function:

$$f_R(\Delta R) = \exp\left[-\left(\frac{\Delta R}{l_R}\right)^2\right]. \quad (5.2)$$

Following experimental observations in, this fitting function is adopted on the assumption that fluctuations have no wave-like structure in the radial direction [65, 69]. Unlike in the fitting functions used for experimental data, no parameters are necessary here to account for global offsets, usually due to large-scale, global MHD modes, which do not

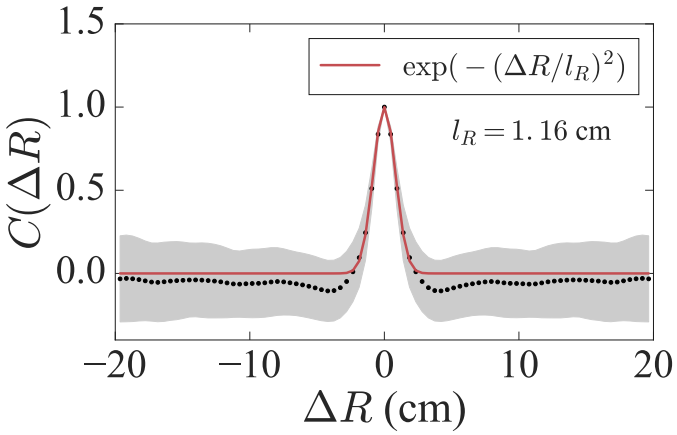


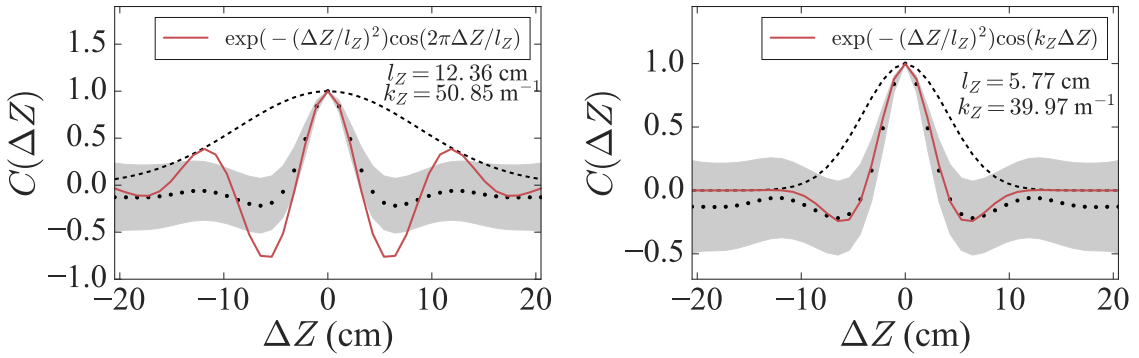

Figure 5.1: A representative radial correlation function fitted with the function (5.2) (red line). The points show the correlation function $C(\Delta R)$ averaged over $t$ and $Z$ and the shaded region shows the associated standard deviation.

appear in our simulations, where the mean density fluctuation over the whole domain is zero. A representative example of the fitting procedure for the radial correlation function is shown in Figure 5.1. The points show the measured correlation function and the red line the fit (5.2). We took an average over $t$ and $Z$ and assumed that radial correlations do not change with $t$ and $Z$ (i.e., that the system is statistically homogeneous in time and in the poloidal direction). The shaded region indicates the standard deviation calculated over the integrals of $t$ and $Z$ used in this averaging. We expect that $C(\Delta R) \to 0$ as $\Delta R$ increases (and similarly for subsequent correlation functions in the other directions) because the fluctuations have a mean of zero over the computational domain.

### 5.2.2 Poloidal correlation length

The poloidal correlation length is calculated by assuming wave-like fluctuations in the poloidal direction and fitting $C(\Delta R = 0, \Delta Z, \lambda(\theta = 0), \Delta t = 0)$ with an oscillating Gaussian function of the form

$$f_Z(\Delta Z) = \cos\left(2\pi k_Z \Delta Z\right) \exp\left[-\left(\frac{\Delta Z}{l_Z}\right)^2\right], \tag{5.3}$$




(a) (b)

Figure 5.2: Representative poloidal correlation function fitted with the function (5.3) (red line) keeping the poloidal wavenumber $k_Z$ (a) fixed to $k_Z = 2\pi/l_Z$, (b) as a free fitting parameter. The points in each plot show the correlation function $C(\Delta Z)$ averaged over $t$ and $R$ and the shaded regions show the associated standard deviation. The dashed lines indicate the Gaussian envelope $\exp(-(\Delta Z/l_Z))$

where $k_Z$ is the poloidal wavenumber. References [65, 69] found that with only four poloidal channels, the BES diagnostic could not fix $l_Z$ and $k_Z$ separately in a meaningful way. As a result, when fitting experimental data, the wavenumber is fixed to the value $k_Z = 2\pi/l_Z$. In our GS2 simulations, we can have many more points in the poloidal direction, allowing us to compare fits with $k_Z$ both as a free fitting parameter and fixed in the way described above. Figure 5.2 shows a representative poloidal correlation function from our simulations along with a fitted function (5.3), both with fixed $k_Z = 2\pi/l_Z$ [Figure 5.2(a)] and free $k_Z$ [Figure 5.2(b)]. The red lines in each plot indicate the fit (5.3) and the dashed lines indicate the Gaussian envelope $\exp(-(\Delta Z/l_Z))$. We have taken an average over the variables $t$ and $R$. We see that the fit with $k_Z$ as a free parameter approximates the correlation function better and predicts a shorter $l_Z$. For consistency with previous work, we will show the correlation results for both cases in Section 5.5.

### 5.2.3 Correlation time

In the presence of toroidal rotation, turbulent structures are advected in the poloidal direction with an apparent velocity $v_Z$ given by [64]

$$v_Z = R\omega_0 \tan\vartheta, \tag{5.4}$$

where $\vartheta$ is the magnetic-field pitch-angle (see Appendix D). Following Ref. [64], we can use this to calculate the correlation time $\tau_c$ by tracking turbulent structures as they move poloidally and measuring their temporal decorrelation. This method assumes that the temporal decorrelation dominates over any effects due to the finite parallel correlation length, as we will now explain. While turbulent structures are elongated along the field lines, they rotate rapidly in the toroidal direction. Measurements taken at a single point (or a poloidal plane) will measure the correlation time as a combination of two effects: (i) true decorrelation of turbulent structures in time, and (ii) structures of finite parallel length moving past the measurement point. Both of these two effects will appear as structures decorrelating in time but are indistinguishable in stationary measurements of turbulence. In order for the true decorrelation of structures (the quantity we are interested in) to dominate over the movement of structures past the detector we require that [69]

$$\tau_c \ll l_\parallel \cos\vartheta / R\omega_0. \tag{5.5}$$

In Section 5.5.1, we will confirm that this condition is indeed satisfied.

The correlation time $\tau_c$ is calculated using the so-called "cross-correlation time delay" technique [64, 66, 68]. Following this method, we calculate the correlation function $C_{\Delta Z}(\Delta t) = C(\Delta R = 0, \Delta Z, \lambda(\theta = 0), \Delta t)$ for several poloidal separations $\Delta Z$, including $\Delta Z = 0$, as shown in Figure 5.3. As the structures are advected poloidally, they decorrelate and the peak of the correlation function at a given $\Delta Z$, i.e., the value of $C_{\Delta Z}(\Delta t)$, decreases for increasing $\Delta Z$. The correlation time $\tau_c$ is then defined as the characteristic exponential decay time of the peaks of the correlation functions. Namely, we fit $C_{\Delta Z}(\Delta t = \Delta t_{\text{peak}})$ with the function

$$f_\tau(\Delta Z) = \exp\left[-\left|\frac{\Delta t_{\text{peak}}(\Delta Z)}{\tau_c}\right|\right], \tag{5.6}$$

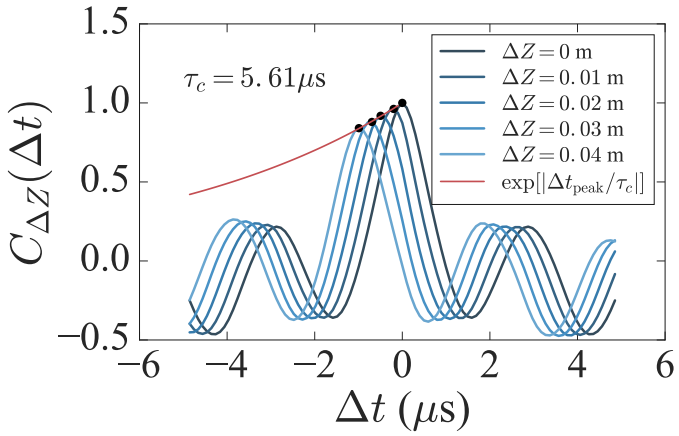



Figure 5.3: Time correlation functions $C_{\Delta Z}(\Delta t)$ for several poloidal separations $\Delta Z$. The points indicate the maximum value of $C(\Delta t)$ for a given $\Delta Z$, and the red line indicates the function (5.6) fitted to those points.

as shown for a representative correlation function in Figure 5.3, where the blue lines show correlation functions $C_{\Delta Z}(\Delta t)$ for different poloidal separations and the red line shows the fit (5.6).

### 5.2.4 Parallel correlation length

Since GS2 simulations supply the full 3D density-fluctuation field (unlike BES measurements), we are able to study the parallel structure of the turbulence. To do this, we convert the fluctuation field from the GS2 parallel coordinate $\theta$ to a real-space coordinate $\lambda(\theta)$ along the field line, as discussed in Appendix D. We then calculate the correlation function $C(\Delta R = 0, \Delta Z = 0, \Delta\lambda, \Delta t = 0)$ and take an average over $(R, Z, t)$. We fit the correlation function with an oscillating Gaussian function of the form

$$f_{\parallel}(\Delta\lambda) = \cos\left(2\pi k_{\parallel}\Delta\lambda\right)\exp\left[-\left(\frac{\Delta\lambda}{l_{\parallel}}\right)^2\right], \tag{5.7}$$

where $k_{\parallel}$ is the parallel wavenumber. A representative example of the fitting procedure for the radial correlation function is shown in Figure 5.4, where the red line indicates the fit (5.7) and the dashed line shows the Gaussian envelope $\exp\left(-(\Delta\lambda/k_{\parallel})\right)$.

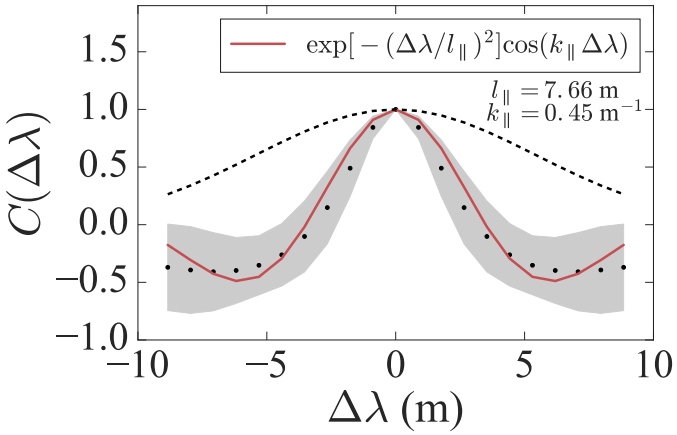



Figure 5.4: Representative parallel correlation function fitted with the oscillating Gaussian function (5.7) (red line). The points show the correlation function $C(\Delta\lambda)$ averaged over $(t, R, Z)$ and the shaded region shows the associated standard deviation. The dashed line shows the Gaussian envelope $\exp\big(-(\Delta\lambda/k_\parallel)\big)$.

### 5.2.5 Density-fluctuation amplitude

The final simulation prediction we can compare with the experimental results in Ref. [65], is the RMS density fluctuation at the outboard midplane averaged over the $(t, R, Z)$:

$$\left(\frac{\delta n_i}{n_i}\right)_{\text{rms}} = \left\langle \frac{\delta n_i^2(t,R,Z)}{n_i^2} \right\rangle_{t,R,Z}^{1/2}. \tag{5.8}$$

## 5.3 Experimental BES results

Before applying the correlation analysis to our simulations, we review the experimental results from MAST discharge #27274, with which we will be comparing, first presented in [65]. As discussed in Section 2.2, MAST discharge #27274 forms part of a set of three discharges, which measured correlation properties over the whole outer radius. Figure 5.5 shows the experimental results obtained for the radial correlation length $l_R^{\text{EXP}}$, the poloidal correlation length $l_Z^{\text{EXP}}$, the correlation time $\tau_c^{\text{EXP}}$, and the RMS density fluctuations $(\delta n_i/n_i)_{\text{rms}}^{\text{EXP}}$ as functions of $r = D/2a$. The vertical dashed line in each plot indicates the radius at which we performed our simulations and the corresponding

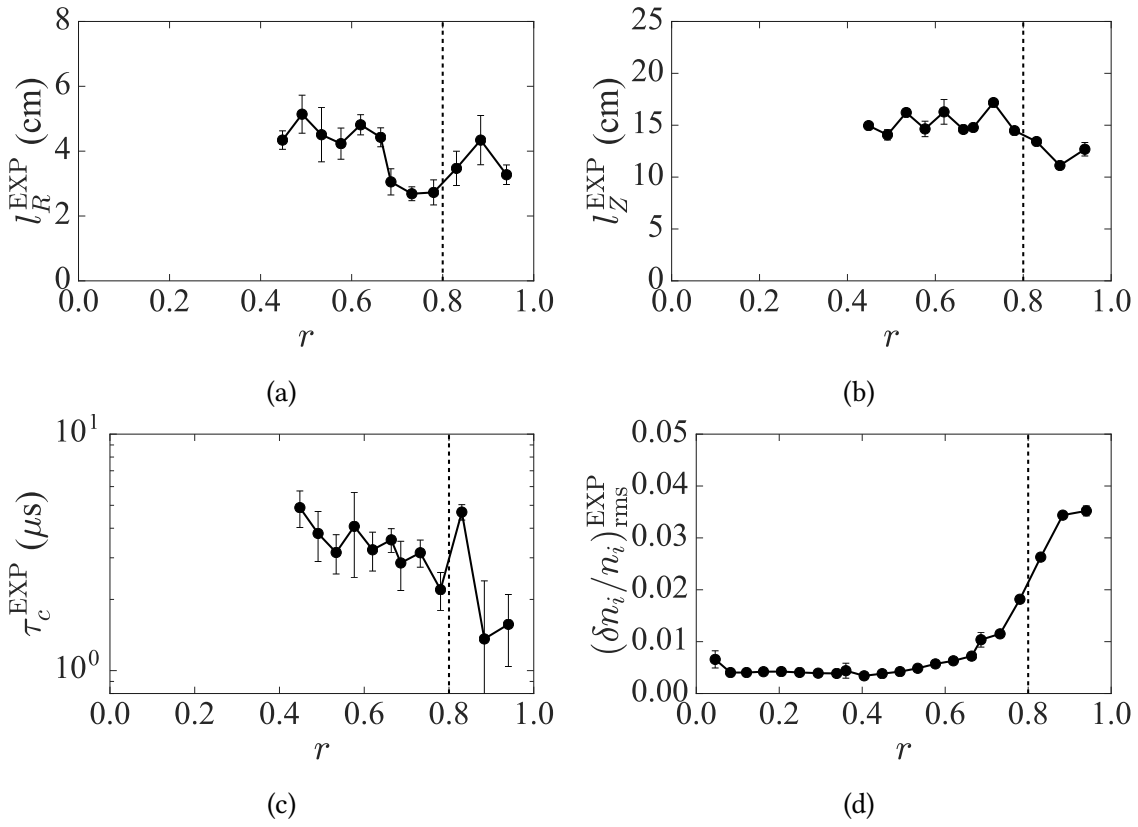



Figure 5.5: Results of the correlation analysis of BES data from MAST discharges #27272, #27268, and #27274 combined to give correlation properties of the turbulence as functions of $r = D/2a$. These results are the same as those previously presented in [65]. The values of the correlation parameters were not available at $r \lesssim 0.4$, because turbulence was suppressed in this region. The vertical dashed line indicates the radius corresponding to the local equilibrium configurations for which we performed our simulations.

values with which we will compare. From these results, we find the following (after interpolating between the experimental data points):

$$\begin{aligned} l_R^{\mathrm{EXP}} &= 3 \pm 0.4 \text{ cm}, \\ l_Z^{\mathrm{EXP}} &= 14.06 \pm 0.09 \text{ cm}, \\ \tau_c^{\mathrm{EXP}} &= 3.2 \pm 0.4 \ \mu\text{s}, \\ \left(\frac{\delta n_i}{n_i}\right)_{\mathrm{rms}}^{\mathrm{EXP}} &= 0.0214 \pm 0.0006. \end{aligned} \tag{5.9}$$

We will be comparing the correlation parameters calculated from our simulations in the following sections to those in (5.9).

## 5.4 Correlation analysis with synthetic diagnostic

In order to compare our simulations with the BES measurements, a number of data transformations were necessary. We mapped our density fluctuations "measured" in the outboard midplane (at $\theta = 0$) from GS2 $(x, y)$ coordinates onto a poloidal $(R, Z)$-plane as explained in Appendix D. We also transformed from the rotating plasma frame, the frame in which our simulations were performed, to the laboratory frame, as also explained in Appendix D. We then applied a synthetic diagnostic to our density fluctuations, including the point-spread functions (described in Section 2.3) to model instrumentation effects and atomic physics, to add artificial noise similar to that found in the experiment, and to map the density-fluctuation field onto an $8 \times 4$ grid similar to the arrangement of BES channels. An important feature of the analysis of experimental data is the presence of a filter to remove high-energy radiation present in the experiment. We have included this filter for consistency in the analysis of synthetic data produced applying the synthetic diagnostic to our simulation data. The results without this filter are presented and discussed in Appendix E.

Figure 5.6 shows the radial correlation length $l_R^{\mathrm{SYNTH}}$, poloidal correlation length $l_Z^{\mathrm{SYNTH}}$, correlation time $\tau_c{}^{\mathrm{SYNTH}}$, and RMS density fluctuation $(\delta n_i/n_i)_{\mathrm{rms}}^{\mathrm{SYNTH}}$ calculated from our simulations with the synthetic diagnostic applied using the correlation analysis described in Section 5.2. These values should agree with the experimentally measured correlation parameters in (5.9) because the equilibrium parameters $\kappa_T$ and $\gamma_E$ at which the results shown in Figure 5.6 were obtained are strictly within the experimental-uncertainty range of these parameters. The dashed lines and shaded areas in Figure 5.6 indicate the experimental values and associated errors given in (5.9) . The circled points indicate the simulations that matched the experimental level of heat flux (listed in Table 4.1).

Examining Figure 5.6(a), we see that the values of $l_R^{\mathrm{SYNTH}}$ are clustered around $2$ cm and below the experimental BES measurement of $3 \pm 0.4$ cm (see Section 5.3). According

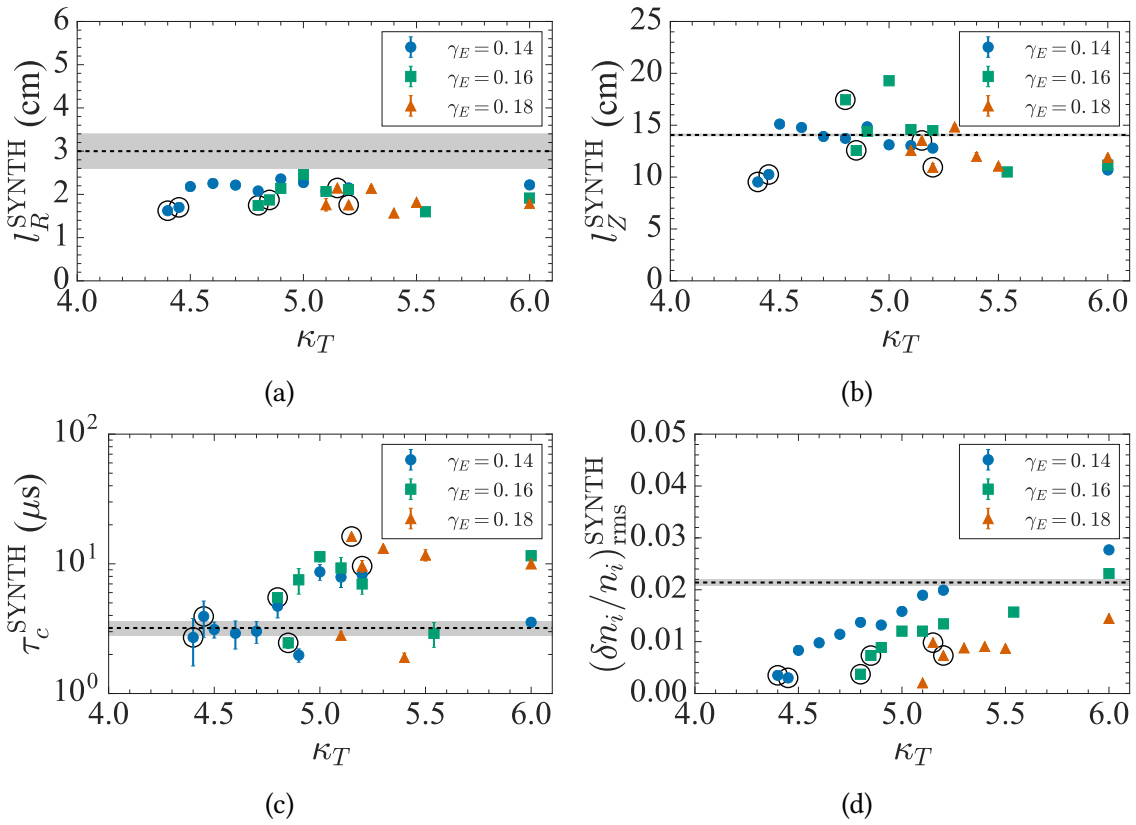



Figure 5.6: Comparison of correlation parameters obtained via synthetic BES measurements of GS2-simulated density field: (a) radial correlation length $l_R^{\mathrm{SYNTH}}$ (Section 5.2.1), (b) poloidal correlation length $l_Z^{\mathrm{SYNTH}}$ (Section 5.2.2), (c) correlation time $\tau_c^{\mathrm{SYNTH}}$ (Section 5.2.3), and (d) RMS fluctuation amplitude $(\delta n_i/n_i)_{\mathrm{rms}}^{\mathrm{SYNTH}}$ (Section 5.2.5) as functions of $\kappa_T$ and for several values of $\gamma_E$ within experimental uncertainty. The circled points indicate the simulations match match the experimental heat flux, given in Table 4.1. The dashed lines indicate the experimental values and the shaded areas the associated error at $r = 0.8$ obtained from interpolating between experimental measurements seen in Figure 5.5, which correspond to the local equilibrium configuration studied in these simulations.

to the BES specifications [54], the approximate resolution limit in the radial and poloidal directions is $\sim 2$ cm, the physical separation between BES channels. More recent work studying the measurement effect of the PSFs, concluded that the radial resolution limit can be between 2 and 4 cm depending on the orientation of the PSFs for a given config-

uration [66]. It is therefore likely that the results shown in Figure 5.6(a) simply confirm the radial resolution limit of the experimental analysis and the true value of $l_R$ may be lower than 2 cm (as suggested by Figure 5.1). We will confirm this in Section 5.5, where we consider the correlation properties of the raw GS2 density fluctuations.

Figures 5.6(b)–(d) give $l_Z^{\mathrm{SYNTH}} = 10$–$15$ cm, $\tau_c^{\mathrm{SYNTH}} = 2$–$15$ $\mu$s, and $(\delta n_i/n_i)_{\mathrm{rms}}^{\mathrm{SYNTH}} \sim 0.005$–$0.03$. We see that these correlation parameters match experimental measurements for certain combinations of $\kappa_T$ and $\gamma_E$. The values of $l_Z^{\mathrm{SYNTH}}$ are scattered around the experimental value $l_Z^{\mathrm{EXP}} = 14.06 \pm 0.09$ cm, showing no clear trend. While none of the cases that match the experimental heat flux (circled cases) match $l_Z^{\mathrm{EXP}}$, there are several simulations within the experimental uncertainty ranges of $\kappa_T$ and $\gamma_E$ that do match. Similarly, there are several values of $\tau_c^{\mathrm{SYNTH}}$ that match $\tau_c^{\mathrm{EXP}}$, including two cases that match the experimental level of heat flux. This is an important improvement over previous nonlinear gyrokinetic simulations of this MAST discharge [65], which overpredicted $\tau_c^{\mathrm{SYNTH}}$ by two orders of magnitude. Examining Figure 5.6(d), we see that $(\delta n_i/n_i)_{\mathrm{rms}}^{\mathrm{SYNTH}}$ increases with increasing $\kappa_T$ or decreasing $\gamma_E$, and that increasing $\gamma_E$ leads to a increase in the value of $\kappa_T$ required to achieve the same $(\delta n_i/n_i)_{\mathrm{rms}}^{\mathrm{SYNTH}}$. The latter is consistent with Figure 4.3(a), which showed that increasing $\gamma_E$ shifted the nonlinear turbulence threshold to higher $\kappa_T$. While Figure 5.6(d) shows that there is agreement between $(\delta n_i/n_i)_{\mathrm{rms}}^{\mathrm{SYNTH}}$ and $(\delta n_i/n_i)_{\mathrm{rms}}^{\mathrm{EXP}}$ at certain combinations of $(\kappa_T, \gamma_E)$, we see that the circled cases, representing simulations that match the experimental heat flux, have values of $(\delta n_i/n_i)_{\mathrm{rms}}^{\mathrm{SYNTH}}$ well below $(\delta n_i/n_i)_{\mathrm{rms}}^{\mathrm{EXP}}$. This may suggest that some effects are missing from the synthetic diagnostic procedure. For example, a more comprehensive analysis could be performed by translating both density *and* temperature fluctuations to fluctuating emission intensity [62]. We note that this discrepancy between simulation and experimental density fluctuation measurements has been observed in previous BES diagnostic studies [62, 63, 117], and so further work is clearly necessary.

One phenomenon that was not present in our simulations but is present in the experiment is high-energy radiation (e.g., neutron, gamma ray, or hard X-ray) impinging on the BES detectors. These photons cause high-amplitude spikes in the time series, which are typically confined to a single detector channel and, therefore, uncorrelated

with other channels. These radiation spikes then give rise to large auto-correlations at zero time delay, which are unrelated to the turbulent field that is being measured. A numerical "spike filter" is normally used to remove radiation spikes by identifying changes above a certain threshold between one time point and the next, and replacing the high-intensity value with the value of a neighbouring point [55, 118]. This "spike filter" is an important component of the experimental analysis of BES data and, while our simulations do not include such sources of radiation, we have included it in the analysis of our simulated density fluctuations for consistency with experimental analysis. For completeness, the results without the "spike filter" are given in Appendix E. The results show little difference to those with the "spike filter" except for the value of $l_Z$. We found that in some cases, fast-moving structures in the poloidal direction (especially the long-lived structures found in our simulations close to the turbulence threshold) were removed by the "spike" filter and therefore did not contribute to the poloidal correlation function, resulting in a drop in $l_Z$. In particular, Figure E.1(b) in Appendix E shows that $l_Z$ increased significantly in marginal cases compared to the results with the "spike filter", which may be dominated by coherent structures, since structures were no longer removed by the "spike filter".

From the above results we can conclude that local gyrokinetic simulations are a reasonable approximation to the experimental turbulence. We showed that all correlation parameters apart from $l_R^{\mathrm{EXP}}$ show reasonable agreement with the experimental measurements within the experimental-uncertainty ranges. This shows that from the point of view of turbulence measured by the BES diagnostic, the experimental turbulence and the synthetic turbulence are comparable.

Unlike the experiment, we have the raw density fluctuations, as calculated by GS2. In the next section we will repeat (and extend) the correlation analysis presented in this section for the raw density fluctuations.

## 5.5 Correlation analysis of raw GS2 data

Having considered the structure of turbulence processed through a synthetic BES diagnostic, we now want to investigate the raw GS2 density fluctuations, which will

allow us to (i) study the (distorting) effect of the synthetic diagnostic, (ii) study the parallel structure using GS2 data along the field line, and (iii) consider our entire parameter scan to understand how the structure of turbulence in MAST might change with the equilibrium parameters $\kappa_T$ and $\gamma_E$. This extends the previous analysis and comparison with simulations performed for this MAST discharge [65], which only considered for equilibrium parameters for a single equilibrium configuration and simulations with a synthetic diagnostic applied.

### 5.5.1 Correlation parameters within experimental uncertainty

We start by considering the correlation analysis results for simulations with values of $\kappa_T$ and $\gamma_E$ within the experimental uncertainty. The only operations applied to the raw density-fluctuation field output by GS2 are the transformation to the laboratory frame using equation (D.1) and the transformation from the GS2 parallel coordinate $\theta$ to the real-space coordinate $\lambda$, as described in Appendix D. Our correlation analysis is performed over a square $(R, Z)$-plane $20 \times 20$ cm$^2$ in size, located at the centre of our computational domain (see Figure D.2). We do this to analyse a region of similar size to the region probed by the BES diagnostic and also to avoid the real-space remapping effect at the edges of the radial domain inherent to the GS2 implementation of flow shear (see Section 3.4.3).

#### Correlation parameters

Figure 5.7 shows the radial correlation length $l_R^{\mathrm{GS2}}$, the poloidal correlation length $l_Z^{\mathrm{GS2}}$, correlation time $\tau_c^{\mathrm{GS2}}$, and RMS density fluctuation $(\delta n_i/n_i)_{\mathrm{rms}}^{\mathrm{GS2}}$ calculated for our GS2 density-fluctuation field. The results shown in Figure 5.7 are for a range of values of $\kappa_T$ and for $\gamma_E = [0.14, 0.16, 0.18]$, with circled points describing the simulations that match the experimental value of the heat flux. The results are as follows.

We find that the radial correlation length is $l_R^{\mathrm{GS2}} \sim 1$–$1.5$ cm, increasing with $\kappa_T$ and decreasing with $\gamma_E$. This suggests that $l_R^{\mathrm{GS2}}$ has a tendency to increase with $Q_i/Q_{\mathrm{gB}}$, as we will show explicitly later. In comparison with the synthetic diagnostic results shown in Figure 5.6(a), where $l_R^{\mathrm{SYNTH}} \sim 2$ cm, the true radial correlation length of the

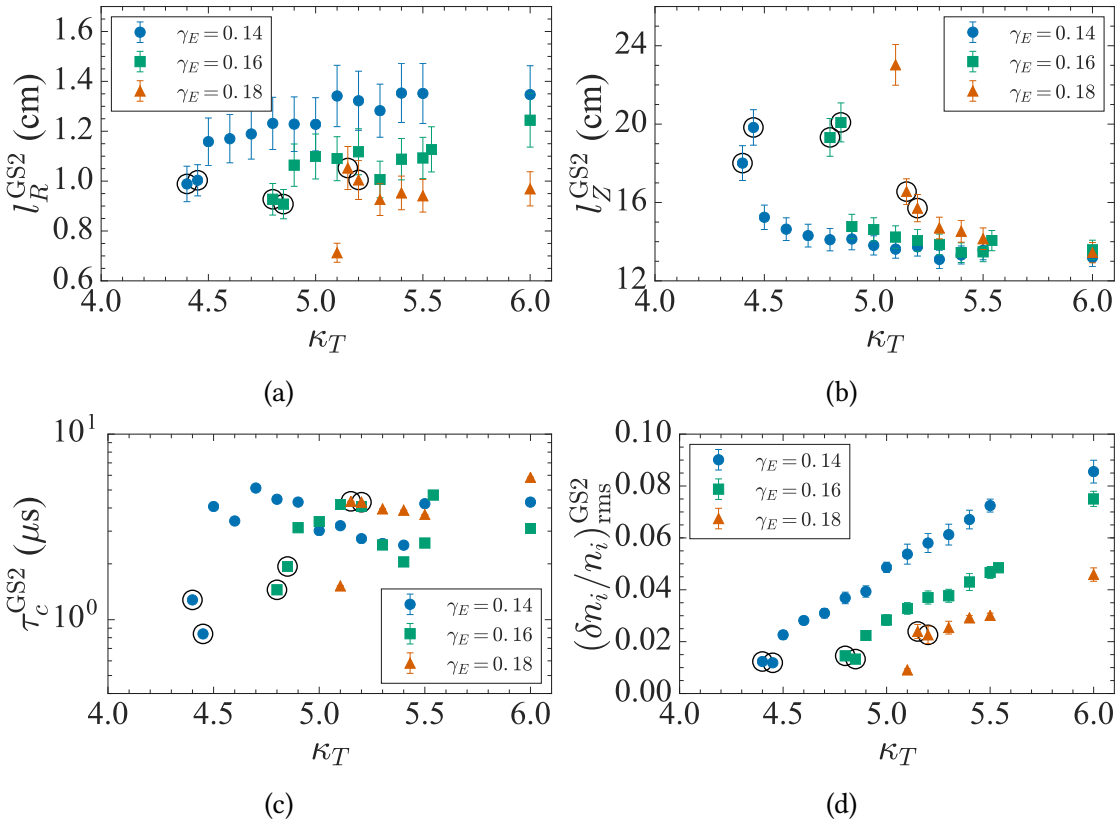



Figure 5.7: Correlation parameters calculated for raw GS2 density fluctuations for $(\kappa_T, \gamma_E)$ within the region of experimental uncertainty indicated in Figure 4.1: (a) radial correlation length $l_R^{\mathrm{GS2}}$ (Section 5.2.1), (b) poloidal correlation length $l_Z^{\mathrm{GS2}}$ keeping $k_y$ fixed to $k_y = 2\pi/l_Z$ (Section 5.2.2), (c) correlation time $\tau_c^{\mathrm{GS2}}$ (Section 5.2.3), and (d) RMS density fluctuations $(\delta n_i/n_i)_{\mathrm{rms}}^{\mathrm{GS2}}$ (Section 5.2.5).

turbulence $l_R^{\mathrm{GS2}}$ is below 2 cm and, therefore, below the resolution threshold of the BES diagnostic (discussed in Section 5.4).

Figure 5.7(b) shows that the poloidal correlation length is $l_Z^{\mathrm{GS2}} \sim 13$–$20$ cm, keeping the poloidal wavenumber $k_Z^{\mathrm{GS2}}$ fixed to $k_Z^{\mathrm{GS2}} = 2\pi/l_Z^{\mathrm{GS2}}$ (giving $k_Z^{\mathrm{GS2}} \sim 30$–$50$ m$^{-1}$). In contrast to $l_R^{\mathrm{GS2}}$, we see that $l_Z^{\mathrm{GS2}}$ decreases rapidly as $\kappa_T$ is increased from its value at the turbulence threshold.

The correlation time [Figure 5.7(c)] does not vary significantly with $\kappa_T$ or $\gamma_E$ and is in the range $\tau_c^{\mathrm{GS2}} \sim 1$–$6$ $\mu$s.

Table 5.1: Summary of results for the correlation parameters $l_R$, $l_Z$, $\tau_c$, and $(\delta n_i/n_i)_{\rm rms}$ from experimental BES measurements (EXP), from the correlation analysis of GS2 density fluctuations with synthetic diagnostic applied (SYNTH) using an identical correlation analysis to that used on the BES data, and from the correlation analysis of raw GS2 density fluctuations (GS2).

| Parameter | EXP | SYNTH | GS2 |
|---|---|---|---|
| $l_R$ (cm) | $3 \pm 0.4$ | 2 | 1–1.5 |
| $l_Z$ (cm) | $14.06 \pm 0.09$ | 10–15 | 13–20 |
| $\tau_c$ ($\mu$s) | $3.2 \pm 0.4$ | 2–15 | 1–6 |
| $(\delta n_i/n_i)_{\rm rms}$ | $0.0214 \pm 0.0006$ | 0.005–0.03 | 0.01–0.08 |

Finally, Figure 5.7(d) shows that $(\delta n_i/n_i)^{\rm GS2}_{\rm rms} \sim 0.01$–$0.08$ and increases with increasing $\kappa_T$ or decreasing $\gamma_E$, i.e., has an upward tendency as heat flux increases.

**Comparisons between experimental and GS2 correlation properties**

We have presented the correlation parameters measured (i) by the BES diagnostic in Section 5.3, (ii) from GS2 density fluctuations with the synthetic diagnostic applied in Section 5.4, and (iii) from the raw GS2 density fluctuations. We show the results from all these analyses in Table 5.1. We can summarise the comparison between simulation results and experimental measurements as follows. Comparing the results of the correlation analysis of the GS2 density fluctuations with the experimental measurements, we see that the all the experimental values, except for the radial correlation length $l_R$, fall within the ranges found for the simulation results. This is particularly important in the case of $\tau_c$, which was significantly overestimated in the previous modelling effort for this MAST discharge [65]. It is clear that the correlation parameters vary with the equilibrium parameters and there is no single simulation, i.e., no single combination of $(\kappa_T, \gamma_E)$, that perfectly matches the BES measurements in all four parameters (see Figure 5.7), even for the correlation parameters where there is overlap between the experimental value and the simulation ranges.

Considering the difference between the GS2 density fluctuations with and without the synthetic diagnostic gives us an indication of the effect of the PSFs on the measure-

ment of turbulence correlation properties. Given that the value of $l_R$ measured from the raw GS2 density fluctuations is below the approximate resolution threshold, it is unclear what effect the PSFs have on the radial correlation length $l_R$. We see from Table 5.1 that the ranges of values of the poloidal correlation length $l_Z$ are comparable in the SYNTH and GS2 cases. However, Figure 5.6(b) shows that, with the synthetic diagnostic applied, we do not see the clear trends versus $\kappa_T$ that we see in Figure 5.7(b). This may be due to the limited poloidal resolution, which can resolve the measured correlation lengths, but is not sensitive enough to recover the trend of decreasing $l_Z$ with $\kappa_T$ seen in Figure 5.7(b). The measurement of the correlation time $\tau_c$ is, again, less certain in the case of the correlation analysis of density fluctuations with a synthetic diagnostic applied, but there is reasonable agreement with the correlation time measured from the raw GS2 density fluctuations. Finally, the application of the synthetic diagnostic leads to a reduction of roughly $50\%$ of the RMS fluctuation amplitude, i.e., from $(\delta n_i/n_i)^{\mathrm{GS2}}_{\mathrm{rms}} \sim 0.01$–$0.08$ for the raw density fluctuations to $(\delta n_i/n_i)^{\mathrm{SYNTH}}_{\mathrm{rms}} \sim 0.005$–$0.03$. This observation is consistent with a recent detailed analysis of the effect of PSFs on the measurement of MAST turbulence using a subset of GS2 simulations found in this work [66].

**Poloidal and parallel correlation parameters**

We now consider two further diagnostics, which were not available to us experimentally: the poloidal and parallel correlation lengths and wavenumbers calculated as independent fitting parameters to the corresponding correlation functions (see Sections 5.2.2 and 5.2.4). As explained in Section 5.2.2, the higher poloidal resolution of GS2 data compared to the experimental BES measurements allows us to fit the poloidal correlation function with $l_Z$ and $k_Z$ as independent fitting parameters. In addition, GS2 predicts density fluctuations in the parallel direction allowing us to calculate parallel correlation functions.

Figures 5.8(a) and (b) show the result of such fitting: $l^{\mathrm{GS2}}_{Z,\mathrm{free}}$ and $k^{\mathrm{GS2}}_{Z}$ versus $\kappa_T$. As already anticipated by Figure 5.2, we see a roughly $50\%$ decrease in $l^{\mathrm{GS2}}_{Z,\mathrm{free}}$ compared to $l^{\mathrm{GS2}}_{Z}$ [Figure 5.7(b)], from $13$–$20$ cm to $7$–$10$ cm, again decreasing as $\kappa_T$ increases or $\gamma_E$ decreases. The value of $k^{\mathrm{GS2}}_{Z,\mathrm{free}}$ is in the range $35$–$45\ \mathrm{m}^{-1}$ – comparable to one obtained via fitting the procedure where $k_Z = 2\pi/l_Z$. Regardless of the fitting method, Figure 5.7(b)

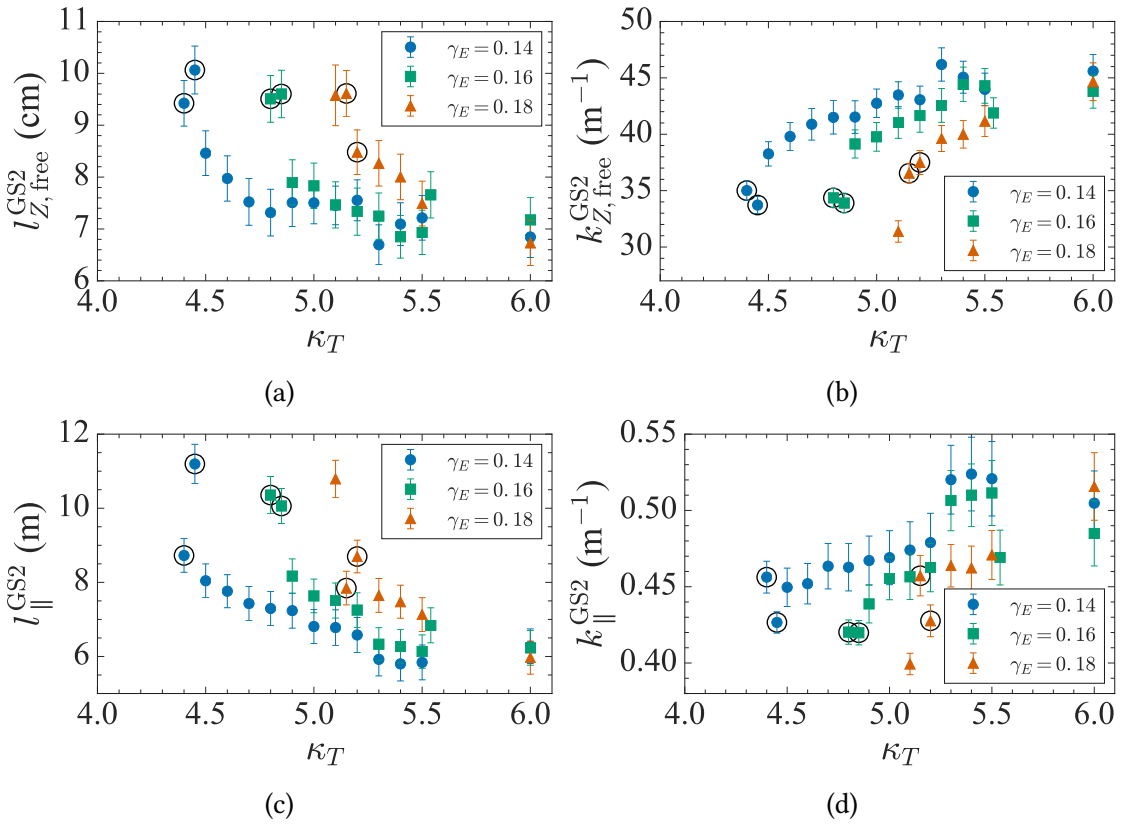



Figure 5.8: Correlation parameters calculated for raw GS2 density fluctuations for $(\kappa_T, \gamma_E)$ within the region of experimental uncertainty indicated in Figure 4.1: (a) poloidal correlation length $l_{Z,\mathrm{free}}^{\mathrm{GS2}}$ with $k_y$ as a free fitting parameter, (b) poloidal wavenumber $k_{Z,\mathrm{free}}^{\mathrm{GS2}}$ (Section 5.2.2), (c) parallel correlation length $l_{\parallel}^{\mathrm{GS2}}$, and (d) parallel wavenumber $k_{\parallel}^{\mathrm{GS2}}$ (Section 5.2.4).

and Figure 5.8(a) show a similar dependence of $l_Z$ on $\kappa_T$ and $\gamma_E$.

Currently the BES diagnostic on MAST is not capable of determining both $l_Z$ and $k_Z$, but these estimates may be used for future comparisons between experimental measurements and numerical results if higher-resolution BES measurements become available. Similarly there is currently no diagnostic on MAST capable of measuring the parallel correlation length, but our estimates may guide future attempts at designing diagnostics to measure it.

The results of the parallel correlation analysis, given in Figure 5.8(c) and (d), are the

values $l_\parallel^{\mathrm{GS2}}$ and $k_\parallel^{\mathrm{GS2}}$ versus $\kappa_T$. We see that $l_\parallel^{\mathrm{GS2}} \sim 6$–$12$ m and decreases with increasing $\kappa_T$ and decreasing $\gamma_E$. Based on this measurement of the parallel correlation length, it is clear that the turbulence is highly anisotropic, i.e., $l_\parallel \gg l_\perp$, as it is expected to be [49].

Using the measurement of $l_\parallel^{\mathrm{GS2}}$, we can return to, and confirm, the assumption upon which the calculation of $\tau_c$ depends. In Section 5.2.3, we assumed that reliably estimating the correlation time depends on the temporal decorrelation dominating over effects due to the finite parallel correlation length [see (5.5)]. Using the value of $l_\parallel$ above, we can estimate that $l_\parallel \cos\vartheta/u_\phi \sim 80$–$160$ $\mu$s, where we have used $R = 1.32$ m, $\omega = 4.71 \times 10^4$ $\mathrm{s}^{-1}$, and $\vartheta \approx 0.6$. This confirms that $\tau_c$ is smaller than $l_\parallel \cos\vartheta/u_\phi$ by more than an order of magnitude and that the time correlation analysis is valid in this MAST configuration.

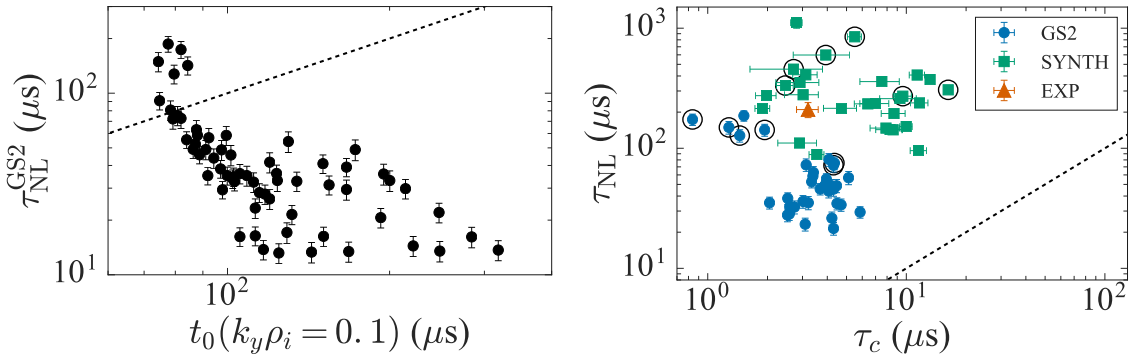
### Comparison between linear and nonlinear time scales

With the knowledge of the correlation parameters, we can return to the comparison of the transient-growth time $t_0$ and nonlinear time $\tau_{\mathrm{NL}}$ discussed in section 4.3. In particular, we want to determine one of the two conditions for the onset of subcritical turbulence [equation (4.2)] proposed in Ref. [38]. We also follow Ref. [65] and compare $\tau_{\mathrm{NL}}$ with the correlation time of the turbulence $\tau_c$ and compare with the corresponding experimental results.

The non-zonal nonlinear interaction time is estimated to be [69]:

$$\tau_{\mathrm{NL}}^{-1} = \frac{v_{\mathrm{th}i}\rho_i}{l_R l_Z}\frac{T_e}{T_i}\left(\frac{\delta n_i}{n_i}\right)_{\mathrm{rms}}, \tag{5.10}$$

where we have assumed $l_Z \approx l_y$ (where $l_y$ is the correlation length in the binormal direction as defined in [69]) because $l_Z = l_y \cos\vartheta$, where $\vartheta$ is the magnetic field pitch-angle (see Figure D.1), and $\cos\vartheta \sim 1$ for this magnetic equilibrium. The transient-growth time $t_0$ was calculated from linear simulations and plotted in Figure 4.7, showing that, at ion scales, the longest transient growth occurred at $k_y\rho_i \sim 0.1$. Figure 5.9(a) shows $\tau_{\mathrm{NL}}^{\mathrm{GS2}}$ versus $t_0$ (at $k_y\rho_i = 0.1$) for all simulations with $\gamma_E > 0$, where the dashed line indicates $\tau_{\mathrm{NL}}^{\mathrm{GS2}} = t_0$. We see that the majority of simulations are below the line defined by $\tau_{\mathrm{NL}}^{\mathrm{GS2}} = t_0$, showing that the condition for the onset of turbulence given by (4.2) is approximately true, i.e., that $t_0 \gtrsim \tau_{\mathrm{NL}}$.




(a) (b)

Figure 5.9: (a) Nonlinear interaction time of the raw density fluctuations $\tau_{\rm NL}^{\rm GS2}$, calculated using (5.10), versus the transient-growth time $t_0$. We have taken $t_0$ at $k_y\rho_i = 0.1$, where $t_0$ is largest (see Figure 4.7). We show all simulations in our parameter scan with $\gamma_E > 0$. (b) $\tau_{\rm NL}$ versus $\tau_c$ for the correlation parameters calculated from the raw GS2 density fluctuations (GS2), from density fluctuations with the synthetic diagnostic applied (SYNTH), and from experimental measurements (EXP). The cases shown are for values of $(\kappa_T, \gamma_E)$ within experimental uncertainty and the circled simulations indicate the simulations that match the experimental heat flux. The dashed lines in each plot indicate where the time scales are equal.

Ref. [65] compares $\tau_{\rm NL}$ with the turbulence correlation time $\tau_c$, both calculated from experimental measurements, and provides another possible point of comparison using the results from our correlation analysis of raw GS2 density fluctuations. Figure 5.9(b) shows $\tau_{\rm NL}$ versus $\tau_c$ for nonlinear simulations with values of $(\kappa_T, \gamma_E)$ within experimental uncertainty. The values of $\tau_{\rm NL}$ were calculated from correlation parameters of raw GS2 density fluctuations (GS2), from correlation parameters calculated from GS2 density fluctuations with a synthetic diagnostic applied (SYNTH), and from the experimental BES measurements at $r = 0.8$ (EXP). The dashed line indicates a line defined by $\tau_{\rm NL} = \tau_c$. First, we see that $\tau_{\rm NL} > \tau_c$ for both the GS2 and SYNTH cases, consistent with the experimental value: the red triangle at approximately $(\tau_{\rm NL}, \tau_c) = (3, 2 \times 10^2)$. Secondly, we see that $\tau_{\rm NL}$ for the raw GS2 density fluctuations tends to be below the experimental value, whereas the SYNTH cases are comparable. The results shown in Figure 5.9(b) are consistent with the experimental results in [65] that showed $\tau_{\rm NL} > \tau_c$ for this and other experimental cases, and so gives us further confidence in the ability

of GS2 to predict the properties of turbulence in MAST. However, we can also conclude from Figure 5.9(b) that $\tau_{\mathrm{NL}} \gg \tau_c$ in all cases, with $\tau_{\mathrm{NL}}$ being up to three orders of magnitude larger in some cases. The value of $\tau_c$ is measured from the turbulence itself, and so Figure 5.9(b) suggests that the estimate of $\tau_{\mathrm{NL}}$ (5.10) can significantly overestimate the actual interaction time, given that it does not make sense to consider the interaction of eddies (over a time scale $\tau_{\mathrm{NL}}$) that have already decorrelated (over a much shorted time scale $\tau_c$).

### 5.5.2 Correlation parameters versus $Q_i/Q_{\mathrm{gB}}$

The correlation analysis results in Figures 5.7 and 5.8, in particular $l_Z^{\mathrm{GS2}}$, $(\delta n_i/n_i)_{\mathrm{rms}}^{\mathrm{GS2}}$, and $l_{\parallel}^{\mathrm{GS2}}$, show similar trends versus $\kappa_T$ for different values of $\gamma_E$. As we showed in Figure 4.1, increasing $\kappa_T$ or decreasing $\gamma_E$ effectively amounts to controlling the distance from the turbulence threshold. Furthermore, our investigations of the transition to turbulence (see [108] and Section 4.3) and the effect of flow shear on its structure [118] suggest that the key determining factor is the distance from the threshold. This is most conveniently parametrised by the ion heat flux $Q_i/Q_{\mathrm{gB}}$. Here we describe the results of our correlation analysis of raw GS2 density fluctuations as a function of this parameter.

Figures 5.10 and 5.11 show the correlation parameters from Figures 5.7 and 5.8 as functions of $Q_i/Q_{\mathrm{gB}}$ for our entire parameter scan, including $\gamma_E = 0$. These figures clearly show that it is distance from threshold that determines the structure of turbulence and characterise this structure for realistic MAST configuration and for a large range of $Q_i/Q_{\mathrm{gB}}$. We start by discussing the $\gamma_E > 0$ cases, which we can characterise as follows.

We see a roughly monotonic increase in the radial correlation length $l_R^{\mathrm{GS2}}$ [Figure 5.10(a)], which is consistent with an increasing $Q_i/Q_{\mathrm{gB}}$ because the formation of larger radial structures is one way the turbulence can transport heat more effectively.

Figure 5.10(b) [along with figures 5.11(a) and (b)] shows the poloidal correlation length $l_Z^{\mathrm{GS2}}$ decreasing (and the corresponding wavenumber $k_Z^{\mathrm{GS2}}$ increasing) with increasing $Q_i/Q_{\mathrm{gB}}$. Again, this is consistent with an increasing $Q_i/Q_{\mathrm{gB}}$, where structures which are poloidally thin (large $k_Z$) are the most efficient at transporting heat out of the plasma, according to (4.7) (given $k_Z \propto k_y$). However, an increase in amplitude may also

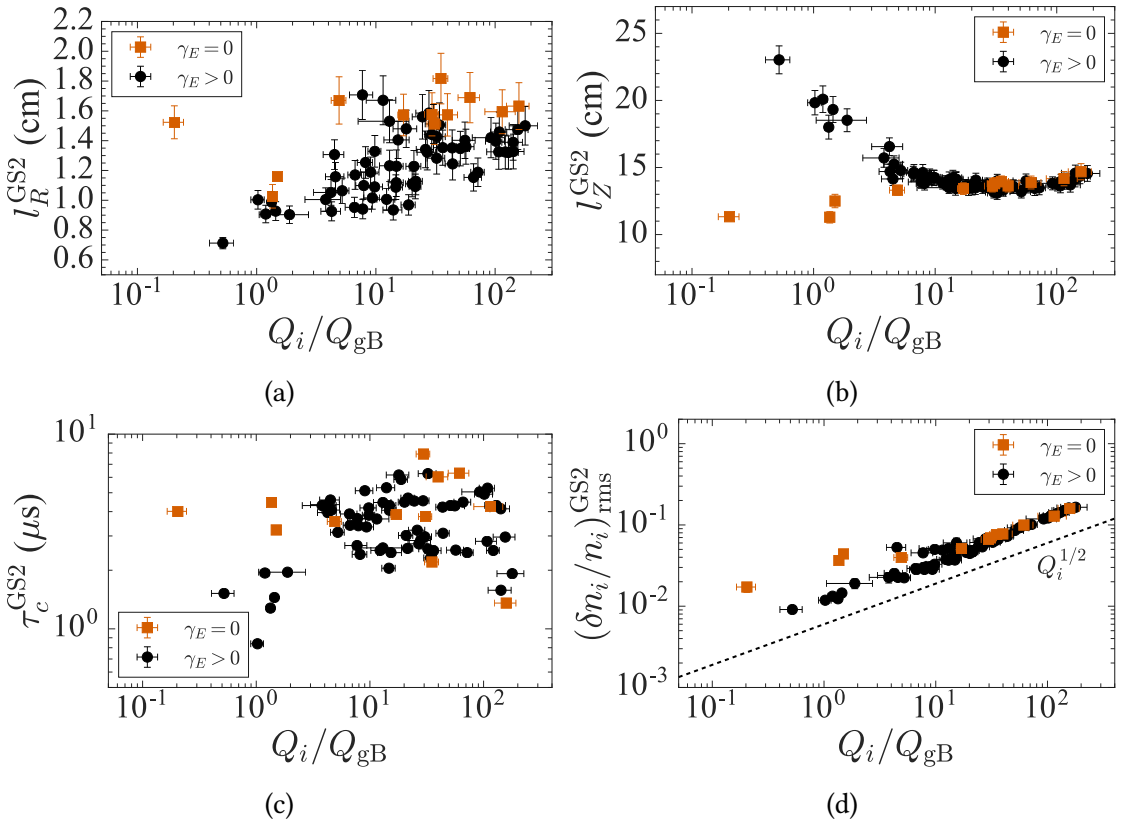



Figure 5.10: Correlation parameters calculated for raw GS2 density fluctuations for the entire parameter scan as a function of $Q_i/Q_{\mathrm{gB}}$: (a) radial correlation length $l_R^{\mathrm{GS2}}$ (Section 5.2.1), (b) poloidal correlation length $l_Z^{\mathrm{GS2}}$ keeping $k_y$ fixed to $k_y = 2\pi/l_Z$ (Section 5.2.2), (c) correlation time $\tau_c^{\mathrm{GS2}}$ (Section 5.2.3), and (d) RMS density fluctuations $(\delta n_i/n_i)_{\mathrm{rms}}^{\mathrm{GS2}}$ (Section 5.2.5), where the dashed line indicates the scaling (4.7).

lead to increased heat transport and so radially elongated and poloidally thin turbulent structures are not necessarily expected for turbulence in general. Figure 5.10(b) shows that $l_Z^{\mathrm{GS2}}$ decreases to roughly 14 cm for $Q_i/Q_{\mathrm{gB}} \sim O(10)$ and possibly starts *increasing* again for $Q_i/Q_{\mathrm{gB}} \sim O(100)$. Theoretical and numerical estimates of the scaling of $l_Z$ far from the turbulence threshold suggested that $l_Z \sim q\kappa_T$ [67]. While our data shows that the value of $l_Z^{\mathrm{GS2}}$ increases at large $Q_i/Q_{\mathrm{gB}}$, further simulations at higher $\kappa_T$ are necessary to confirm whether our simulations adhere to this scaling.

The RMS density fluctuations $(\delta n_i/n_i)_{\mathrm{rms}}^{\mathrm{GS2}}$ [Figure 5.10(d)] increase as $(Q_i/Q_{\mathrm{gB}})^{1/2}$

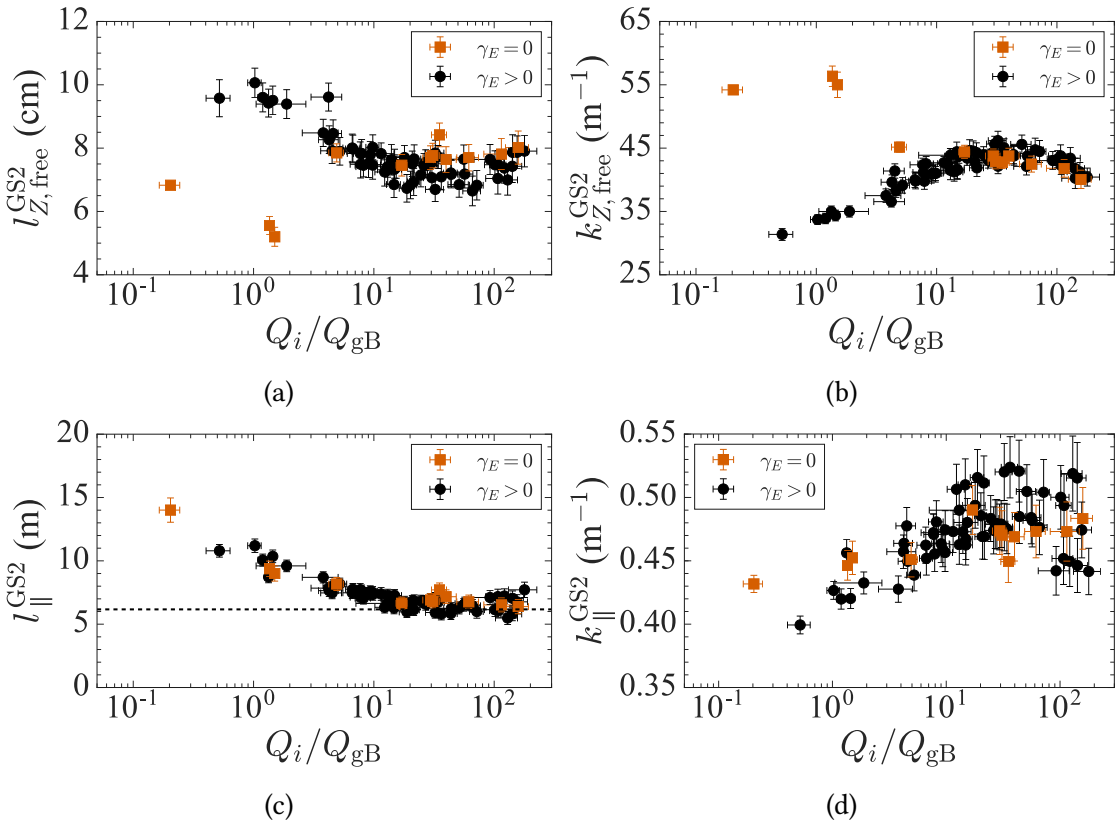



Figure 5.11: Correlation parameters calculated for raw GS2 density fluctuations for the entire parameter scan as a function of $Q_i/Q_{\mathrm{gB}}$: (a) poloidal correlation length $l^{\mathrm{GS2}}_{Z,\mathrm{free}}$ with $k_y$ as a free fitting parameter, and (b) poloidal wavenumber $k^{\mathrm{GS2}}_{Z,\mathrm{free}}$ (Section 5.2.2), (c) parallel correlation length $l^{\mathrm{GS2}}_{\parallel}$, and (d) parallel wavenumber $k^{\mathrm{GS2}}_{\parallel}$ (Section 5.2.4). The dashed line in (c) indicates a line of $l_{\parallel} \sim qR$ (see main text).

far from threshold, as expected from the scaling (4.7). However, in contrast to the results in Figure 4.15, we do not see a flattening of $(\delta n_i/n_i)^{\mathrm{GS2}}_{\mathrm{rms}}$ at low $Q_i/Q_{\mathrm{gB}}$ (as in Figure 4.15, where we plotted the *maximum* amplitude), for $\gamma_E > 0$ simulations. This is due to the relatively little volume taken up by the coherent structures and, hence, their small contribution to the RMS value. We verified this by calculating the RMS density fluctuations while excluding varying amounts of the turbulence structures (near the threshold) and found that the RMS value did not change very much, showing that for the cases near the threshold the RMS value is dominated by the low-amplitude density fluctuations.

Finally, we see that the parallel correlation length $l_{\parallel}^{\mathrm{GS2}}$ [Figure 5.11(c)] decreases as the system is taken away from the turbulence threshold. Estimates of $l_{\parallel}$ for strongly driven ITG turbulence [67] suggested that $l_{\parallel}$ should be proportional to the connection length, i.e., $l_{\parallel} \sim \pi q R$. This estimate is indicated by the dashed line in Figure 5.11(c), and we see that, indeed, $l_{\parallel}$ is of the order of the connection length.

We have highlighted cases for which $\gamma_E = 0$ (red) and $\gamma_E > 0$ (black) in Figures 5.10 and 5.11 to highlight two important features of sheared versus unsheared turbulence previously discussed in Section 4.4. First, close to the turbulence threshold, the cases with $\gamma_E = 0$, represent a different regime of turbulence to those cases with $\gamma_E > 0$. In particular, $l_Z^{\mathrm{GS2}}$ shown in Figure 5.10(b) [as well as Figures 5.11(a) and (b)], shows an *increasing* trend for cases with $\gamma_E = 0$: from $\sim 10$ cm near the turbulence threshold to $\sim 15$ cm far away from it, whereas cases with $\gamma_E > 0$ *decrease* from $\sim 23$ cm near marginality to $\sim 15$ cm far away from it. This represents a different dependence on $Q_i/Q_{\mathrm{gB}}$ as well as showing a significantly lower value of $l_Z^{\mathrm{GS2}}$ at experimentally relevant $Q_i/Q_{\mathrm{gB}}$ ($= 2 \pm 1$). Figure 5.10(c) shows that $\tau_c^{\mathrm{GS2}}$ predicted by $\gamma_E = 0$ simulations stays roughly constant over a large range of $Q_i/Q_{\mathrm{gB}}$ whereas for $\gamma_E > 0$ simulations, $\tau_c^{\mathrm{GS2}}$ diminishes rapidly for small $Q_i/Q_{\mathrm{gB}}$. Secondly, we see that far from the threshold, the $\gamma_E = 0$ and $\gamma_E > 0$ cases for *all* correlation parameters show the same dependence on $Q_i/Q_{\mathrm{gB}}$. This shows that far from the threshold there is little difference between sheared and unsheared (by a background flow) turbulence. This result is consistent with the results in Section 4.4.5, further confirming the conclusions reached in Section 4.4.5: close to the turbulence threshold the background flow shear has a significant effect on the turbulence leading to reduced heat transport (as shown in Chapter 4), whereas far from the threshold the turbulence is much like conventional ITG-driven turbulence in the absence of flow shear. This has been studied in related work [118], which attempted to argue a similar case in terms of symmetry breaking of fluctuation spectra close to the threshold in the presence of flow shear. Far from the threshold, however, the symmetry is effectively restored, and resembles turbulence in the absence of flow shear.

## 5.6 Summary

In this chapter, we made quantitative comparisons between our GS2 simulations and the experimental measurements from the BES diagnostic. We first presented an overview of the correlation techniques in Section 5.2, developed in Ref. [69], to measure the properties of turbulence from density fluctuations and extended the correlation analysis to the parallel direction, in which it is not currently possible to measure density fluctuations in order to calculate correlation lengths. The results from BES diagnostic measurements [65] were presented in Section 5.3.

In Section 5.4, we presented the first of our two correlation analyses, which looked strictly at simulations with equilibrium parameters within the experimental uncertainty ranges, we applied a synthetic diagnostic to the GS2 density-fluctuation fields before performing a correlation analysis exactly like the one used on experimental data. We showed reasonable agreement between our simulations and the BES measurements in the poloidal correlation length and correlation time (a major improvement compared to previous attempts at measuring this quantity). We also found that the radial correlation length was likely below the resolution threshold of the BES diagnostic. We showed agreement for the RMS density fluctuation amplitude within the experimental uncertainties of $\kappa_T$ and $\gamma_E$; however, this was at values of the equilibrium parameters far from those found to be relevant to the experiment, i.e., far from the turbulence threshold.

In Section 5.5, we performed a correlation analysis of the raw GS2 density fluctuations. We first presented the results within the experimental-uncertainty ranges of $\kappa_T$ and $\gamma_E$ and showed the following. We confirmed that the radial correlation tended to be below the resolution threshold of the BES diagnostic and showed that the poloidal correlation length and correlation times were comparable to both the results with a synthetic diagnostic applied and the experimental results. The effect of the synthetic diagnostic and associated PSFs was to reduce the measured density fluctuation amplitude compared to the raw GS2 density fluctuations. We compared the results from our two correlation analyses and experimental measurements and showed reasonable agreement across all the correlation properties of turbulence.

Calculating the nonlinear decorrelation time, we confirmed in Section 5.5.1 that the

onset of subcritical turbulence requires that the transient-growth time be approximately greater than the nonlinear interaction time in a given simulation. Furthermore, we showed that nonlinear interaction time tends to be much greater than the correlation times – in agreement with the experimental results in Ref. [65].

Finally, we showed that the correlation properties of the turbulence in our simulations are effectively determined by how far the system is from the turbulence threshold; quantified by the ion heat flux $Q_i/Q_{\mathrm{gB}}$. This was consistent with the results shown in Sections 4.3 and 4.4.5, which showed that the number of structures, their maximum amplitude, and the relative importance of zonal flows were also effectively functions of $Q_i/Q_{\mathrm{gB}}$. Presenting the data in this way highlighted two important properties of the turbulence: (i) close to the turbulence threshold, the background flow shear has a significant effect on the properties, and (ii) far from the threshold, the properties of sheared and unsheared turbulence were similar.

# Chapter 6

# *Conclusions*

We have simulated the conditions inside MAST discharge #27274 using local gyrokinetic simulations and performed a systematic parameter scan in the ion-temperature-gradient length scale $\kappa_T$ and the flow shear $\gamma_E$. We have demonstrated in Section 4.2 that, within experimental uncertainty, simulations reproduce the experimental ion heat flux and that the experimentally measured equilibrium gradients lie close to the turbulence threshold inferred from the simulations (see Figure 4.1). Importantly, this is one of the first numerical demonstrations that a MAST plasma is close to the turbulence threshold. The parameter scan performed in this work has clearly shown that $\kappa_T$ and $\gamma_E$ are useful control parameters, in agreement with several previous experimental and numerical studies [17, 25, 28, 29].

We have shown in Section 4.3, that the system is subcritical for $\gamma_E > 0$, i.e., finite initial perturbations, which we assume are generated by the experiment, are required in order to achieve a saturated nonlinear state. Subcriticality is a defining feature of this system: for $\gamma_E > 0$, even the largest values of $\kappa_T$ that we considered required large initial perturbations to ignite turbulence. Using linear and nonlinear simulations, we have estimated the conditions necessary for the onset of subcritical turbulence: we require that maximum transient-amplification factor be $N_{\gamma,\max} \gtrsim 0.4$ (see Figure 4.9), and that the transient-growth time $t_0$ be approximately greater than the nonlinear interaction time, i.e., $t_0 \gtrsim \tau_{\mathrm{NL}}$ (Section 5.5.1). These conditions were comparable to those in previous work for simpler systems [38]. Furthermore, we have showed that the linear dynamics

do not show significant changes as the turbulence threshold is passed, and so nonlinear simulations are essential in predicting the exact onset of subcritical turbulence.

Our simulations have shown that, near the turbulence threshold, a previously unreported turbulent state exists in which fluctuation energy is concentrated into a few coherent, long-lived structures, which have a finite minimum amplitude (Section 4.4.1). We have argued that this phenomenon is due to the subcriticality of the system, which cannot support arbitrarily small-amplitude perturbations (as in supercritical turbulence). We have investigated the changes in the nature of these nonlinear structures by tracking the maximum fluctuation amplitude (Section 4.4.3) and the number of structures (Section 4.4.4) as we changed our equilibrium parameters, and have shown the following. Near the turbulence threshold, the system is comprised of just a few finite-amplitude structures. As the system is taken away from the turbulence threshold, the number of these structures increases (at constant amplitude). Upon increasing in number sufficiently to fill the spatial simulation domain, they begin to increase in amplitude (at a roughly constant number of structures) (see Figures 4.15 and 4.17). Interestingly, the evolution of our system as the system is taken away from the turbulence threshold is reminiscent of the transition to subcritical turbulence via localised structures in pipe flows [45]. We have further shown that, in contrast to conventional ITG-driven turbulence regulated by zonal flows [99] (and their associated shear), in our system, close to the turbulence threshold, the shear due to the mean toroidal flow dominates over the shear due to the zonal flows. We have shown that the experimental gradients lie close to the threshold, meaning that it is essential to include the background flow shear in simulations of MAST plasmas. Only reasonably far from the turbulence threshold does the effect of the zonal shear and the flow shear due to the background flow become comparable (see Figure 4.19), and further still the turbulence becomes similar to ITG-driven turbulence in the absence of background flow shear.

We have made quantitative comparisons between density fluctuations in our simulations and those measured by the MAST BES diagnostic [54, 55] (Section 5). A correlation analysis [64] was previously performed on the measurements of density fluctuations from the BES diagnostic [65] (Section 5.3), giving the following properties of the turbulence: the radial correlation length $l_R$, the poloidal correlation length $l_Z$, and the

correlation time $\tau_c$. We have performed two types of correlation analysis on our simulated density fluctuations: one after applying a synthetic BES diagnostic (Section 5.4), and one directly on the raw GS2-generated density fluctuations (Section 5.5). We have compared these results to experimental measurements and achieved reasonable agreement of the correlation lengths, time, and amplitude measurements, except for the radial correlation length, which was predicted by us to be lower than the resolution limit of the BES diagnostic. Notably, the simulated and experimentally measured correlation times were in good agreement, unlike in previous global, gyrokinetic simulations of the same MAST discharge [65].

Finally, we have shown that the nature of the turbulence is effectively a function of the distance from the turbulence threshold [for example, see Figures 4.15, 4.17, 4.19(b), 5.10, and 5.11]. We have quantified this distance from threshold via the ion heat flux $Q_i/Q_{\mathrm{gB}}$, and have shown that it is this quantity, rather than the specific values of the equilibrium parameters $\kappa_T$ and $\gamma_E$, that determines the properties of the turbulence. Throughout this work, we have presented our data as functions of the distance from threshold to highlight the two distinct turbulence regimes that we have identified. Close to the threshold, where coherent structures dominate the dynamics, and far from the threshold, where the turbulence appears to be similar to conventional strongly driven ITG turbulence in the absence of flow shear. It is important to note that the experiment is located at the boundary of these two regimes, in parameter space, and may suggest that this boundary is most relevant to the experiment, as opposed to the boundary separating the non-turbulent and turbulent states — the so-called "zero-turbulence manifold" [102].

Using the local gyrokinetic code GS2, we have been able to reproduce both the experimental heat flux and the quantitative measurements of turbulence obtained using the BES diagnostic. This has given us confidence in our simulations and has allowed us to trust some conclusions from them that do not (yet) have direct experimental backing. More broadly, we have gained confidence in the future use of local gyrokinetic simulations in predicting turbulence and transport in high-aspect-ratio spherical tokamaks such as MAST.

## 6.1 Future directions

The most interesting experimental question that has arisen from this study is about the existence of the long-lived, coherent structures near the turbulence threshold, which support heat fluxes that are experimentally relevant. Given that these structures occur at ion scales, the BES diagnostic is well-suited for detecting them. However, as we have found in this investigation, the "spike filter", which plays an important role in cleaning experimental data of high-energy radiation, may complicate the detection of these structures, since it may erroneously remove long-lived, poloidally fast-moving structures. Currently, the "spike filter" is a simple and efficient algorithm to remove any spike in the emission above a certain threshold; however, future work might involve more carefully filtering out only high-energy radiation and ensuring that high-intensity emission that is correlated in time or across detectors (such as that produced by a fast moving structure) is not overlooked. It might also be possible to investigate the existence of structures statistically. Recent work on this question has provided some tentative but encouraging indications that a regime dominated by isolated structures might manifest itself in experimentally observed skewed probability distributions of density fluctuations [118]. Clearly, further more extensive analysis of MAST BES measurements is needed.

In addition to detecting the coherent structures in experiments, it may be useful to attempt to formulate an analytical description of their structure and behaviour. Our simulations were of a realistic experimental configuration; however, it may be possible to observe them in simpler systems and in this way identify the key physical mechanisms that give rise to them. Our simulations have identified the flow shear as a key physical mechanism and that the relevant part of parameter space where the structures are found, is close to the turbulence threshold. However, open questions remain regarding, for example, the importance of the MAST geometry, the influence of dissipation mechanisms such as collisions, and the role played by electron-scale turbulence.

In this work we have identified two regimes of turbulence: a coherent-structure-dominated regime and a more conventional ITG-turbulence regime. Future studies could attempt to more precisely identify the criteria that define the boundary between the two regimes, since it may be this boundary that is most relevant to experiments, as is the case

for the system we have investigated.

Finally, we may ask: how universal are the turbulence regimes that we have identified? First, with respect to other fusion devices and secondly, with respect to other subcritical systems. We have shown in Section 4.3 that even turbulence that has reached a saturated state may still be quenched at a seemingly unpredictable time. Previous work on subcritical systems in neutral fluid flow down a pipe [44, 105] and Keplerian magnetorotational accretion flows [107] have shown (using large numbers of experiments and/or numerical simulations) that subcritical turbulence has a finite life time and is a statistical property of the system that depends on how far the system is from the turbulence threshold, much like the ion heat flux in our study. Most recently, it has been shown, for neutral fluid flow down a pipe, that subcritical turbulence has a finite life time *regardless* of how far the system is from the turbulence threshold. Currently, our simulations are much too expensive to carry out the number of simulations required to determine the turbulence life time as in the above studies. However, it would be an exciting demonstration of the universality of subcritical turbulence if the turbulence life time could be shown to behave similarly in tokamak plasmas.

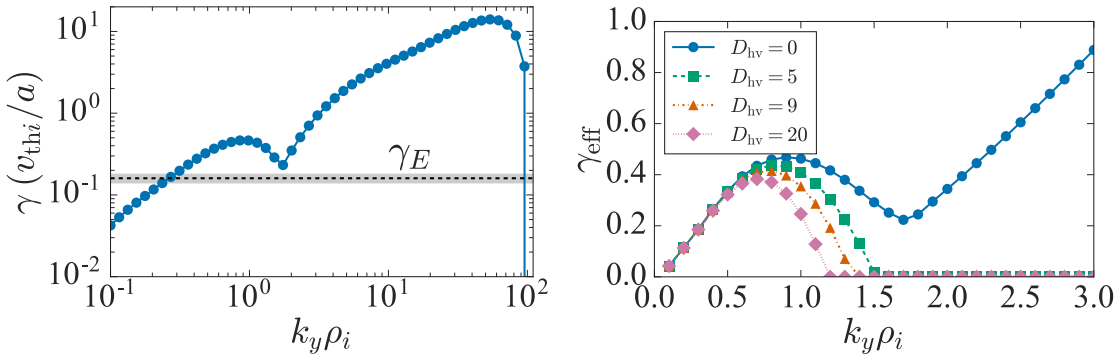
# Appendix A

# *Linear and nonlinear effect of hyperviscosity*

For the MAST configuration that we investigated, hyperviscosity was a key requirement in order for us to be able to run ion-scale-only simulations to saturation. To demonstrate the need for hyperviscosity, we start by considering the linear growth rate $\gamma$ (calculated with zero flow shear, $\gamma_E = 0$) over a range of $k_y\rho_i$ that covers both ion ($k_y\rho_i \sim 1$) and electron scales ($k_y\rho_i \gtrsim 10$). This is shown in Figure A.1(a). We see that there is no clear scale separation between ion- and electron-scale instabilities and, therefore, it is problematic to choose a maximum value of $k_y\rho_i$ at which our nonlinear simulations could naturally be cut off. Figure A.1(a) suggests that multiscale simulations, covering both ion and electron scales, are required as any intermediate cut-off scale would lead to finite growth at the smallest resolved scales.

Using equation (3.47) we can determine the effect of different levels of hyperviscosity on linear growth rate (in the absence of flow shear) without running additional linear simulations. Hyperviscosity is implemented as a wave-number-dependent factor applied to the distribution function at every time step, with the result that, in the presence of hyperviscosity, a perturbed quantity like $\varphi$ evolves in a linear simulations in time as

$$\varphi(t) \sim \exp\left[\left(\gamma - D_{\mathrm{hv}}\frac{k_\perp^4}{k_{\perp,\mathrm{max}}^4}\right)t\right], \tag{A.1}$$



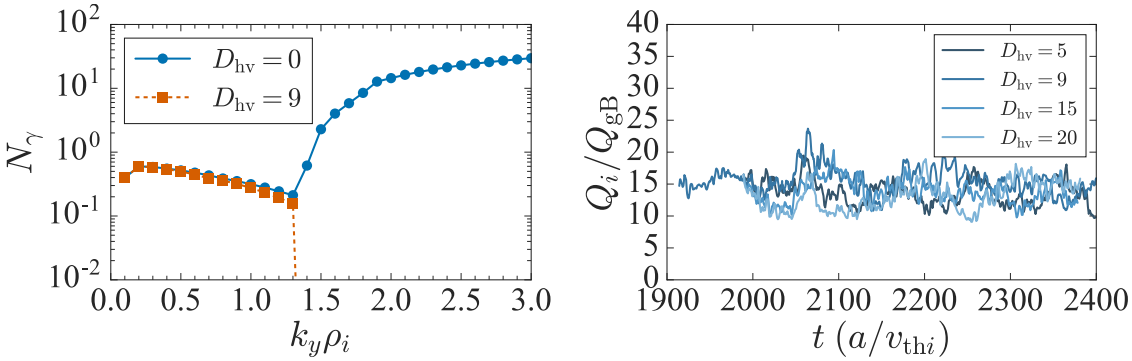

(a) (b)

Figure A.1: (a) Linear growth rate $\gamma$ as a function of $k_y\rho_i$ covering both ion and electron scales for $\kappa_T = 5.1$ and $\gamma_E = 0$. There is no clear scale separation between the ion and electron dynamics. (b) Effective linear growth rates $\gamma_{\mathrm{eff}}$ versus $k_y\rho_i$ at $k_x\rho_i = 0$ for a range of different values of $D_{\mathrm{hv}}$, calculated from (A.2). We have used $k_{y,\mathrm{max}}\rho_i = 3.1$ because this was the maximum value resolved in our nonlinear simulations.

where $D_{\mathrm{hv}}$ is a constant coefficient controlling the strength of the hyperviscosity (denoted by `d_hypervisc` in GS2), $k_\perp^2 = k_x^2 + k_y^2$, $k_{\perp,\mathrm{max}}$ is the largest perpendicular wavenumber resolved in the simulation. Hence, the effective growth rate is given by

$$\gamma_{\mathrm{eff}} = \gamma - D_{\mathrm{hv}} \frac{k_\perp^4}{k_{\perp,\mathrm{max}}^4}. \tag{A.2}$$

Figure A.1(b) shows the effective linear growth rate, calculated using (A.2) as a function of $k_y\rho_i$ for $k_x\rho_i = 0$ for a range of values of $D_{\mathrm{hv}}$. We have used $k_{y,\mathrm{max}}\rho_i \approx 3$, which was the maximum resolved wavenumber in our nonlinear simulations. The $D_{\mathrm{hv}} = 0$ curve shows the need for hyperviscosity in our nonlinear simulations: there is no clear scale separation between ion ($k_y\rho_i \sim 1$) and electron scales ($k_y\rho_i \gtrsim 2$). Therefore, a purely ion-scale nonlinear simulation would have strongly growing electron modes at the smallest simulated scales, but wouldn't resolve the electron dissipation scale at $k_y\rho_i \sim 60$. Hence, hyperviscosity provides the damping needed to run an ion-scale simulation and stop an unphysical build up of free energy at the smallest scales. In our nonlinear simulations we settle on the value $D_{\mathrm{hv}} = 9$ and prove later that it does not affect the transport properties.




(a) (b)

Figure A.2: (a) Transient-amplification factor $N_\gamma$ (at $(\kappa_T, \gamma_E) = (5.1, 0.16)$ and $k_x\rho_i = 0$) for a range of $k_y\rho_i$ identical to that in our nonlinear simulations with $D_{\rm hv} = 0$ (blue line) and $D_{\rm hv} = 9$ (red line). While ion-scale transient growth is unaffected electron-scale modes are suppressed by the hyperviscosity. (b) Ion heat flux $Q_i/Q_{\rm gB}$ as a function of time for nonlinear simulations with $(\kappa_T, \gamma_E) = (5.1, 0.16)$ with $D_{\rm hv} = 5$, 15, and 20.

In the presence of flow shear, the picture is made more complicated by the fact that the system is subcritical; however, we are still able to study the effect of hyperviscosity. Setting $\gamma_E > 0$, and calculating the transient-amplification factor $N_\gamma$, instead of $\gamma$, leads to a similar conclusion as for $\gamma_E = 0$ simulations without hyperviscosity: there is no clear maximum value of $k_y\rho_i$ that would ensure there is no growth at the smallest scales, as shown by the blue line in Figure A.2(a) (with $\gamma_E = 0.16$). The red line in Figure A.2(a) shows the effect of hyperviscosity on $N_\gamma$ [at $(\kappa_T, \gamma_E) = (5.1, 0.16)$ and $k_x\rho_i = 0$] for a value of $k_{\perp,\rm max}$ equal to that in our nonlinear simulations. We see that ion-scale transient growth is not strongly affected by the hyperviscosity while electron-scale transient growth is effectively damped (mainly due to their long transient growth time), i.e, $N_\gamma$ goes to zero. This allowed us to choose a cut-off scale for our nonlinear simulations at $k_y\rho_i \sim O(1)$ and focus our attention at ion scales while still simulating electrons via a kinetic equation and including their effect on the ions.

The key requirement when artificially removing energy from the system, as hyperviscosity does, is that the nonlinear saturated state should not depend strongly on the value of $D_{\rm hv}$. Figure A.2(b) shows four nonlinear simulations at $(\kappa_T, \gamma_E) = (5.1, 0.16)$ with different levels of hyperviscosity. The simulation at $D_{\rm hv} = 9$ was run until satura-

tion and then restarted three times with different values of $D_{\mathrm{hv}}$: $D_{\mathrm{hv}} = 5, 15$, and $20$. Figure A.2(b) shows that these level of $D_{\mathrm{hv}}$ do not affect the level of transport strongly while allowing our simulations to saturate. Based on Figure A.2(b), we have used $D_{\mathrm{hv}} = 9$ for all of our nonlinear simulations.

In conclusion, using hyperviscosity we were able to damp high wavenumber dynamics and allowed us to run ion-scale-only simulations, with a cut-off scale around $k_y \rho_i \sim 3$. As a consequence of being limited to ion scales only, our simulations will miss the effects of turbulence at electron scales, as well as possible cross-scale coupling effects between electron and ion scales. Previous realistic multiscale studies [119, 120] have shown that these effects may increase the level of turbulence via the stabilisation of zonal flows by electron scale turbulence. However, for the purposes of this work we will assume that we are capturing the majority of the physics at ion scales, and are not introducing any artificial effects through our high-wavenumber cut-off.

# Appendix B

# *Resolving the effect of flow shear*

In this appendix, we estimate the conditions that need to be satisfied in order to resolve the effect of flow shear using the results from nonlinear simulations in the absence of flow shear.

In Section 3.4.3, we showed that flow shear is implemented in GS2 by allowing the radial wavenumber $k_x$ to vary with time according to (3.42), and by "shifting" the fluctuation fields along the $k_x$ dimension. The frequency at which GS2 shifts the fluctuation fields in the $k_x$ dimension depends on the value of the radial grid spacing $\Delta k_x$, $\gamma_E$, and the poloidal wavenumber $k_y$. From (3.42), the time taken before the exact shift is $\Delta k_x/2$ (at which points GS2 shifts the fluctuation fields by $\Delta k_x$ as explained in Section 3.4.3) is

$$\tau_{\mathrm{shift}} = \frac{\Delta k_x}{2\gamma_E k_y}. \tag{B.1}$$

In order for the effect of flow shear to be considered "resolved", this shifting operation should occur at least once during the lifetime of an eddy, otherwise turbulence will interact and decorrelate as though the simulation were shearless. The turbulence decorrelation time $\tau_{\mathrm{NL}}$ is estimated from the correlation properties of turbulence via (5.10), and the condition for flow shear to be resolved is, therefore,

$$\tau_{\mathrm{shift}} \lesssim \tau_{\mathrm{NL}}. \tag{B.2}$$

To estimate the value of $\tau_{\mathrm{NL}}$ relevant to our parameter scan, we performed a series of nonlinear simulations at a range of different values of ion temperature gradient $\kappa_T$

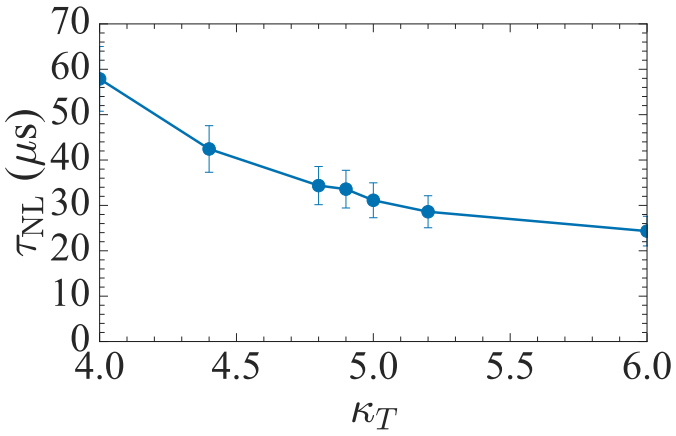



Figure B.1: Nonlinear decorrelation time $\tau_{\mathrm{NL}}$, calculated using (5.10), as a function of $\kappa_T$ for simulations with $\gamma_E = 0$.

in the absence of flow shear. The results are shown in Figure B.1, and we see that at the experimental value $\kappa_T = 5.1$, $\tau_{\mathrm{NL}} \sim 30$ $\mu$s. We now want to find the approximate value of $\gamma_E$ that ensures (B.2) is satisfied, given the value of $\tau_{\mathrm{NL}}$ above. Returning to (B.1), the radial grid spacing we employed in our nonlinear simulations was $\Delta k_x \approx 0.03$, and the most important scales in the system is $k_y \rho_i \sim 0.2$ [see Figure A.2(a)]. Using (B.1), the value of $\gamma_E$ that satisfies (B.2) is $\gamma_E \approx 0.08$, where values less than this satisfy (B.2) less well. Therefore, we have taken this to be the minimum value of flow shear for our parameter scan in this work.

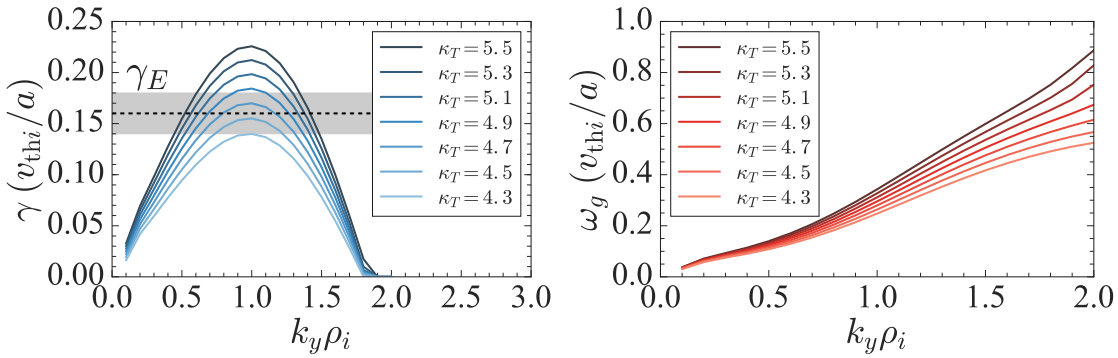
# Appendix C

# *Linear simulations with* $\gamma_E = 0$

In Section 4.3, we showed that, in the presence of flow shear, the turbulence is subcritical. This means that one cannot easily define a linear growth rate for $\gamma_E > 0$ simulations; however, it is still useful to consider the linear physics in the absence of flow shear to investigate which scales are important. Here, we look at the linear growth rates and frequencies for simulations with adiabatic and kinetic electron species.

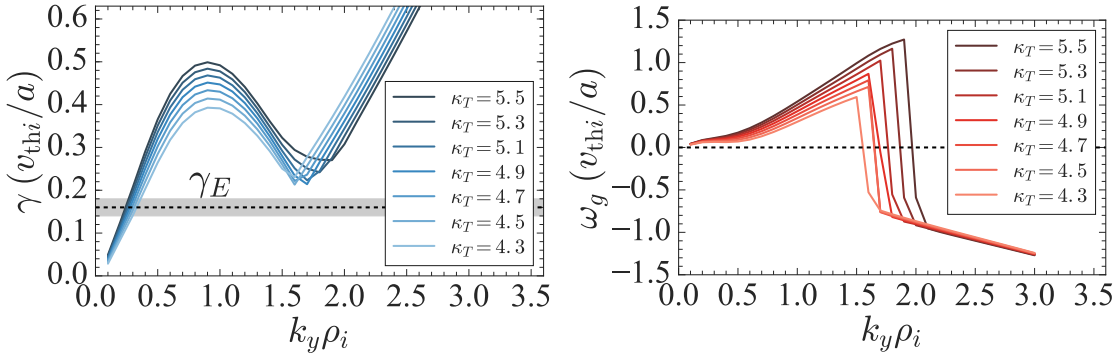
In the absence of flow shear, $\varphi$ will evolve in time according to $\varphi \sim e^{\gamma t}$, where $\gamma$ is the linear growth rate. We start by looking at $\gamma$ and real frequency $\omega_g$ versus $k_y$ for simulations with kinetic ions and adiabatic electrons for a range of ion temperature gradient length scales $\kappa_T$ as shown in Figure C.1. The dashed line indicates the experimental value of flow shear $\gamma_E = 0.16 \pm 0.02$. We see that the flow shear is comparable to the maximum linear growth rate, i.e., $\gamma_E \sim \gamma_{\max}$. Previous numerical studies with adiabatic electrons and flow shear [31] have defined the so-called "Waltz Rule", which states that ion-scale turbulence tends to be quenched when $\gamma_{\max} \sim \gamma_E$. Indeed, nonlinear simulations of our system with adiabatic electrons and flow shear show that steady-state turbulence cannot be achieved for any $\kappa_T$ within the experimental error range, in agreement with the above quenching rule.

Including a kinetic electron species, leads to much stronger linear growth as shown in Figure C.2, which again shows $\gamma$ and $\omega_g$ as a function of $k_y\rho_i$. We focus here on the dynamics at ion scales ($k_y\rho_i \sim 1$), given that the hyperviscosity we apply in our nonlinear simulations acts predominantly on the electron scales (see Appendix 3.4.4). Figure C.3




(a) (b)

Figure C.1: (a) Linear growth rate $\gamma$ and (b) real frequency $\omega_g$ versus $k_y$ for simulations with a single kinetic ion species and adiabatic electrons. For these linear simulations plots, $k_x\rho_i = 0$. The shaded region shows the experimental level of flow shear $\gamma_E = 0.16 \pm 0.02$.




(a) (b)

Figure C.2: (a) Linear growth rate $\gamma$ and (b) real frequency $\omega_g$ versus $k_y$ for simulations with a kinetic ion and electron species. For these linear simulations plots, $k_x\rho_i = 0$. The shaded region shows the experimental level of flow shear $\gamma_E = 0.16 \pm 0.02$.

shows the maximum growth rate at ion scales as a function of $\kappa_T$ with $\kappa_T = 4.8$. The horizontal dashed line indicates $\gamma_E = 0.16 \pm 0.02$ and the vertical dashed line indicates $\kappa_T = 4.8$, which was the value of $\kappa_T$ at which turbulence was quenched in our nonlinear simulations at this flow shear [see Figures 4.1 and 4.2]. We see that the maximum growth rate at ion scales is clearly much larger than $\gamma_E$, and that $\gamma_E/\gamma_{\mathrm{max}} \sim 1/3$ at $\kappa_T = 4.8$.

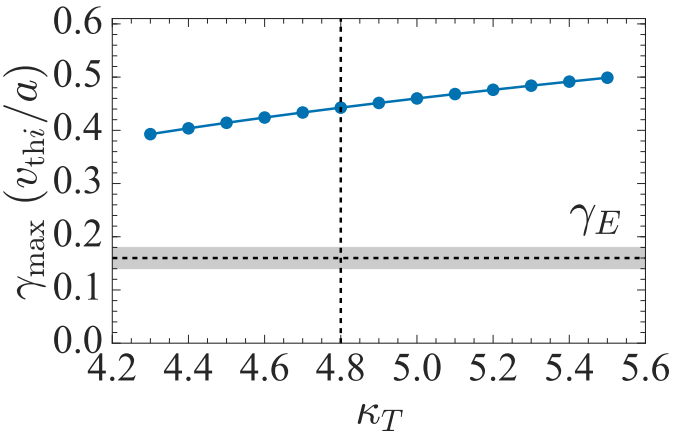



Figure C.3: Maximum linear growth rate $\gamma_{\max}$ as a function of $\kappa_T$. The dashed line and shaded area indicate $\gamma_E = 0.16 \pm 0.02$.

Previous numerical investigations with kinetic electrons investigating the quenching of turbulence with flow shear estimated that [121]: $\gamma_E/\gamma_{\max} = 0.71(\kappa/1.5)/(A/3)^{0.6}$, where $A$ aspect ratio and $\kappa$ is the flux surface elongation. For the flux surface we are considering, $A \sim 1.5$ and $\kappa = 1.46$ (see Table 3.4), giving $\gamma_E/\gamma_{\max} \sim 1$, similar to the quench condition for adiabatic electrons. We see that in our nonlinear simulations, turbulence is quenched for a much lower ratio of $\gamma_E/\gamma_{\max}$ suggesting that, for the system we are investigating, flow shear is more effective than expected at quenching ion-scale turbulence, at least compared to the estimates in [121].

# Appendix D

# *Transforming to real space and laboratory frame*

As explained in Section 3.4.1, GS2 solves the gyrokinetic equation (3.15) in curvilinear coordinates [89] in a domain known as a "flux tube", shown in Figure 3.2, that rotates with the plasma. In order to analyse the real-space structure of turbulence and compare with BES measurements, we need to transform our data from the rotating plasma frame to the laboratory frame and from flux-tube geometry to real-space geometry, i.e., from the GS2 coordinates $(x, y, \theta)$ to $(R, Z, \lambda)$ where $x$ and $y$ are the GS2 perpendicular coordinates, $\theta$ is the poloidal angle, $R$ is the major radius, $Z$ is poloidal height above the midplane of the machine, and $\lambda$ is the distance along the field line.

## D.1 Laboratory frame

GS2 simulates the plasma in a frame rotating with the plasma [see equation (3.21) and (3.22)], with toroidal rotation frequency $\omega_0$, whereas the BES diagnostic measures turbulence in the laboratory frame. In order to make realistic comparisons with BES measurements, we applied the following transformation to the GS2 distribution function to transform from the rotating to the laboratory frame [62]:

$$\left(\frac{\delta n_i}{n_i}\right)_{\text{lab}}(t, k_x, k_y, \theta) = \left(\frac{\delta n_i}{n_i}\right)_{\text{GS2}}(t, k_x, k_y, \theta)e^{-in\omega_0 t}, \tag{D.1}$$

where $(\delta n_i/n_i)_{\mathrm{GS2}}(t, k_x, k_y, \theta)$ is the fluctuating density field calculated by GS2 in the rotating frame, $(\delta n_i/n_i)_{\mathrm{lab}}(t, k_x, k_y, \theta)$ is the density field in the laboratory frame, and

$$n = k_y \rho_i \frac{\mathrm{d}\psi_N}{\mathrm{d}r} \frac{a}{\rho_i} \tag{D.2}$$

is the toroidal mode number of a given $k_y$ mode, $\psi_N$ is the normalised poloidal magnetic flux, $r = D/2a$ is the Miller [79] radial coordinate, $D$ is the diameter of the flux surface, $a$ is half of the diameter of the last closed flux surface (LCFS), and $\rho_i$ is the ion gyroradius.

## D.2 Radial domain size

Here, we calculate the radial domain size $L_R$ at the outboard midplane from the radial domain size in GS2 coordinates $L_x$. We start by noting that gradients across the GS2 domain are held constant, meaning that

$$R'(\theta = 0) = \frac{1}{a}\frac{\mathrm{d}R(\theta = 0)}{\mathrm{d}r} = \frac{1}{a}\frac{\Delta R(\theta = 0)}{\Delta r}, \tag{D.3}$$

where $R$ is the major radius, $R'(\theta)$ is the derivative of $R$ with respect to the poloidal angle $\theta$, and $\Delta R(\theta = 0) \equiv L_R$ is the radial domain size. We calculate $\Delta r$ from the local GS2 coordinate $x$ as follows. Using the Taylor expansion $r \approx r_0 + (\psi_N - \psi_{0N})\ \mathrm{d}r/\mathrm{d}\psi_N \Big|_{r_0}$ and substituting into (3.28) we get

$$x = (r - r_0)\frac{q_0}{r_0}\frac{\mathrm{d}\psi_N}{\mathrm{d}r}\frac{a}{\rho_i}, \tag{D.4}$$

where $r_0 = 0.8$ is the location of the flux surface we are investigating, and $q_0$ is the safety factor at $r = 0.8$. The extent of the radial domain in the coordinate $x$ is then

$$\Delta x = \Delta r \frac{q}{r_0}\frac{\mathrm{d}\psi_N}{\mathrm{d}r}\frac{a}{\rho_i}. \tag{D.5}$$

Using the following values from our simulations $\Delta x = 2\pi/k_{x,\mathrm{min}}\rho_i \approx 200\rho_i$, where $k_{x,\mathrm{min}}$ is the minimum resolved $k_x$ in our nonlinear simulations, $(\mathrm{d}\psi_N/\mathrm{d}r)^{-1} = 1.44$, and from the experiment [see Tables 2.2 and 3.4] $a = 0.58$ m, $\rho_i = 6.08 \times 10^{-3}$ m, $q_0 = 2.31$, we calculate $\Delta r$ from equation (D.5) and substitute into equation (D.3) to find $\Delta R(\theta = 0) \equiv L_R \approx 65\rho_i \approx 0.4$ m. We note that while $x$ is a local coordinate and $R$ is a physical coordinate our simulations only describe the turbulence at $r = 0.8$. Hence, our results are only comparable to experimental results at this radius.

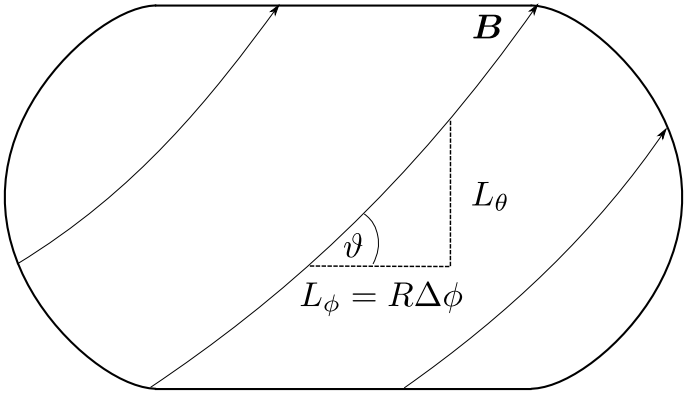



Figure D.1: Side view sketch of the MAST geometry shown in Figure 3.2. The magnetic field's pitch-angle, $\vartheta$ ($\approx 0.6$), relates the toroidal extent of the GS2 domain, $L_\phi$, with the poloidal extent, $L_\theta$, through $\tan\vartheta = L_\theta/L_\phi$.

## D.3 Poloidal domain size

To calculate the poloidal domain size $L_Z$, we start by noting that, the GS2 grid points lie on $(\phi, \psi)$ planes at constant values of $\theta$. Therefore, at $\theta = 0$, GS2 simulates turbulence on a radial-toroidal plane. The extent of the GS2 domain in toroidal angle $\phi$ is [89]

$$\Delta\phi = \frac{2\pi}{n_0}, \tag{D.6}$$

where

$$n_0 = k_{y,\min}\rho_i \frac{\mathrm{d}\psi_N}{\mathrm{d}r}\frac{a}{\rho_i} \tag{D.7}$$

is the minimum toroidal mode number simulated and $k_{y,\min}\rho_i$ is the smallest resolved $k_y$ mode in our nonlinear simulations. The toroidal extent of the domain is therefore given by $L_\phi = R\Delta\phi$, where $R$ is the major radius of the flux surface at the outboard midplane. We can relate $L_\phi$ to the poloidal extent of the GS2 domain, $L_\theta$, via the relation $\tan\vartheta = L_\theta/L_\phi$, where $\vartheta$ ($\approx 0.6$) is the pitch-angle of the magnetic field, as shown in Figure D.1, for the flux surface $r = 0.8$ at the outboard midplane. In our nonlinear simulations, $k_{y,\min}\rho_i = 0.1$, giving $n_0 \approx 7$ using (D.7) and $L_\phi \approx 1.2$ m. Using the above relations we find that the poloidal projection of the plane at $\theta = 0$ is $L_\theta \approx 134\rho_i \approx 0.81$ m.

Using the results from this section and Section D.2, we can transform our density fluctuation fields at the outboard midplane to a radial-poloidal plane similar to the BES

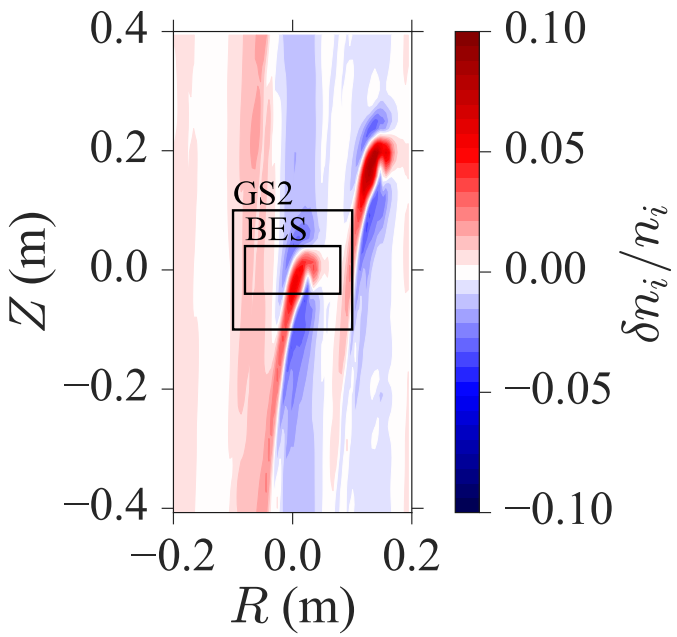



Figure D.2: Density-fluctuation field $\delta n_i/n_i$ for the same near-marginal shown in Figure 4.10(a) for the equilibrium parameters $(\kappa_T, \gamma_E) = (4.8, 0.16)$ as a function $R$ and $Z$. The indicated domains are those used for the correlation analysis of raw GS2 density fluctuations (GS2) and the approximate size of the BES viewing window (BES).

measurement window. For example, Figure D.2 shows the same plot as in Figure 4.10(a) at $\theta = 0$ in terms of the real-space poloidal coordinates $R$ and $Z$. Also indicated in Figure D.2 are the domains used for the correlation analysis of BES data and raw GS2 data, as used in Sections 5.3 and 5.5, respectively.

## D.4 Parallel coordinate and domain size

Finally, we calculate the parallel distance along the magnetic field line at the centre of our flux tube. This procedure is non-trivial for a general geometry because a uniform grid in $\theta$ does not map to a uniform spatial grid along the field line as it would have done for circular flux surfaces. For our D-shaped geometry we want to find $\lambda(\theta)$, the distance along the field line parametrised by the poloidal angle $\theta$. The differential arc length of a

line element along the field line in terms of $(R, Z, \phi)$ is

$$d\lambda^2 = dR^2 + dZ^2 + (Rd\phi)^2, \tag{D.8}$$

where $R = R(\theta)$ and $Z = Z(\theta)$ are the coordinates of the magnetic field line at the centre of the flux tube. We can differentiate with respect to $\theta$ and integrate to get the arc length as a function of $\theta$:

$$\lambda(\theta) = \int_0^\theta d\theta' \sqrt{\left(\frac{\mathrm{d}R}{\mathrm{d}\theta'}\right)^2 + \left(\frac{\mathrm{d}Z}{\mathrm{d}\theta'}\right)^2 + \left(R\frac{\mathrm{d}\phi}{\mathrm{d}\theta'}\right)^2}. \tag{D.9}$$

The quantities $R(\theta)$, $Z(\theta)$, $\mathrm{d}\phi/\mathrm{d}\theta$ are obtained from GS2 and we then calculate their numerical derivatives with respect to $\theta$, and then the integral (D.9) to determine $\lambda(\theta)$. With the knowledge of the real-space parallel grid, we can calculate correlation lengths in the parallel direction.

# Appendix E

# *Synthetic correlation properties without the "spike filter"*

A key step in the analysis of experimental data involves the removal of high-energy radiation (e.g., neutron, gamma ray, or hard X-ray) impinging on the BES detector. This radiation manifests itself as delta-function-like spikes in time, typically only on a single BES channel. These are removed via a numerical "spike filter" [55, 118], which was included in the main analysis for consistency with experimental analysis. Here, we show the results of a correlation analysis of GS2 density fluctuations with the synthetic diagnostic applied, but without this "spike filter". Figure E.1 shows the correlation results for parameter values within the experimental uncertainty: the radial correlation length $l_R^{\mathrm{NS}}$ [Figure E.1(a)], the poloidal correlation length $l_Z^{\mathrm{NS}}$ [Figure E.1(b)], the correlation time $\tau_c^{\mathrm{NS}}$ [Figure E.1(c)], the RMS density fluctuation $(\delta n_i/n_i)_{\mathrm{rms}}^{\mathrm{NS}}$ [Figure E.1(d)].

Comparing these results to the results in Section 5.4 with the "spike filter", we see that only the poloidal correlation length is affected: $l_Z^{\mathrm{NS}}$ is several centimetres lower with the "spike filter" compared to cases without it. We found that in some cases, fast-moving structures in the poloidal direction (especially the long-lived structures found in our near-marginal simulations) were removed by the "spike filter" and, therefore, would not affect to the poloidal correlation function, resulting in a drop in $l_Z^{\mathrm{NS}}$. In particular, Figure E.1(b) shows that $l_Z^{\mathrm{NS}}$ increased significantly in near-marginal simulations compared to the results with the "spike filter", suggesting that the coherent structures were

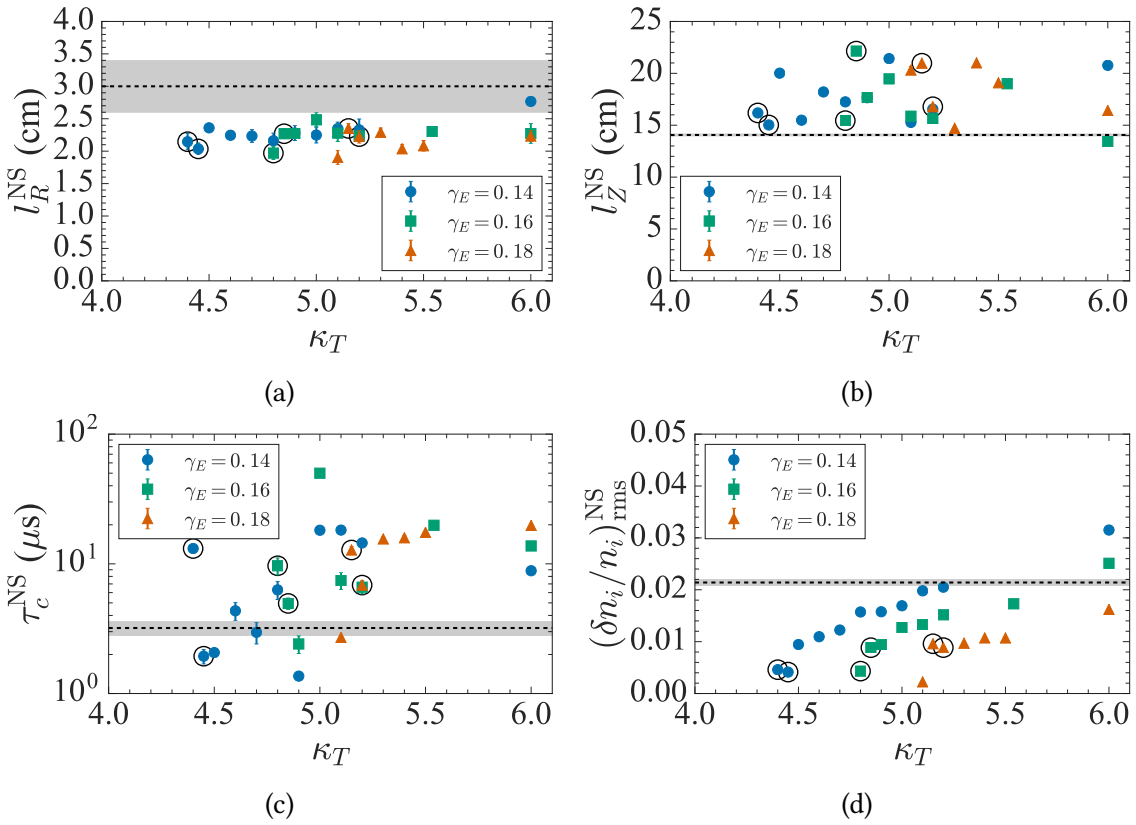



Figure E.1: Correlation-analysis results calculated from the analysis of GS2 fluctuation data (within the region of experimental uncertainty) after applying the synthetic diagnostic, but without the spike filter normally applied to experimental data: (a) radial correlation length $l_R^{\mathrm{NS}}$, (b) poloidal correlation length $l_Z^{\mathrm{NS}}$, (c) correlation time $\tau_c^{\mathrm{NS}}$, and (d) RMS density fluctuation level $(\delta n_i/n_i)_{\mathrm{rms}}^{\mathrm{NS}}$. The simulations that matched the experimental heat flux are circled. The quantities plotted here are discussed in Section 5.2.

no longer removed by the "spike filter". This observation may assist future attempts to observe experimentally the coherent structures predicted by our simulations.

# Appendix F

# *Example GS2 input file*

The following is an example GS2 input file used for this study (see `http://gyrokinetics.sourceforge.net` on how to run the code with these settings). A description of each of these variables can be found at `http://gyrokinetics.sourceforge.net/wiki/index.php/Gs2_Input_Parameters`.

```
! General parameters
&parameters
     beta = 0.0047310768
     zeff = 1.5899834
/

&kt_grids_knobs
     grid_option = "box"
/

! Resolution parameters
&kt_grids_box_parameters
     nx = 128
     ny = 96
     jtwist = 80
     y0 = 10.0
     x0 = 10.0
/

! Geometric parameters
&theta_grid_parameters
     ntheta = 20
     nperiod = 1
     shat = 3.9955695
     rhoc = 0.7966436
     qinp = 2.31493
```

```
     akappa = 1.45734
     akappri = 0.44877291
     tri = 0.205939
     tripri = 0.46296135
     shift = -0.30708938
     rmaj = 1.4891066
     r_geo = 1.6438144
/

&theta_grid_knobs
    equilibrium_option = "eik"
/

&theta_grid_eik_knobs
     itor = 1
     iflux = 0
     irho = 2
     local_eq = .true.
     bishop = 4
     s_hat_input = 3.9955695
     beta_prime_input = -0.1212404
     delrho = 0.001
/

! Velocity space grid parameters
&le_grids_knobs
     ngauss = 8
     negrid = 16
/

&dist_fn_knobs
     gridfac = 1.0
     boundary_option = "linked"
     g_exb = 0.16
     apfac = 1.0
     driftknob = 1.0
     opt_init_bc = .true.
     opt_source = .true.
/

&fields_knobs
     field_option = "local"
     field_subgath = .true.
     response_dir = "response"
     do_smart_update = .true.
     field_local_allreduce = .true.
     field_local_allreduce_sub = .true.
/

! Time parameters
&knobs
     fphi = 1.0
     faperp = 0.0
```

```
    delt = 0.01
    nstep = 100000
    avail_cpu_time = 21600
    margin_cpu_time = 600
/

&reinit_knobs
    delt_adj = 2.0
    delt_minimum = 1.0e-06
    delt_cushion = 10
/

&layouts_knobs
    layout = "xyles"
    unbalanced_xxf = .true.
    max_unbalanced_xxf = 0.5
    unbalanced_yxf = .true.
    max_unbalanced_yxf = 0.5
    intmom_sub = .true.
    intspec_sub = .true.
/

&collisions_knobs
    collision_model = "default"
/

&hyper_knobs
    hyper_option = "visc_only"
    const_amp = .true.
    d_hypervisc = 9
/

&nonlinear_terms_knobs
    nonlinear_mode = "on"
    flow_mode = "off"
    cfl = 0.5
/

&species_knobs
    nspec = 2
/

&species_parameters_1
    z = 1.0
    mass = 1.0
    dens = 1.0
    temp = 1.0
    tprim = 5.1
    fprim = 2.64278
    uprim = 0.0
    vnewk = 0.02098588
    type = "ion"
/
```

```
&dist_fn_species_knobs_1
     fexpr = 0.48
     bakdif = 0.05
/

&species_parameters_2
     z = -1.0
     mass = 0.0002723311
     dens = 1.0
     temp = 1.091722
     tprim = 5.773614
     fprim = 2.64278
     uprim = 0.0
     vnewk = 0.5900574
     type = "electron"
/

&dist_fn_species_knobs_2
     fexpr = 0.48
     bakdif = 0.05
/

! Initial conditions
&init_g_knobs
     phiinit = 1.0
     restart_file = "gs2.nc"
     ginit_option = "noise"
     restart_dir = "nc"
/

! Diagnostics
&gs2_diagnostics_knobs
     write_verr = .true.
     write_avg_moments = .true.
     write_eigenfunc = .true.
     write_final_fields = .true.
     write_final_moments = .true.
     nsave = 500
     nwrite = 100
     navg = 10
     omegatol = -0.001
     omegatinst = 500.0
     save_for_restart = .true.
     write_cross_phase = .true.
/
```

# *Bibliography*


[1] F. L. Hinton and R. D. Hazeltine, "Theory of plasma transport in toroidal confinement systems", Rev. Mod. Phys. **48**, 239 (1976).

[2] F. L. Hinton and S. K. Wong, "Neoclassical ion transport in rotating axisymmetric plasmas", Phys. Fluids **28**, 3082 (1985).

[3] P. J. Catto, I. B. Bernstein, and M. Tessarotto, "Ion transport in toroidally rotating tokamak plasmas", Phys. Fluids **30**, 2784 (1987).

[4] H. Sugama and W. Horton, "Neoclassical electron and ion transport in toroidally rotating plasmas", Phys. Plasmas **4**, 2215 (1997).

[5] P. Helander and D. J. Sigmar, *Collisional transport in magnetized plasmas* (Cambridge University Press, 2002).

[6] B. Coppi, M. N. Rosenbluth, and R. Z. Sagdeev, "Instabilities due to temperature gradients in complex magnetic field configurations", Phys. Fluids **10**, 582 (1967).

[7] P. J. Catto, "Parallel velocity shear instabilities in an inhomogeneous plasma with a sheared magnetic field", Phys. Fluids **16**, 1719 (1973).

[8] S. C. Cowley, R. M. Kulsrud, and R. Sudan, "Considerations of ion-temperature-gradient-driven turbulence", Phys. Fluids B **3**, 2767 (1991).

[9] J. W. Connor and H. R. Wilson, "Survey of theories of anomalous transport", Plasma Phys. Control. Fusion **36**, 719 (1994).

[10] F. Jenko, W. Dorland, M. Kotschenreuther, and B. N. Rogers, "Electron temperature gradient driven turbulence", Phys. Plasmas **7**, 1904 (2000).

[11] W. Dorland, F. Jenko, M. Kotschenreuther, and B. N. Rogers, "Electron temperature gradient turbulence", Phys. Rev. Lett. **85**, 5579 (2000).

[12] T. Dannert and F. Jenko, "Gyrokinetic simulation of collisionless trapped-electron mode turbulence", Phys. Plasmas **12**, 1 (2005).

[13] G. R. Tynan, A. Fujisawa, and G. R. McKee, "A review of experimental drift turbulence studies", Plasma Phys. Control. Fusion **51**, 113001 (2009).

[14] R. J. Hawryluk, S. H. Batha, W. Blanchard, M. Beer, M. G. Bell, R. E. Bell, H. L. Berk, S. Bernabei, M. Bitter, B. N. Breizman, et al., "Fusion plasma experiments on TFTR: A 20 year retrospective", Phys. Plasmas **5**, 1577 (1998).

[15] E. Lazarus, G. Navratil, C. M. Greenfield, E. Strait, M. E. Austin, K. H. Burrell, T. Casper, D. R. Baker, J. C. DeBoo, E. J. Doyle, et al., "Higher fusion power gain with current and pressure profile control in strongly shaped DIII-D tokamak plasmas", Phys. Rev. Lett. **77**, 2714 (1996).

[16] R. J. Akers, J. W. Ahn, G. Y. Antar, L. C. Appel, D. Applegate, C. Brickley, C. Bunting, P. G. Carolan, C. D. Challis, N. J. Conway, et al., "Transport and confinement in the Mega Ampère Spherical Tokamak (MAST) plasma", Plasma Phys. Control. Fusion **45**, A175 (2003).

[17] P. Mantica, D. Strintzi, T. Tala, C. Giroud, T. Johnson, H. Leggate, E. Lerche, T. Loarer, A. G. Peeters, A. Salmi, et al., "Experimental study of the ion critical-gradient length and stiffness level and the impact of rotation in the JET Tokamak", Phys. Rev. Lett. **102**, 1 (2009).

[18] D. R. Baker, C. M. Greenfield, K. H. Burrell, J. C. DeBoo, E. J. Doyle, R. J. Groebner, T. C. Luce, C. C. Petty, B. W. Stallard, D. M. Thomas, et al., "Thermal diffusivities in DIII-D show evidence of critical gradients", Phys. Plasmas **8**, 4128 (2001).

[19] G. Tardini, A. G. Peeters, G. V. Pereverzev, F. Ryter, J. Stober, and ASDEX Upgrade Team, "Comparison of theory based transport models with ASDEX upgrade data", Nucl. Fusion **42**, 258 (2002).

[20] P. Mantica, C. Angioni, C. Challis, G. Colyer, L. Frassinetti, N. Hawkes, T. Johnson, M. Tsalas, P. C. DeVries, J. Weiland, et al., "A key to improved ion core con-

finement in the JET tokamak: ion stiffness mitigation due to combined plasma rotation and low magnetic shear", Phys. Rev. Lett. **107**, 135004 (2011).

[21] Y.-c. Ghim, A. R. Field, A. A. Schekochihin, E. G. Highcock, C. Michael, and the MAST Team, "Local dependence of ion temperature gradient on magnetic configuration, rotational shear and turbulent heat flux in MAST", Nucl. Fusion **54**, 6 (2014).

[22] W. Horton and R. D. Estes, "Fluid simulation of ion pressure gradient driven drift modes", Plasma Phys. **22**, 663 (1980).

[23] R. E. Waltz, "Three-dimensional global numerical simulation of ion temperature gradient mode turbulence", Phys. Fluids **31**, 1962 (1988).

[24] M. Kotschenreuther, W. Dorland, M. A. Beer, and G. W. Hammett, "Quantitative predictions of tokamak energy confinement from first-principles simulations with kinetic effects", Phys. Plasmas **2**, 2381 (1995).

[25] A. M. Dimits, T. J. Williams, J. A. Byers, and B. I. Cohen, "Scalings of ion-temperature-gradient-driven anomalous transport in tokamaks", Phys. Rev. Lett. **77**, 71 (1996).

[26] E. G. Highcock, M. Barnes, A. A. Schekochihin, F. I. Parra, C. M. Roach, and S. C. Cowley, "Transport bifurcation in a rotating tokamak plasma", Phys. Rev. Lett. **105**, 215003 (2010).

[27] M. Barnes, F. I. Parra, E. G. Highcock, A. A. Schekochihin, S. C. Cowley, and C. M. Roach, "Turbulent transport in tokamak plasmas with rotational shear", Phys. Rev. Lett. **106**, 175004 (2011).

[28] C. P. Ritz, H. Lin, T. L. Rhodes, and A. J. Wootton, "Evidence for confinement improvement by velocity-shear suppression of edge turbulence", Phys. Rev. Lett. **65**, 2543 (1990).

[29] K. H. Burrell, "Effects of ExB velocity shear and magnetic shear on turbulence and transport in magnetic confinement devices", Phys. Plasmas **4**, 1499 (1997).

[30] A. R. Field, C. Michael, R. Akers, J. Candy, G. Colyer, W. Guttenfelder, Y.-c. Ghim, C. M. Roach, and S. Saarelma, "Plasma rotation and transport in MAST spherical tokamak", Nucl. Fusion **51**, 063006 (2011).

[31] R. E. Waltz, G. D. Kerbel, and J. Milovich, "Toroidal gyro-Landau fluid model turbulence simulations in a nonlinear ballooning mode representation with radial modes", Phys. Plasmas **1**, 2229 (1994).

[32] R. E. Waltz, G. M. Staebler, W. Dorland, G. W. Hammett, M. Kotschenreuther, and J. A. Konings, "A gyro-Landau-fluid transport model", Phys. Plasmas **4**, 2482 (1997).

[33] J. E. Kinsey, R. E. Waltz, and J. Candy, "Nonlinear gyrokinetic turbulence simulations of ExB shear quenching of transport", Phys. Plasmas **12**, 062302 (2005).

[34] Y. Camenen, A. G. Peeters, C. Angioni, F. J. Casson, W. A. Hornsby, A. P. Snodin, and D. Strintzi, "Impact of the background toroidal rotation on particle and heat turbulent transport in tokamak plasmas", Phys. Plasmas **16**, 012503 (2009).

[35] C. M. Roach, I. G. Abel, R. J. Akers, W. Arter, M. Barnes, Y. Camenen, F. J. Casson, G. Colyer, J. Connor, S. C. Cowley, et al., "Gyrokinetic simulations of spherical tokamaks", Plasma Phys. Control. Fusion **51**, 124020 (2009).

[36] S. L. Newton, S. C. Cowley, and N. F. Loureiro, "Understanding the effect of sheared flow on microinstabilities", Plasma Phys. Control. Fusion **52**, 125001 (2010).

[37] E. G. Highcock, M. Barnes, F. I. Parra, A. A. Schekochihin, C. M. Roach, and S. C. Cowley, "Transport bifurcation induced by sheared toroidal flow in tokamak plasmas", Phys. Plasmas **18**, 102304 (2011).

[38] A. A. Schekochihin, E. G. Highcock, and S. C. Cowley, "Subcritical fluctuations and suppression of turbulence in differentially rotating gyrokinetic plasmas", Plasma Phys. Control. Fusion **54**, 055011 (2012).

[39] M. Landreman, G. G. Plunk, and W. D. Dorland, "Generalized universal instability: transient linear amplification and subcritical turbulence", J. Plasma Phys. **81**, 905810501 (2015).

[40] O. Reynolds, "An experimental investigation of the circumstances which determine whether the motion of water shall be direct or sinuous, and of the law of resistance in parallel channels", Philos. T. Roy. Soc. A **174**, 935 (1883).

[41] H. Salwen, F. W. Cotton, and C. E. Grosch, "Linear stability of Poiseuille flow in a circular pipe", J. Fluid Mech. **98**, 273 (1980).

[42] L. N. Trefethen, A. E. Trefethen, S. C. Reddy, and T. A. Driscoll, "Hydrodynamic stability without eigenvalues", Science **261**, 578 (1993).

[43] R. R. Kerswell, "Recent progress in understanding the transition to turbulence in a pipe", Nonlinearity **18**, R17 (2005).

[44] K. Avila, D. Moxey, A. de Lozar, M. Avila, D. Barkley, and B. Hof, "The onset of turbulence in pipe flow", Science **333**, 192 (2011).

[45] D. Barkley, B. Song, V. Mukund, G. Lemoult, M. Avila, and B. Hof, "The rise of fully turbulent flow", Nature **526**, 550 (2015).

[46] A. A. Schekochihin, S. C. Cowley, W. D. Dorland, G. W. Hammett, G. G. Howes, E. Quataert, and T. Tatsuno, "Astrophysical gyrokinetics: kinetic and fluid turbulent cascades in magnetized weakly collisional plasmas", **310**, 65 (2007).

[47] E. A. Frieman and L. Chen, "Nonlinear gyrokinetic equations for low-frequency electromagnetic waves in general plasma equilibria", Phys. Fluids **25**, 502 (1982).

[48] H. Sugama and W. Horton, "Nonlinear electromagnetic gyrokinetic equation for plasmas with large mean flows", Phys. Plasmas **5**, 2560 (1998).

[49] I. G. Abel, G. G. Plunk, E. Wang, M. Barnes, S. C. Cowley, W. D. Dorland, and A. A. Schekochihin, "Multiscale gyrokinetics for rotating tokamak plasmas: fluctuations, transport and energy flows", Rep. Prog. Phys. **76**, 105 (2013).

[50] M. Kotschenreuther, G. Rewoldt, and W. M. Tang, "Comparison of initial value and eigenvalue codes for kinetic toroidal plasma instabilities", Comput. Phys. Commun. **88**, 128 (1995).

[51] T. Görler, X. Lapillonne, S. Brunner, T. Dannert, F. Jenko, F. Merz, and D. Told, "The global version of the gyrokinetic turbulence code GENE", J. Comput. Phys. **230**, 7053 (2011).

[52] J. Candy and R. E. Waltz, "An Eulerian gyrokinetic-Maxwell solver", J. Comput. Phys. **186**, 545 (2003).

[53] G. R. McKee, C. Fenzi, R. J. Fonck, and M. Jakubowski, "Turbulence imaging and applications using beam emission spectroscopy on DIII-D (invited)", Rev. Sci. Instrum. **74**, 2014 (2003).

[54] A. R. Field, D. Dunai, N. J. Conway, S. Zoletnik, and J. Sárközi, "Beam emission spectroscopy for density turbulence measurements on the MAST spherical tokamak.", Rev. Sci. Instrum. **80**, 073503 (2009).

[55] A. R. Field, D. Dunai, R. Gaffka, Y.-c. Ghim, I. Kiss, B. Mészáros, T. Krizsanóczi, S. Shibaev, and S. Zoletnik, "Beam emission spectroscopy turbulence imaging system for the MAST spherical tokamak", Rev. Sci. Instrum. **83**, 013508 (2012).

[56] D. R. Smith, H. Feder, R. Feder, R. J. Fonck, G. Labik, G. R. McKee, N. Schoenbeck, B. C. Stratton, I. Uzun-Kaymak, and G. Winz, "Overview of the beam emission spectroscopy diagnostic system on the National Spherical Torus Experiment", Rev. Sci. Instrum. **81**, 10D717 (2010).

[57] P. Hennequin, C. Honoré, A. Truc, A. Quéméneur, C. Fenzi-Bonizec, C. Bourdelle, X. Garbet, G. T. Hoang, and the Tore Supra Team, "Fluctuation spectra and velocity profile from Doppler backscattering on Tore Supra", Nucl. Fusion **46**, S771 (2006).

[58] J. C. Hillesheim, C. Holland, L. Schmitz, S. Kubota, T. L. Rhodes, and T. A. Carter, "2D full wave modeling for a synthetic Doppler backscattering diagnostic", Rev. Sci. Instrum. **83**, 10E331 (2012).

[59] J. C. Hillesheim, N. A. Crocker, W. A. Peebles, H. Meyer, A. Meakins, A. R. Field, D. Dunai, M. Carr, and N. Hawkes, "Doppler backscattering for spherical tokamaks and measurement of high-k density fluctuation wavenumber spectrum in MAST", Nucl. Fusion **55**, 073024 (2015).

[60] E. Mazzucato, D. R. Smith, R. Bell, S. M. Kaye, J. Hosea, B. LeBlanc, J. Wilson, P. Ryan, C. Domier, N. C. Luhmann, et al., "Short-scale turbulent fluctuations

driven by the electron-temperature gradient in the National Spherical Torus Experiment", Phys. Rev. Lett. **101**, 075001 (2008).

[61] A. E. White, L. Schmitz, W. A. Peebles, T. A. Carter, T. L. Rhodes, E. J. Doyle, P. A. Gourdain, J. C. Hillesheim, G. Wang, C. Holland, et al., "A correlation electron cyclotron emission diagnostic and the importance of multifield fluctuation measurements for testing nonlinear gyrokinetic turbulence simulations", Rev. Sci. Instrum. **79**, 103505 (2008).

[62] C. Holland, A. E. White, G. R. McKee, M. W. Shafer, J. Candy, R. E. Waltz, L. Schmitz, and G. R. Tynan, "Implementation and application of two synthetic diagnostics for validating simulations of core tokamak turbulence", Phys. Plasmas **16**, 052301 (2009).

[63] M. W. Shafer, R. J. Fonck, G. R. McKee, C. Holland, A. E. White, and D. J. Schlossberg, "2D properties of core turbulence on DIII-D and comparison to gyrokinetic simulations", Phys. Plasmas **19**, 032504 (2012).

[64] Y.-c. Ghim, A. R. Field, D. Dunai, S. Zoletnik, L. Bardóczi, and A. A. Schekochihin, "Measurement and physical interpretation of the mean motion of turbulent density patterns detected by the beam emission spectroscopy system on the Mega Amp Spherical Tokamak", Plasma Phys. Control. Fusion **54**, 095012 (2012).

[65] A. R. Field, D. Dunai, Y.-c. Ghim, P. Hill, B. F. McMillan, C. M. Roach, S. Saarelma, A. A. Schekochihin, and S. Zoletnik, "Comparison of BES measurements of ion-scale turbulence with direct gyro-kinetic simulations of MAST L-mode plasmas", Plasma Phys. Control. Fusion **56**, 025012 (2014).

[66] M. F. J. Fox, A. R. Field, F. van Wyk, Y.-c. Ghim, and A. A. Schekochihin, "Experimental determination of the correlation properties of plasma turbulence using 2D BES systems", Plasma Phys. Control. Fusion **59**, 044008 (2017).

[67] M. Barnes, F. I. Parra, and A. A. Schekochihin, "Critically balanced ion temperature gradient turbulence in fusion plasmas", Phys. Rev. Lett. **107**, 115003 (2011).

[68] R. D. Durst, R. J. Fonck, G. Cosby, H. Evensen, and S. F. Paul, "Density fluctuation measurements via beam emission spectroscopy", Rev. Sci. Instrum. **63**, 4907 (1992).

[69] Y.-c. Ghim, A. A. Schekochihin, A. R. Field, I. G. Abel, M. Barnes, G. Colyer, S. C. Cowley, F. I. Parra, D. Dunai, and S. Zoletnik, "Experimental signatures of critically balanced turbulence in MAST", Phys. Rev. Lett. **110**, 145002 (2013).

[70] A. C. Darke, M. Cox, J. R. Harbar, J. H. Hay, J. B. Hicks, J. W. Hill, D. Hurford, J. S. Mckenzie, A. W. Morris, M. P. S. Nightingale, et al., "The Mega Amp Spherical Tokamak", Proc. 18th symp. fusion technol. (1994), p. 799.

[71] A. W. Morris, "MAST: results and upgrade activities", IEEE Trans. Plasma Sci. **40**, 682 (2012).

[72] M. Ono, S. M. Kaye, Y.-K. M. Peng, G. Barnes, W. Blanchard, M. D. Carter, J. Chrzanowski, L. Dudek, R. Ewig, D. Gates, et al., "Exploration of spherical torus physics in the NSTX device", Nucl. Fusion **40**, 557 (2000).

[73] J. Menard, S. Gerhardt, M. Bell, J. Bialek, A. Brooks, J. Canik, J. Chrzanowski, M. Denault, L. Dudek, D. Gates, et al., "Overview of the physics and engineering design of NSTX upgrade", Nucl. Fusion **52**, 083015 (2012).

[74] Y.-K. M. Peng, "The physics of spherical torus plasmas", Phys. Plasmas **7**, 1681 (2000).

[75] A. Sykes, R. Akers, L. Appel, P. G. Carolan, N. J. Conway, M. Cox, A. R. Field, D. A. Gates, S. Gee, M. Gryaznevich, et al., "High-beta performance of the START spherical tokamak", Plasma Phys. Control. Fusion **39**, B247 (1997).

[76] G. F. Counsell, J.-W. Ahn, R. Akers, E. Arends, R. Buttery, A. R. Field, M. Gryaznevich, P. Helander, A. Kirk, H. Meyer, et al., "Confinement and exhaust in the Mega Ampere Spherical Tokamak", Plasma Phys. Control. Fusion **44**, B23 (2002).

[77] S. M. Kaye, F. M. Levinton, D. Stutman, K. Tritz, H. Yuh, M. G. Bell, R. E. Bell, C. W. Domier, D. Gates, W. Horton, et al., "Confinement and local transport in the National Spherical Torus Experiment (NSTX)", Nucl. Fusion **47**, 499 (2007).

[78] M. Valovič, R. Akers, G. Cunningham, L. Garzotti, B. Lloyd, D. Muir, A. Patel, D. Taylor, M. Turnyanskiy, and M. Walsh, "Scaling of H-mode energy confinement with Ip and BT in the MAST spherical tokamak", Nucl. Fusion **49**, 075016 (2009).

[79] R. L. Miller, M. S. Chu, J. M. Greene, Y. R. Lin-Liu, and R. E. Waltz, "Noncircular, finite aspect ratio, local equilibrium model", Phys. Plasmas **5**, 973 (1998).

[80] N. J. Conway, P. G. Carolan, J. McCone, M. J. Walsh, and M. Wisse, "High-throughput charge exchange recombination spectroscopy system on MAST", Rev. Sci. Instrum. **77**, 10F131 (2006).

[81] R. Scannell, M. J. Walsh, M. R. Dunstan, J. Figueiredo, G. Naylor, T. O'Gorman, S. Shibaev, K. J. Gibson, and H. Wilson, "A 130 point Nd:YAG Thomson scattering diagnostic on MAST", Rev. Sci. Instrum. **81**, 10D520 (2010).

[82] L. L. Lao, H. S. John, R. D. Stambaugh, A. G. Kellman, and W. Pfeiffer, "Reconstruction of current profile parameters and plasma shapes in tokamaks", Nucl. Fusion **25**, 1611 (1985).

[83] R. J. Hawryluk, "An empirical approach to tokamak transport", Phys. plasmas close to thermonucl. cond. Vol. 1, edited by B. Coppi (1981), pp. 19–46.

[84] E. G. Highcock, "The zero turbulence manifold in fusion plasmas", PhD thesis (2012).

[85] B. F. McMillan, X. Lapillonne, S. Brunner, L. Villard, S. Jolliet, A. Bottino, T. Görler, and F. Jenko, "System Size Effects on Gyrokinetic Turbulence", Phys. Rev. Lett. **105**, 155001 (2010).

[86] I. G. Abel, M. Barnes, S. C. Cowley, W. D. Dorland, and A. A. Schekochihin, "Linearized model Fokker–Planck collision operators for gyrokinetic simulations. I. Theory", Phys. Plasmas **15**, 122509 (2008).

[87] M. Barnes, I. G. Abel, W. Dorland, D. R. Ernst, G. W. Hammett, P. Ricci, B. N. Rogers, A. A. Schekochihin, and T. Tatsuno, "Linearized model Fokker–Planck collision operators for gyrokinetic simulations. II. Numerical implementation and tests", Phys. Plasmas **16**, 072107 (2009).

[88] J. Ball, F. I. Parra, M. Barnes, W. D. Dorland, G. W. Hammett, P. Rodrigues, and N. F. Loureiro, "Intrinsic momentum transport in up–down asymmetric tokamaks", Plasma Phys. Control. Fusion **56**, 095014 (2014).

[89] M. A. Beer, S. C. Cowley, and G. W. Hammett, "Field-aligned coordinates for nonlinear simulations of tokamak turbulence", Phys. Plasmas **2**, 2687 (1995).

[90] M. D. Kruskal and R. M. Kulsrud, "Equilibrium of a magnetically confined plasma in a toroid", Phys. Fluids **1**, 265 (1958).

[91] A. A. Schekochihin, S. C. Cowley, W. Dorland, G. W. Hammett, G. G. Howes, G. G. Plunk, E. Quataert, and T. Tatsuno, "Gyrokinetic turbulence: a nonlinear route to dissipation through phase space", Plasma Phys. Control. Fusion **50**, 124024 (2008).

[92] G. W. Hammett and W. Dorland, *Notes on collisions in GS2*, Published online, 2003.

[93] J. D. Huba, *NRL Plasma formulary* (Naval Research Laboratory, 2016).

[94] G. W. Hammett, W. Dorland, N. F. Loureiro, and T. Tatsuno, "Implementation of large scale ExB shear flow in the GS2 gyrokinetic turbulence code", APS meeting abstracts, Presented at the 48th Annual Meeting of the Division of Plasma Physics, Abstract No. VP1.00136 (2006).

[95] E. A. Belli, "Studies of numerical algorithms for gyrokinetics and the effects of shaping on plasma turbulence", PhD thesis (2006).

[96] D. J. Applegate, C. M. Roach, S. C. Cowley, W. D. Dorland, N. Joiner, R. J. Akers, N. J. Conway, A. R. Field, A. Patel, M. Valovic, et al., "Microstability in a "MAST-like" high confinement mode spherical tokamak equilibrium", Phys. Plasmas **11**, 5085 (2004).

[97] C. M. Roach, D. J. Applegate, J. W. Connor, S. C. Cowley, W. D. Dorland, R. J. Hastie, N. Joiner, S. Saarelma, A. A. Schekochihin, R. J. Akers, et al., "Microstability physics as illuminated in the spherical tokamak", Plasma Phys. Control. Fusion **47**, B323 (2005).

[98] S. A. Orszag, "Transform method for the calculation of vector-coupled sums: application to the spectral form of the vorticity equation", J. Atmos. Sci. **27**, 890 (1970).

[99] A. M. Dimits, G. Bateman, M. A. Beer, B. I. Cohen, W. D. Dorland, G. W. Hammett, C. Kim, J. E. Kinsey, M. Kotschenreuther, A. H. Kritz, et al., "Comparisons and physics basis of tokamak transport models and turbulence simulations", Phys. Plasmas **7**, 969 (2000).

[100] B. N. Rogers, W. Dorland, and M. Kotschenreuther, "Generation and stability of zonal flows in ion-temperature-gradient mode turbulence", Phys. Rev. Lett. **85**, 5336 (2000).

[101] J. Citrin, F. Jenko, P. Mantica, D. Told, C. Bourdelle, R. Dumont, J. Garcia, J. W. Haverkort, G. M. D. Hogeweij, T. Johnson, et al., "Ion temperature profile stiffness: non-linear gyrokinetic simulations and comparison with experiment", Nucl. Fusion **54**, 023008 (2014).

[102] E. G. Highcock, A. A. Schekochihin, S. C. Cowley, M. Barnes, F. I. Parra, C. M. Roach, and W. Dorland, "Zero-turbulence manifold in a toroidal plasma", Phys. Rev. Lett. **109**, 265001 (2012).

[103] H. Faisst and B. Eckhardt, "Sensitive dependence on initial conditions in transition to turbulence in pipe flow", J. Fluid Mech. **504**, 343 (2004).

[104] J. Peixinho and T. Mullin, "Decay of turbulence in pipe flow", Phys. Rev. Lett. **96**, 094501 (2006).

[105] B. Hof, J. Westerweel, T. M. Schneider, and B. Eckhardt, "Finite lifetime of turbulence in shear flows", Nature **443**, 59 (2006).

[106] M. Avila, A. P. Willis, and B. Hof, "On the transient nature of localized pipe flow turbulence", J. Fluid Mech. **646**, 127 (2010).

[107] E. L. Rempel, G. Lesur, and M. R. E. Proctor, "Supertransient magnetohydrodynamic turbulence in keplerian shear flows", Phys. Rev. Lett. **105**, 044501 (2010).

[108] F. van Wyk, E. G. Highcock, A. A. Schekochihin, C. M. Roach, A. R. Field, and W. Dorland, "Transition to subcritical turbulence in a tokamak plasma", J. Plasma Phys. **82**, 905820609 (2016).

[109] S. H. Müller, A. Fasoli, B. Labit, M. McGrath, O. Pisaturo, G. Plyushchev, M. Podestà, and F. M. Poli, "Basic turbulence studies on TORPEX and challenges in the theory-experiment comparison", Phys. Plasmas **12**, 090906 (2005).

[110] J. Cheng, J. Dong, L. Yan, K. Itoh, K. Zhao, W. Hong, Z. Huang, L. Nie, T. Lan, A. Liu, et al., "Generation of large-scale coherent structures by turbulence in the edge plasmas of the HL-2A tokamak", Nucl. Fusion **53**, 093008 (2013).

[111] N. S. Love and C. Kamath, "Image analysis for the identification of coherent structures in plasma", Proc. SPIE (2007), p. 66960D.

[112] S. van der Walt, J. L. Schönberger, J. Nunez-Iglesias, F. Boulogne, J. D. Warner, N. Yager, E. Gouillart, T. Yu, and the scikit-image contributors, "Scikit-image: image processing in Python", PeerJ **2**, e453 (2014).

[113] C. Fiorio and J. Gustedt, "Two linear time Union-Find strategies for image processing", Theor. Comput. Sci. **154**, 165 (1996).

[114] Z. Lin, T. S. Hahm, W. W. Lee, W. M. Tang, and R. B. White, "Turbulent transport reduction by zonal flows: massively parallel simulations", Science **281**, 1835 (1998).

[115] P. H. Diamond, S.-I. Itoh, K. Itoh, and T. S. Hahm, "Zonal flows in plasma—a review", Plasma Phys. Control. Fusion **47**, R35 (2005).

[116] S. Jolliet, A. Bottino, P. Angelino, R. Hatzky, T. Tran, B. Mcmillan, O. Sauter, K. Appert, Y. Idomura, and L. Villard, "A global collisionless PIC code in magnetic coordinates", Comput. Phys. Commun. **177**, 409 (2007).

[117] T. Görler, A. E. White, D. Told, F. Jenko, C. Holland, and T. L. Rhodes, "A flux-matched gyrokinetic analysis of DIII-D L-mode turbulence", Phys. Plasmas **21**, 0 (2014).

[118] M. F. J. Fox, F. van Wyk, A. R. Field, Y.-c. Ghim, F. I. Parra, and A. A. Schekochihin, "Symmetry breaking in MAST plasma turbulence due to toroidal flow shear", Plasma Phys. Control. Fusion **59**, 034002 (2017).

[119] N. T. Howard, A. E. White, M. Greenwald, C. Holland, and J. Candy, "Multi-scale gyrokinetic simulation of Alcator C-Mod tokamak discharges", Phys. Plasmas **21**, 032308 (2014).

[120] N. T. Howard, C. Holland, A. E. White, M. Greenwald, and J. Candy, "Synergistic cross-scale coupling of turbulence in a tokamak plasma", Phys. Plasmas **21**, 112510 (2014).

[121] J. E. Kinsey, R. E. Waltz, and J. Candy, "The effect of plasma shaping on turbulent transport and ExB shear quenching in nonlinear gyrokinetic simulations", Phys. Plasmas **14**, 102306 (2007).